UNIVERSITY OF CALIFORNIA
RIVERSIDE

Theory and Applications of NMR to Problems in Material Science and Analytical Chemistry

A Dissertation submitted in partial satisfaction
of the requirements for the degree of

Doctor of Philosophy

in

Chemistry

by

Arun Agarwal

August 2010

Dissertation Committee:
Dr. Leonard J. Mueller, Chairperson
Dr. Christopher J. Bardeen
Dr. Jingsong Zhang

The Dissertation of Arun Agarwal is approved:

_____

_____

_____

Committee Chairperson

University of California, Riverside

ACKNOWLEDGEMENTS

The Text of this thesis, in part or in full, is a reprint of the material as it appears in

1. *Journal of the American Chemical Society,* 2010, 132, 1500-1501

2. Langmuir, 2007, 23, 5735-5739

3. *Journal of the American Chemical Society* 2006, *128*, 15594-15595

The co-authors, Dr. L.J. Mueller, Prof. F. Zaera and Dr. P. Feng directed and supervised the research which forms the foundation for Chapter 4 of this dissertation.

The path to my Ph.D. has been long and challenging, and I have been extremely fortunate to get constant support from a lot of people. First and foremost, I would like to thank Prof. Leonard J. Muller (Len to most of us) for his valuable mentorship and constant guidance. I still remember talking to him over the phone from India, when I was trying to make a choice on graduate schools (3:00 am India time!). His genuineness was apparent even over a long distance phone call. He has been a great friend throughout my six years of graduate school, being a mentor when necessary and a loving friend at all other times. He is a very intelligent and careful scientist who has taught me the value of sincerity, honesty, critical thinking, persistence, and hard work. We have shared a lot of life experiences, lunches and coffees together, especially in the final few years of my graduate education. Wherever I go in the future, I will miss him and his warm demeanor!

I would like to thank my committee members, Prof. Christopher Bardeen and Prof. Jingsong Zhang, for their constant support during my graduate studies at UCR. They have guided me and helped me get through the program, by sharing their experiences and scientific knowledge.

I was fortunate to have shared my lab-space with a group of knowledgeable and friendly people. Over the years, Dr. Garett Leskowitz, Dr. Doug Elliot, Dr. Ryan Olson, Dr. John Mike Kaiser, Dr. Nima Ghaderi, Dr. Jinfeng Lai, Dr. Lingling Chen, Dr. Ye Tian and our new members, Y. Wang, Olivia Alley, L. Zhu and Tommy Neubauer have all been very supportive. I have learned a lot by interacting with them. Special thanks to Gary, Ryan, Doug and Mike for helping me get inducted into the lab at an early stage of my Ph.D. career.

A lot of my work as a graduate student involved collaboration with a collection of motivated and skilled scientists. I would like to thank Prof. Pingyun Feng, Prof. Christopher Bardeen, Prof. Francisco Zaera, Prof. Robert Haddon, Prof. Cynthia Larive and Prof. David Bocian and their group members for samples and/or useful discussions. Dr. Dan Borchardt has always been the go-to person in case of any NMR or EPR issues. Dr. Kurt Hermann has been outstanding as an industrial collaborator. He has helped me refine my practical skills as a scientist. Stock room personnel Prisciliano Saavedra (Pris to us) and the “handyman” Wayne have always helped me get things done faster. Dr. Kevin Simpsons has been a good friend throughout my teaching career at UCR.

Working with Teaching Assistant Development Program (TADP) at UCR earned me new friends, including Kelly, Jennifer, Megan, Crystal, Darren and Matt. There was never a dull moment in the two years of working with them.

Cricket became a big part of my life in Southern California. I was fortunate to earn a lot of friends in the process of playing cricket for Friday Knights and Regal Cricket Club. Kanwar “Sonu” Singh and Keyur Patel are dear to me. Pukar, Sandeep, Jay, Vipul bhai, Bada Faheem, Chota Faheem, Yaseer Bhai, Purvesh, Pratik, Devraj, Hemanshu, Mayur, Aftab, T’Shaka and Azam Bhai have been very understanding and supportive through this journey as well.

Arun Sharma and Vinita Sharma (Pinkiji) have been my extended family over the past three years. Sharma’s simplicity and humility has motivated me to have a positive outlook at all times. He inspires me to be a better person every day, helping me beyond limits in every aspect of my life. He is a very special friend and I would like to thank him for all his love and support over the past eight years.

Life in graduate school was rewarding because of dear friends like David Medina, Stacie, Mike, Amy, Christiana and Andrew Rice. David and Andrew have been two pillars of strength in trying times, and have helped me extensively to reach my goals. David has been a helpful friend since my first week at UCR. His presence and support has made life fun in a foreign country. Andrew has taught me many valuable things, and has dedicated a lot of him time helping me with my work. Without him, this thesis would have been a lot harder to accomplish. Kunwar Piyush has been a valuable friend over the years. Shraeddha Tiwari has been a source of strength and support, and a very dear friend

to me! Bibhuti has been a NMR colleague and a wise friend, who always guides me when I am lost. I am thankful for that. Sonali has always been the mature friend, who respected my achievements and reminded me of them whenever I was low. I cannot forget my forming years in St. Thomas and St. Xaviers, where I met a lot of my dear friends. Prof. Marzaban, Prof. Potnis, Prof. Sapna and Prof. Hoshang were always very kind during my college years. My masters education was meaningful because of Prof. Srivastava, Prof. Ajgaonkar, and Prof Garje, all from University of Mumbi. My science teacher from middle school, Prof. Uma Sinha always loved me and inspired me to love science.

Govindaji and Bobby bhai have fed me Indian meals throughout my graduate career. Stepping into one of their stores has always helped me feel closer to home and my Indian culture. Many thanks to them!

My parents, Bishwa Nath Agarwal and Lalita Agarwal have always been the source of constant inspiration and love. They are simple people who always appreciated the beauty of science and my work. I do not think I could have come this far without their love and blessings.

One can only wish for a loving family like mine. Malka di, Girdhari jijaji, Barun (Bhai to me), Anuja bhabhi, and Pallavi are the greatest family members one can wish for! My elder sister, Malka di held my hand as a child to teach me how to write. She has always been a loving sister! Girdhari jijaji has been a great friend from day one, and has never hesitated to provide me guidance and support whenever I am in need of direction. Bhai has taught me valuable lessons in life, and given me the support which only a elder brother can provide. Over time, he has become a great friend and a constant source of

inspiration. Anuja bhabhi has added value to our lives by being a part of our family. Despite limited time that we have got to share, I feel most comfortable sharing things with her. Pallavi has always been caring and loving. She has shown interest in my work throughout my higher education. Finally, Vanisha and Vedika, our two newest members have filled our lives with joy. I miss them every day.

Finally, life would have been far less meaningful without Luiza (Pinku for me), who has provided me with unconditional love, support, encouragement and strength over the past four years. Despite being far away geographically, she managed to remain close to me at all times. This journey would have been impossible to complete without her presence.

DEDICATION

To my parents for their unconditional love and support

ABSTRACT OF THE DISSERTATION

Theory and Applications of NMR to Problems in Material Science and Analytical Chemistry
by

Arun Agarwal

Doctor of Philosophy, Graduate Program in Chemistry
University of California, Riverside, August, 2010
Dr. Leonard J Mueller, Chairperson

Recent developments in NMR spectroscopy have seen an increase in its application for the study of structure and dynamics in the field of material science. NMR can be used as a complementary technique to X-ray diffraction and other structure probing techniques such as AFM and STM in the study of complex systems. Due to its non-invasive nature, measurements can be made on samples without altering their structural or functional properties.

In this thesis three different application of solid-state NMR will be highlighted. First, the butyl-substituted spiro-biphenalenyl radical will be studied. This molecule is a member of a new class of organic conductors which posses the highest conductivity of any neutral organic molecular solid via a magnetic phase transition. ^{13}C chemical shift measurements allow us to track the transition between the diamagnetic and paramagnetic states, which we find builds in as a gradual increase in the spin-density at the aromatic sites and a decrease in the electron spin-spin coupling between adjacent radicals. Our

model suggests that the electron is not delocalized over the entire molecule, but is in fast exchange between the phenalenyl rings.

Next, the photophysics of photomechanically responsive molecular crystal nanostructures based on anthracene esters is studied using solid-state NMR. A detailed study of these materials provides significant insight into the molecular-level dynamics that give rise to the micron-scale response of the nanorods. This work provides insight into how solid-state photochemistry within nanostructured molecular crystals can give rise to novel photomechanical behavior on micron lengthscales.

Finally, the last chapter discusses several examples of analytical applications of NMR. A combined approach of using solid as well as solution state NMR spectroscopy to study the stereo-chemical and functional properties of industrially useful compounds has been presented. The approach taken has the potential to be used for a wide variety of industrial applications.

Table of Contents

LIST OF FIGURES

CHAPTER I

CHAPTER II

CHAPTER III

CHAPTER IV

LIST OF TABLES

CHAPTER III

CHAPTER IV

CHAPTER I

INTRODUCTION TO NUCLEAR MAGNETIC RESONANCE SPECTROSCOPY

1.1 History and Synopsis

Nuclear Magnetic Resonance (NMR) spectroscopy has become a routine analytical tool for solving a wide variety of molecular problems in the field of chemistry, biology and physics. Since its inception, the field of NMR and its applications has led to six Nobel Prizes (Otto Stern: 1943, Isidor I. Rabi: 1944, Felix Bloch and Edward M. Purcell: 1952, Richard R. Ernst: 1991, Kurt Wüthrich: 2002, and Paul C. Lauterbur and Peter Mansfield: 2003) and thousands of publications in the past seventy years. Significant improvement in hardware and software, along with the full maturation of solution state NMR and solid-state NMR techniques, has enabled scientists to study the structure, reactivity and dynamics of molecules, in liquid as well as solid form. Superconducting magnets leading to stable high magnetic fields, fast Fourier transformation (FFT), superior electronics, robust probes, cross-polarization in solids, and multi-dimensional NMR spectroscopy has helped boost the sensitivity and resolution of NMR spectroscopy by orders of magnitude for both solid-state and solution-state NMR. Understanding the nature of a NMR spectrum, which arises from the molecular level and chemical level details around a NMR active nucleus, unravels the mysteries of chemical reactivity and the thermodynamic and kinetic aspects of chemical reaction. This

has made NMR a central technique to gain deeper understanding of atomic and molecular level interactions in zeolites, glasses, batteries, pharmaceutical compounds, catalysts, and proteins.

In 1921, Stern and Gerlach used a beam of silver atoms passing through an inhomogeneous magnetic field[1,2] to establish the existence of an intrinsic property of electrons called spin. Isidor Rabi used an extended form of Stern-Gerlach experiment in 1937 to show that radio frequency fields can be used to manipulate the quantum state of an atom[3]. Rabi was awarded the Nobel Prize in Physics for this discovery in 1944. Inspired by these developments, Edward Purcell[4] and Felix Bloch[5] demonstrated the first bulk condensed phase NMR experiments in 1946 on solid paraffin and water respectively. They were awarded the Nobel Prize in Physics in 1952 for the first NMR experiments. Although these experiments were fundamental to the development and understanding of future NMR experiments, the chemical application of NMR became an active field of research in the years to follow. Pake[6] developed the ideas of dipolar couplings (through space association of nuclear spins), and Proctor[7] introduced the idea of Chemical shift, a small frequency shift (parts-per-million or ppm) of NMR lines originating from the local electronic structure surrounding NMR active nuclei. The observation of chemical shifts revolutionized the application of NMR to structure determination in chemistry and biology. Additional fine-structure in the form of the indirect or J coupling was established by Gutowsky [8] which helped pave the way for the determination of through bond connectivity in molecules using NMR. Multidimensional NMR, introduced by Jenner and further developed by Ernst [9]into multi resonance pulsed Fourier transform NMR, has

become a routine technique for solution and solid state NMR experiments. Since then, various aspects of experimental and theoretical NMR have been developed, including new pulse sequence design, faster spinning samples, and *ab initio* calculations of NMR parameters, to solve a multitude of structural problems.

1.2 The NMR Hamiltonian

The NMR Hamiltonian can be expressed as a sum of external field and internal field interactions[10,11], as shown in equation 1.1:

$$\hat{H}_{total} = \hat{H}_{external} + \hat{H}_{internal} \quad \textbf{[1.1]}$$

where $$\hat{H}_{external} = \hat{\mathrm{H}}_{\mathrm{B}_0} + \hat{\mathrm{H}}_{\mathrm{B}_1} \quad \textbf{[1.2]}$$

and $$\hat{H}_{internal} = \hat{H}_{CS} + \hat{H}_{Q} + \hat{H}_{SR} + \hat{H}_{D} + \hat{H}_{J} \quad \textbf{[1.3]}$$

$\hat{\mathrm{H}}_{\mathrm{B}_0}$ is the coupling of nuclear spins with an external static magnetic field, $\hat{\mathrm{H}}_{\mathrm{B}_1}$ is coupling to an external radio frequency magnetic fields, $\hat{H}_{CS}$ is the induced chemical shift, $\hat{H}_{Q}$ is the coupling to the electric field gradients (quadrupolar Hamiltonian), $\hat{H}_{SR}$ is coupling to the magnetic moment due to angular momentum (spin-rotation interaction), $\hat{H}_{D}$ is to coupling of nuclear spins to each other directly through their intrinsic magnetic dipole moments, and $\hat{H}_{J}$ is the indirect coupling through the electron spins. Discussion of spin-rotation interaction and quardupolar interactions is omitted in this thesis.

1.2.1 Zeeman Hamiltonian

The external applied magnetic field (B_0) is typically chosen to lie along the z-axis and is kept constant in space. The size of this magnetic field is usually stated in terms of ^{1}H resonance frequency in NMR parlance. For example, a 9.4 Tesla magnet is called a 400 MHz (resonant frequency) magnet and a 21.1 Tesla magnet is called a 900 MHz magnet. The Hamiltonian for the chemical shift interaction is shown in equation 1.4

$$\hbar \, \widehat{H}_{B_0} = -\hbar \, B_z \sum_i \gamma_n^i \, I_z^i \qquad \textbf{[1.4]}$$

where γ_n^i, gyromagnetic ratio of the ith nucleus indicates the magnetic strength of a given nth nucleus. Larger value of γ provides higher sensitivity to the NMR spectrum.

1.2.2 Radio Frequency Hamiltonian

The radio frequency pulse (B_1) is applied perpendicular to the external static magnetic field. The amplitude and phase of these rf pulses can be modulated to perform various NMR experiments.

$$\hbar \, \widehat{H}_{B_1} = -\hbar \, B_1(t) \cos[\omega t + \varphi(t)] \sum_i \gamma_n^i \, I_x^i \qquad \textbf{[1.5]}$$

An rf pulse is simply expressed in terms of the tip angle, θ

$$\theta = \frac{360 \, \gamma \, B_1 \, t_p}{2\pi} degrees \qquad \textbf{[1.6]}$$

where t_p is the duration for which the radio frequency is applied. Equation 1.6 is extremely handy in understanding the effect of rf pulses on the magnetization vector in an external magnetic field.

1.2.3 Chemical Shift or Nuclear Magnetic Shielding Hamiltonian

Proctor first studied the influence of local electronic contributions to the exact resonance frequency of nitrogen nuclei[7] and Dickenson studied the influence of various chemical environments on the NMR line positions of Fluorine[12] to understand the effect of electronic environment of a NMR active nuclei. The chemical shift Hamiltonian can be written as

$$\hbar\,\widehat{H}_{CS} = \hbar \sum_i \gamma_n^i\, \boldsymbol{I^i} \cdot \overline{\overline{\boldsymbol{\sigma^i}}} \cdot \boldsymbol{B_0} = \sum_i \omega^i\, I_z^i \qquad \textbf{[1.7]}$$

Where, $\boldsymbol{\sigma^i}$ is a second rank tensor called the Chemical Shift Anisotropy (CSA) tensor for a given nuclei and $-\overline{\overline{\boldsymbol{\sigma^i}}} \cdot \boldsymbol{B_0}$ is the resulting magnetic field or the shielding created at the nucleus due to its electronic environment[13]. ω^i has an angular dependence as shown in equation 1.8.

$$\omega = \sigma + \delta\left\{\frac{3\cos^2\beta - 1}{2} + \frac{\eta}{2}[\cos 2\alpha \sin^2\beta]\right\} \qquad \textbf{[1.8]}$$

Since solid samples are made up of many small polycrystallites, each of which has different special orientation in a given ensemble of sample, the chemical shift not only depends on the local structure of the nucleus but on the orientation of these crystals with respect to the external magnetic field. Unlike liquids, which are in constant tumbling motion, solid samples are immobile. Hence this gives rise to broad lines NMR spectrum, otherwise averaged out due to rapid tumbling motion in solutions. This broad line is called the power pattern in NMR spectroscopy, and an example is shown in figure 1.1

along with a depiction of a solid sample showing various orientations of polycrystallites in figure 1.2.

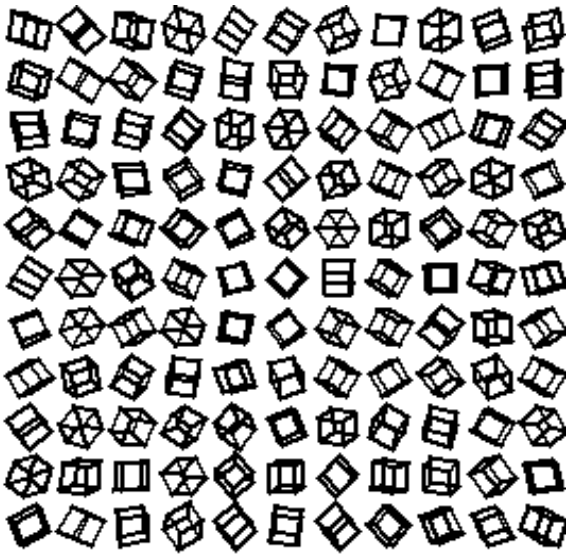

Figure 1.1 A powered solid sample composed of an ensemble of polycrystallites with various different orientations

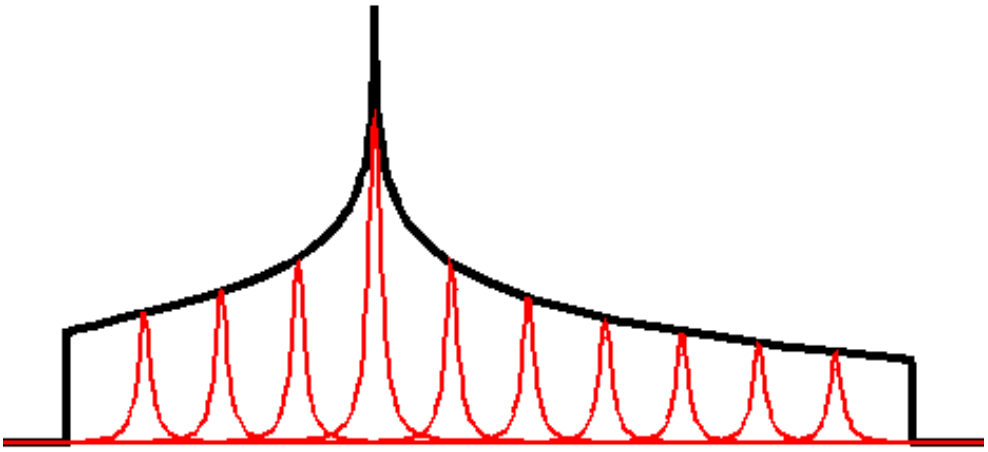

Figure 1.2 Powder pattern of a typical solid due to CSA

1.2.4 The *Dipolar Hamiltonian*

The through space or direct spin-spin interaction (D) gives rise to a significant term in the NMR Hamiltonian in solids. The dipolar tensor is traceless and axially symmetric[13] which implies that this term averages to zero in solutions, due to their rapid molecular tumbling motion. For a spin in a given orientation, there are two possible orientations of the second spin, which it is dipolarly coupled with in space, contributing to the fundamental lineshape of NMR spectrum. As shown in equation 1.9, the dipolar interaction is inversely related to the cube of the distance between the spins.

$$\hbar\,\widehat{H}_D = \sum_{i<k}\left(-\frac{\gamma_n^i\gamma_n^k\hbar^2}{r_{ik}^3}\right)\left[\frac{3(\boldsymbol{I^i}\cdot\boldsymbol{r_{ik}})(\boldsymbol{I^k}\cdot\boldsymbol{r_{ik}})}{r_{ik}^2} - \boldsymbol{I^i}\cdot\boldsymbol{I^k}\right] \qquad \textbf{[1.9]}$$

or

$$\widehat{H}_D = \sum_{\boldsymbol{i<k}} \boldsymbol{I^i}\cdot\boldsymbol{D}\cdot\boldsymbol{I^k} = \sum_{\boldsymbol{i<k}} \boldsymbol{\omega} \boldsymbol{I_z^i}\,\boldsymbol{I_z^k} \qquad \textbf{[1.10]}$$

This property makes dipolar interaction an extremely useful parameter to determine distances between spins, and thus three dimensional structures. Since the two spins that are dipolarly coupled in a given sample, $\boldsymbol{\omega}$ has an angle and distance dependence expressed in equation 1.11 below.

$$\omega = \pm\frac{\gamma_n^i\gamma_n^k\hbar}{r_{ik}^3}\left(\frac{3\cos^2\theta - 1}{2}\right) \qquad \textbf{[1.11]}$$

1.2.5 The *Scalar Coupling Hamiltonian*

The indirect spin-spin coupling also known as the Scalar (J) or through-bond coupling is much smaller in magnitude compared to direct dipolar coupling and the range of the chemical shift. This interaction exists because of the coupling of two spins that are connected with each other via a covalent bond. Since the scalar coupling interaction is weak, the effect of this coupling is small enough to only consider the isotropic part. The Hamiltonian can be written as shown in equation 1.12.

$$\hbar\hat{H}_J = \hbar \sum_{i<k} \boldsymbol{I^i} \cdot \overline{\overline{\boldsymbol{J^{ik}}}} \cdot \boldsymbol{I^k} \qquad \textbf{[1.12]}$$

Since the NMR lines are rather sharp in liquids, scalar coupling plays a significant role in solution state structure elucidation. However, the solid-state lines are broad and the magnitude of scalar couplings is usually smaller than the linewidths, making them harder to utilize for structural insights. Over the past few years, a few research groups, including our group, have established unique methodology to utilize these small range couplings to determine structure of biomolecules[14-18]. Dipolar coupling and scalar coupling are both two-spin Hamiltonians and can couple all the NMR active spins in a given sample.

1.3 Experimental Tricks

The static NMR spectrum of a solid sample is rather broad, as shown in section 1.2 (figure 1.2) of this chapter. Lines which are kHz wide, in the case of most solids, and tens of MHz broad in cases where a paramagnetic center are present, as shown in chapter 2 of this thesis, seem almost useless for detailed site-specific structural studies for

multispin systems. However these broad lines contain a wealth of information, which can be obtained by careful analysis of the data. Over the last fifty years, NMR scientists have put a lot of thought and effort into converting these featureless, non-informative spectral lines into high resolution solid state NMR signals, which have close resemblance to solution state data. There are four common, yet profound techniques, which have found a place in modern day solid state NMR experiments. They are discussed in this section.

1.3.1 Magic Angle Spinning (MAS)

The molecules in a liquid sample are in constant random tumbling motion, averaging out the anisotropy of these samples and resulting in sharp NMR lines. However, solid samples which are comprised of an ensemble of micro-crystallites can only undergo restricted molecular motion. Therefore these crystallites tend to have different spatial orientations that experience slightly different magnetic environments with respect to each other, leading to a broad NMR line. Andrew[19] and Lowe[20] introduced a method to get around the anisotropy of solid samples by spinning them mechanically about an axis tilted at an angle (the magic angle) with respect to the external magnetic field. Second rank tensors which cause anisotropy and thus broaden lines in NMR can be averaged out into sharp lines, showing only the isotropic spin interactions, just like liquids, by using this method. If the angle is carefully chosen to be $\theta_M = cos^{-1}\frac{1}{\sqrt{3}} = 54^{\circ}44'08''$, the isotropic part remains invariant under rotation, but the off axis terms experience a time average Hamiltonian that is zero, sharpening up the NMR resonances. Thus, the second rank tensors average to zero if the rotation rate (s^{-1} or Hz) is larger than or equal to the linewidth (in Hz) of the NMR spectral features. However, if the spinning

rate is slower than the linewidths, spinning sidebands are produced at multiples of the spinning frequency[21,22]. As the spinning rate is increased, these sidebands move away from the central line, and diminish in intensity as well. Thus, the choice of spinning rate is an important factor in setting up NMR experiments, since it demands caution to not have the sidebands overlap other NMR signals that may be present. Recently, ultra high spinning rates of up to 70 kHz have been achieved in solid state NMR experiments[23-25] to

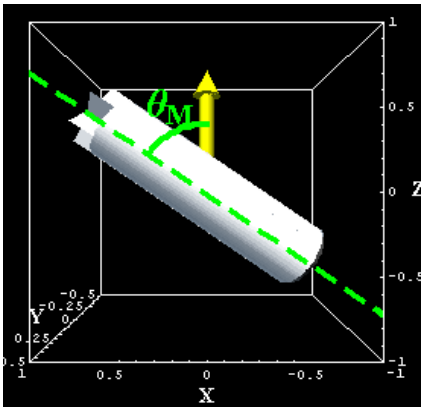

Figure 1.3 Solid State NMR sample holder (4 mm 'rotor') aligned at Magic angle of 54.74° from the external magnetic field

almost remove all dipolar couplings of protons, which have other advantages along with narrowing of NMR lines. Thus MAS enhances the resolution and sensitivity of ssNMR spectra, but leads to loss of information being generated from second rank interactions, such as dipolar couplings and spatial distribution of chemical shift tensors.

1.3.2 Cross Polarization (CP)

Magic angle spinning can make NMR lines narrow, but lesser sensitive nuclei would still have the problem of weak NMR signals and long relaxation delays for the magnetization to recover. Gibby and Pines[26,27] realized that the polarization of dilute

spins with low gyromagnetic ratio, such as ^{13}C (a common NMR nucleus in organic, biological and inorganic materials) and low natural abundance of 1.10% can be enhanced by transferring the polarization from a abundant spin, such as ^{1}H (natural abundance of 99.9%). This polarization transfer, which leads to an increase in the signal of the rare, and often more interesting spin, S, requires the latter to come into thermal contact with the abundant spin, I, by matching their Larmor frequencies as suggested by Hartmann and Hahn. This is called the Hartmann-Hahn double resonance condition, as shown in equation 1.13.

$$\boldsymbol{\gamma_I B_{1I} = \omega_I = \gamma_S B_{1S} = \omega_S} \qquad \textbf{[1.13]}$$

In this equation, γ_I and γ_S are the gyromagnetic ratios, and B_{1I} and B_{1S} are the frequency strength of abundant I and rare S spins. Thus, ω_I and ω_S are the two continuous radio frequency field at their respective resonance frequencies. When the Hartmann-Hahn condition is met, i.e. equation 1.13 holds true, the nutation frequencies of the two spins become equal in the doubly-rotating frame, creating a dipolar contact between the two spins, enabling the transfer of polarization from the 'hot' abundant spins to the 'cold' rare spin, until they reach thermal equilibrium.

Averaging out the second rank tensors to zero, by the use of magic angle spinning and using the matching conditions of cross-polarization, an enhancement by a factor of 4 can be attained in the sensitivity of rare ^{13}C spectra in a ^{1}H-^{13}C CP-MAS NMR experiment. Cross-polarization is the fundamental building block to most of the modern day ss-NMR experiments. It can also be used as a means to transfer magnetization between different nuclei in a multidimensional NMR experiment, aimed at gaining

structural and correlation information. Finally, since the intensity of enhanced signal depends on its proximity to the abundant spins, cross-polarization also provides an insight into the distances between different sites, for instance, on catalytic surfaces.

1.3.3 Decoupling

Two spins, which are close to each other in space, can communicate with each other via dipolar coupling. This can lead to broadening, and hence a loss in sensitivity and resolution of NMR lines. Since the probability of finding two rare nuclei dipolar coupled in an unlabeled sample is rather low (they have low natural abundance), homonuclear ^{13}C-^{13}C and ^{15}N-^{15}N dipolar couplings are almost absent. However, the NMR signal of the rare spin can become broad due to its coupling with highly abundant ^{1}H in the sample, called heteronuclear coupling (since it involves two different types of nuclei). The heteronuclear couplings can be removed if the time average dipolar field of protons can be made to go to zero. This can be achieved by applying continuous irradiation on the proton channel with specially designed pulse sequences (repeating units of pulses with predefined phases and tip angles). Some of these decoupling sequences are MLEV-16, WALTZ-16, TPPM[28], XiX[29] and the one which is most commonly used in this thesis is SPINAL64[30]. In order to remove heteronuclear coupling of about 20 kHz, dipolar fields of 40 kHz is typically used on the proton channel.

1.3.4 Phase Cycling

Phase cycling is used to select the coherences which one desires to have in an experiment and reject all the other ones. It can be achieved by alternating the phases of the applied NMR pulses and that of the receiver. The phase of radio frequency pulses

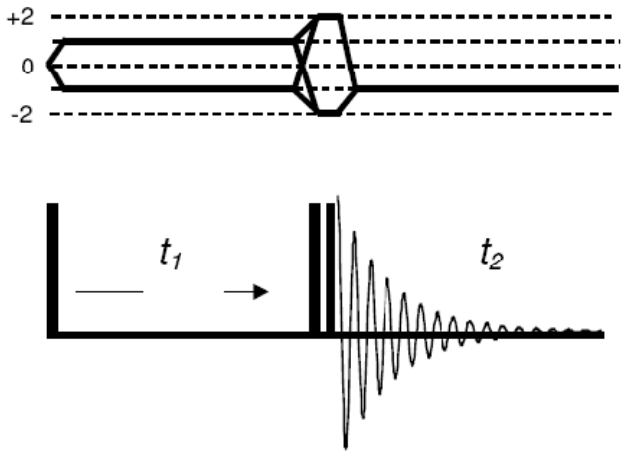

Figure 1.4 Coherence diagram and pulse sequence of 2QFCOSY

used in a particular pulse sequence is manipulated to select pathways which only allow the desired terms to pass, during the entire pulse cycle. This can not only help in removing imperfections from the pulses but also selectively detecting specific responses in multidimensional NMR experiments. As an example, pulse sequence of double quantum filtered COSY is shown in figure 1.4, along with its coherence diagram, showing the phase-cycle chosen coherence pathway.

1.4 Thesis Layout

This thesis describes the theory and application of solid-state NMR spectroscopy to problems in material science and engineering. The three following chapters truly establish the use of solid-state NMR in solving a gamut of problems, mostly in combination with some other analytical techniques. Chapter 2 uses the idea of paramagnetic NMR extensively to understand the electronic properties of a neutral organic radical conductor. A brief introduction of paramagnetic NMR, which can be

highly useful in additional areas such as the structure determination of metalloproteins and natural clay matter, is also presented at the beginning of this chapter. Chapter 3 illustrates application of solid-state NMR to the emerging and promising field of NMR crystallography, wherein a combined use of NMR and X-ray crystallography helps understand the photophysics of photomechanically responsive molecular crystal nanorods. Chapter 4, which is the final subject chapter in this thesis, encompasses some examples from both solid and solution state NMR to analyze complex mixtures to figure out the structure and reactivity of industrially relevant samples. Finally the last part of this thesis sums up all the work that has been described in this thesis, in conclusion. Throughout this thesis, ideas described in this chapter are used to improve the sensitivity and resolution of NMR lines. Figure 1.5 shows the solid-state NMR spectra of adamantane under various conditions of MAS and decoupling to illustrate the importance of these tools in proper collection and analysis of data to solve problems.

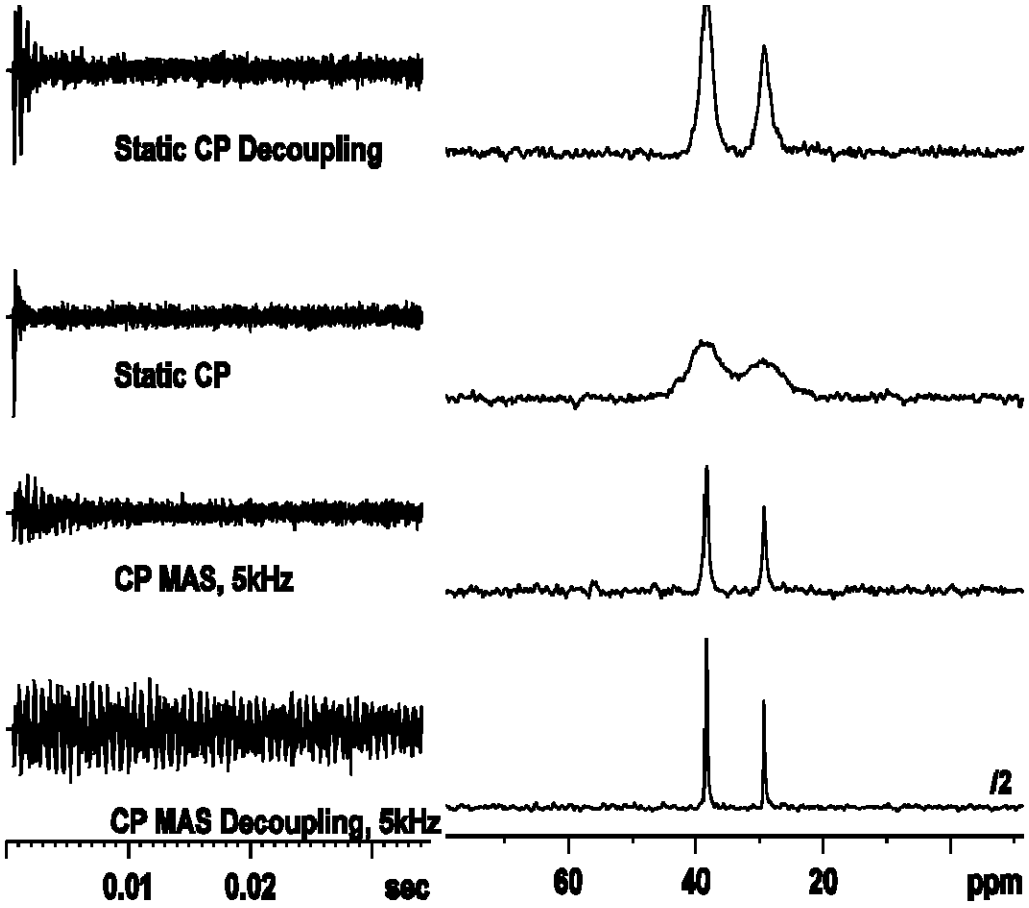

Figure 1.5 ^{13}C NMR spectra of Adamantane a) No MAS; with decoupling, b) No MAS; no decoupling, c) MAS (5kHz); no decoupling and d) MAS (5 kHz) and decoupling.

1.5 Conclusion

The field of NMR has established itself as an essential research tool of any modern day analytical laboratory. The use of spin gymnastics in designing new pulse sequences and the use of existing experiments along with MAS, cross polarization, isotope labeling, decoupling, ultra fast spinning, low temperature studies and phase cycling have made NMR a popular choice to solve problems in wide variety of disciplines. The field is growing rapidly showing its power by answering unanswered questions in multiple disciplines. Solid theoretical foundations and state of the art equipment design have made NMR both challenging and highly useful to chemists. The use of solid state NMR for molecular structure determination leads to making successful chemical models, which answers questions about chemical reactivity and dynamics.

REFERENCES

(1) Stern, O. *Zeitschrift Fur Physik* **1921**, *7*, 249-253.

(2) Gerlach, W.; Stern, O. *Zeitschrift Fur Physik* **1921**, *8*, 110-111.

(3) Rabi, I. I.; Zacharias, J. R.; Millman, S.; Kusch, P. *Physical Review* **1938**, *53*, 318-318.

(4) Purcell, E. M.; Torrey, H. C.; Pound, R. V. *Physical Review* **1946**, *69*, 37-38.

(5) Bloch, F.; Hansen, W. W.; Packard, M. *Physical Review* **1946**, *69*, 127-127.

(6) Pake, G. E. *Journal of Chemical Physics* **1948**, *16*, 327-336.

(7) Proctor, W. G.; Yu, F. C. *Physical Review* **1950**, *77*, 717-717.

(8) Gutowsky, H. S.; Mccall, D. W.; Slichter, C. P. *Physical Review* **1951**, *84*, 589-590.

(9) Ernst, R. R.; Anderson, W. A. *Review of Scientific Instruments* **1966**, *37*, 93-+.

(10) Mehring, M. *Principles of high resolution NMR in solids*; 2nd, rev. and enl. ed.; Springer-Verlag: Berlin ; New York, 1983.

(11) Haeberlen, U. *High resolution NMR in solids : selective averaging*; Academic Press: New York, 1976.

(12) Dickinson, W. C. *Physical Review* **1950**, *78*, 339-339.

(13) Abragam, A. *The principles of nuclear magnetism*; Clarendon Press: Oxford,, 1961.

(14) Tian, Y.; Chen, L. L.; Niks, D.; Kaiser, J. M.; Lai, J. F.; Rienstra, C. M.; Dunn, M. F.; Mueller, L. J. *Physical Chemistry Chemical Physics* **2009**, *11*, 7078-7086.

(15) Chen, L. L.; Kaiser, J. M.; Lai, J. F.; Polenova, T.; Yang, J.; Rienstra, C. M.; Mueller, L. J. *Magnetic Resonance in Chemistry* **2007**, *45*, S84-S92.

(16) Chen, L.; Kaiser, J. M.; Polenova, T.; Yang, J.; Rienstra, C. M.; Mueller, L. J. *Journal of the American Chemical Society* **2007**, *129*, 10650-+.

(17) Chen, L. L.; Olsen, R. A.; Elliott, D. W.; Boettcher, J. M.; Zhou, D. H. H.; Rienstra, C. M.; Mueller, L. J. *Journal of the American Chemical Society* **2006**, *128*, 9992-9993.

(18) Emsley, L.; Mueller, L. J. *Magnetic Resonance in Chemistry* **2007**, *45*, S1-S1.

(19) Andrew, E. R.; Bradbury, A.; Eades, R. G. *Nature* **1959**, *183*, 1802-1803.

(20) Lowe, I. J. *Physical Review Letters* **1959**, *2*, 285-287.

(21) Herzfeld, J.; Berger, A. E. *Journal of Chemical Physics* **1980**, *73*, 6021-6030.

(22) Maricq, M. M.; Waugh, J. S. *Journal of Chemical Physics* **1979**, *70*, 3300-3316.

(23) Bertini, I.; Emsley, L.; Lelli, M.; Luchinat, C.; Mao, J. F.; Pintacuda, G. *Journal of the American Chemical Society* **2010**, *132*, 5558-+.

(24) Laage, S.; Sachleben, J. R.; Steuernagel, S.; Pierattelli, R.; Pintacuda, G.; Emsley, L. *Journal of Magnetic Resonance* **2009**, *196*, 133-141.

(25) Salager, E.; Stein, R. S.; Steuernagel, S.; Lesage, A.; Elena, B.; Emsley, L. *Chemical Physics Letters* **2009**, *469*, 336-341.

(26) Pines, A.; Gibby, M. G.; Waugh, J. S. *Journal of Chemical Physics* **1973**, *59*, 569-590.

(27) Pines, A.; Waugh, J. S.; Gibby, M. G. *Journal of Chemical Physics* **1972**, *56*, 1776-&.

(28) Bennett, A. E.; Rienstra, C. M.; Auger, M.; Lakshmi, K. V.; Griffin, R. G. *Journal of Chemical Physics* **1995**, *103*, 6951-6958.

(29) Detken, A.; Hardy, E. H.; Ernst, M.; Meier, B. H. *Chemical Physics Letters* **2002**, *356*, 298-304.

(30) Fung, B. M.; Khitrin, A. K.; Ermolaev, K. *Journal of Magnetic Resonance* **2000**, *142*, 97-101.

CHAPTER II

CORRELATING STRUCTURAL AND ELECTRONIC CHANGES IN A PHENALENYL-BASED NEUTRAL RADICAL CONDUCTOR VIA SOLID-STATE NMR

2.1 Introduction

Organic compounds historically thought of as insulators with low conductivity, have come to the foreground of electronics research in pursuit of efficient molecular conductors over the past 50 years. Organic molecular conductors are made of a electron donor-acceptor pair to generate charge carriers in the salts[1,2]. The physical properties of materials govern their capacity for information processing. These properties are typically electrical, magnetic and/ or optical. Traditionally only one of these three channels were used, although two or more of these channels are available for information processing these days in the fields of optoelectronics, magnetooptics and spintronics[3]. Phenalenyl-based neutral radical organic conductors (PLY) have the advantage of possessing all three channels. They show two stable forms, depending on the temperature. Phenalenyl-based conductors are paramagnetic, insulating and infrared transparent at high temperatures whereas they are diamagnetic, conducting and IR opaque at low temperatures. Since they have an unpaired electron, they can be used in the construction of molecular metals and superconductors[4]. Phenalenyl possess high symmetry (D_{3h}) and high stability in

solutions[5]. The first neutral radical conductors were synthesized in 1991 using sulfur and nitrogen compounds[6-8].

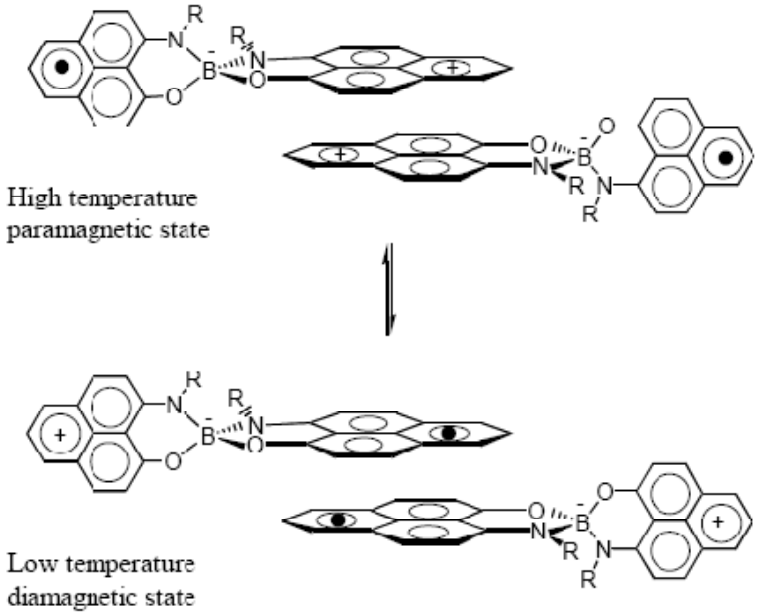

Figure 2.1 The diamagnetic and paramagnetic states of spiro-biphenalenyl radical conductors. (***Published with permission from ref 9. Copyright 2002 Science)***

The spiro-biphenalenyl radicals have two Phenalenyl rings, spiro-conjugated through a boron atom, making the two rings sterically orthogonal to each other. Since these materials are nonplanar, they cannot form one dimensional structures[9-11]. This eliminates the possibility of Peierls transition to an insulating ground state[12]. A series of functional groups can be attached to the nitrogen atoms in these radicals to alter the crystal packing and thus their properties. The first group of PLY material was formed by addition of hexyl groups [**1**] on the nitrogen atoms. Attaching hexyl groups to the nitrogen atoms made the radicals resonance-stabilized and therefore stable[13].

The alkyl group attached to nitrogen can be changed to –ethyl [**2**] or –butyl [**3**], which forces the molecules to dimerize, forming π-dimer crystals[14]. For [**3**], the interplanar distance between the π-dimer is a function of temperature. In the high temperature regime (temperature > 350 K), the interplanar distance is large (3.33 Å), which makes the pairing of electrons impossible, resulting in a paramagnetic form of the dimer. However these materials undergo a structural phase transition when temperature is lowered to below 320 K, as the interplanar distance decreases to 3.16 Å. This proximity in the Phenalenyl rings assists in the pairing of the electrons, making them diamagnetic in nature. This transition from diamagnetic form to paramagnetic form follows a completely reversible hysteresis curve. This first-order phase transition occurs with a 25-K wide hysteretic loop, between 325 K and 350 K. An increase of conductivity by two orders of magnitude is seen at the phase transition. The phase transition occurs at a temperature which is close to room temperature, thus making these materials feasible for potential applications[15] in material and semiconductor industries. These materials have the highest known conductivity amongst any organic neutral molecular conductors.

The conductivity enhancement shown by these materials does not match with their magnetic state[14]. The magnetic susceptibility (χ) for butyl substituted spiro-biphenalenyl radicals was measured with a Faraday balance in the temperature range of 10-400 K[14]. At low temperatures (T < 100 K) only paramagnetic defects in the crystal lattice makes them paramagnetic. As the temperatures is increased, they dissociate into paramagnetic π-dimers (free radicals), unpairing the coupled electrons, making the Curie spin count unity[13]. Electrical resistivity of the single crystal was measured as a function

of temperature as well[14]. A conductivity increase by two orders of magnitude is seen when the paramagnetic π-dimer transitions to the diamagnetic π-dimer as the temperature is lowered. However Peierls dimerization should lead to an insulating ground state, and not to an enhanced conductive state[1,16]. This property needs further explanation. Figure 2.2 shows the experimental observations for the magnetic susceptibility, curie spin count and conductivity all as function of temperature.

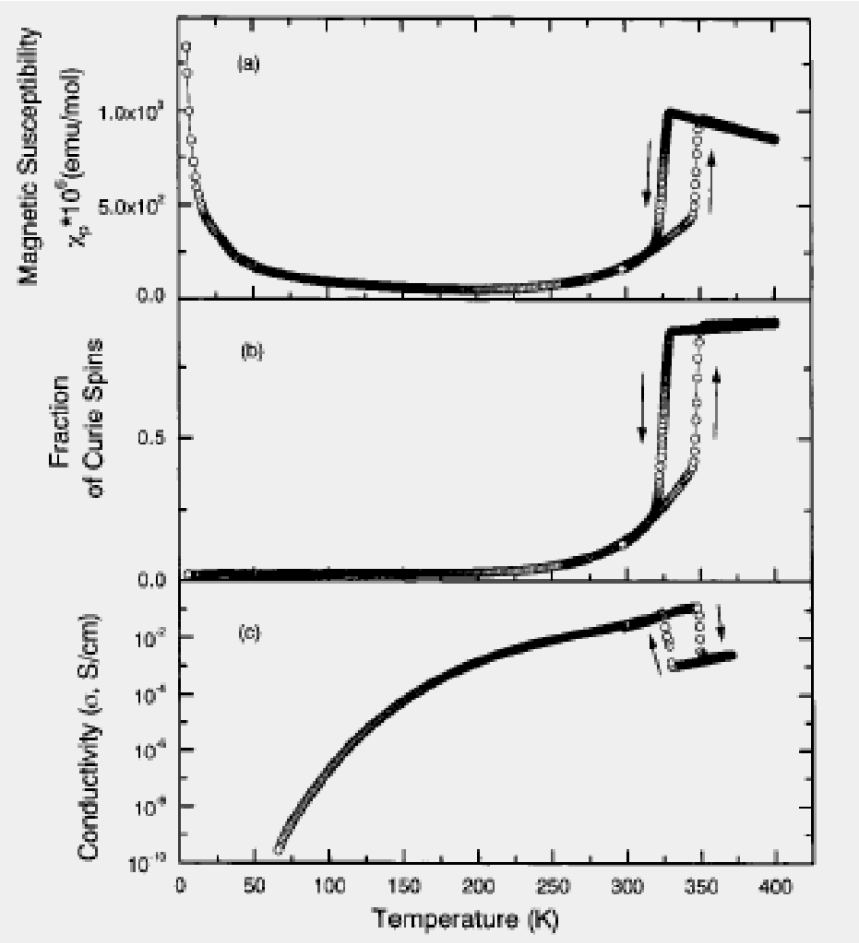

Figure 2.2 (a) magnetic Susceptibility, (b) fraction of Curie spins and (c) single- crystal conductivity of butul spiro-biphenalenyl radical conductor as a function of temperature. ***(Published with permission from ref 14. Copyright 2001 American Chemical Society)***

Over the past 30 years, NMR has been a reliable method of analysis to understand the electronic structure of these complex organic radical conductors. Yannoni et al in 1987, did a ^{13}C DNP NMR study of (Fluoranthenyl)$_2$ PF_6, a organic quasi-one-dimensional conductor[17]. A classic paper was published by Mehring and Thier in 1994 on the use of solid-state NMR for the study of metal-insulator and structural phase transition in the organic conductor (Fluoranthenyl)$_2$ PF_6. As a function of temperature[18]. Naito et al studied the electronic structure of a stable Phenalenyl radical using ^{13}C NMR at 290 K[19]. However the variable temperature studies of these molecules were not published. They did similar measurements on these molecules in liquid state to study the effect of paramagnetism on the NMR spectra of protons. ^{13}CP MAS NMR was used to obtain detailed picture of the wave function of conduction electrons by Dormann and Fischer in 1999[20]. They also reported studies on similar molecule in 2005[21]. Finally, Nakasuji et al reported variable temperature NMR studies on organic radical conductors, but they were done in solution state[22,23].

A systematic study of these butyl substituted spiro-biphenalenyl organic molecular radical conductors using variable temperature ^{13}C CP-MAS NMR has not yet been reported in literature. Such involved studies require a lot of data collection over a wide range of temperatures, following the hysteresis of the molecule several times, and complex modeling of the obtained results to understand the underlying physics of these conductors. We took up this challenge and the results of our solid state NMR study on these paramagnetic materials are presented in this chapter. Section 2.2 discusses the theory of Paramagnetic NMR in brief, and section 2.3 shows the obtained results. Section

2.4 discusses the probable model for our study to explain the mechanism of electron migration within these molecules and finally section 2.5 concludes this chapter.

2.2 Paramagnetic NMR

The presence of paramagnetic center in a molecule makes the calculation of shifts in high resolution NMR rather complex compared to diamagnetic species. In order to interpret the data and have a complete understanding of the chemical model, knowledge of ligand field theory, magnetic susceptibility, and theory of high resolution NMR is required simultaneously. Even with the inherent challenges which the presence of paramagnetic center causes, numerous structures of paramagnetic proteins have been established[24-29]. Although the presence of paramagnetism in a molecule causes the NMR lines to broaden dramatically and shift, the electron-nucleus interactions can provide knowledge about the electronic and structural arrangement of the molecule under study. Paramagnetic proteins with transition metal centers have been studied widely over the past 30 years or so using NMR spectroscopy, making use of paramagnetic shifts[30], residual dipolar couplings[31,32] and paramagnetic relaxation[33].

The net magnetization of a sample, $\vec{M}$, is given by the sum of all nuclear magnetic moment, μ_i which in turn, is proportional to the magnitude of angular momentum, where γ is the gyromagnetic ratio (equation 2.1).

$$\vec{M} = \sum_i \vec{\mu_i} = \sum_i \gamma \vec{I_i} \qquad \textbf{[2.1]}$$

The interaction of nuclear magnetic moment with an external magnetic field, B_0 is given by equation 2.2, assuming that the static magnetic field lies along the z-direction

$$\widehat{\mathcal{H}_N} = -\overrightarrow{\mu_i} . \boldsymbol{B_0} = -\hbar \boldsymbol{\gamma_N B_0 I_z} = -\boldsymbol{g_N \beta_N B_0 I_z} \qquad \textbf{[2.2]}$$

β_N is the nuclear magneton which is proportional to the ratio of charge and mass of a proton. For nuclei with half-integral spins, there can be two wave functions for the spin states, given by +½ and -½ and the solution of equation 2.2 gives the energy levels, as shown in Figure 2.3

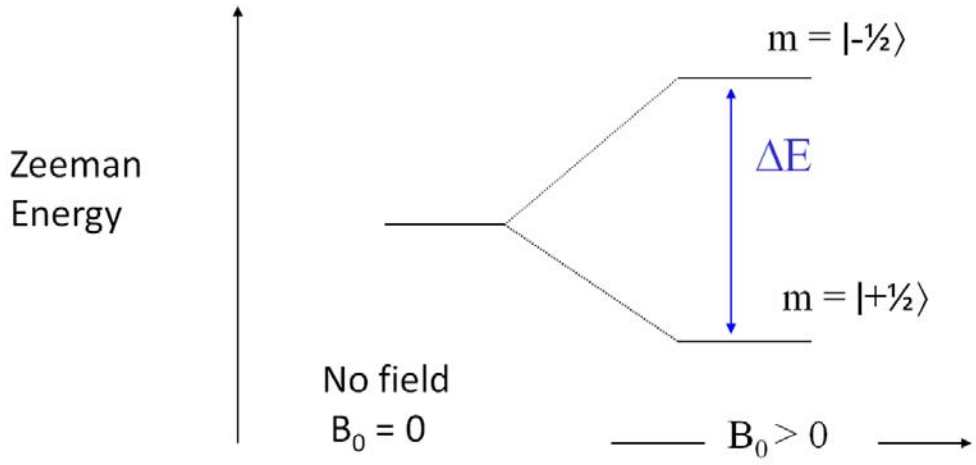

Figure 2.3 Energy levels of a nucleus with spin= ½ as a function of external field strength

The levels are degenerate in the absence of external magnetic field, B_0. According to the Boltzmann distribution, there is a slight excess of nuclei in the lower + ½ state. This equilibrium can be perturbed by application of an oscillating radio frequency,ν perpendicular to B_0, as long as the resonance condition is met.

Similar to nuclear spins, the net magnetic moment of an electron is proportional to spin angular momentum of the electron, given by equation 2.3, where g = 2.002333 for a free electron.

$$\overrightarrow{\boldsymbol{M}} = \sum_i \overrightarrow{\mu_e} = \sum_i g\,\overrightarrow{\boldsymbol{s}_i} \qquad \textbf{[2.3]}$$

The interaction of electron magnetic moment with an external magnetic field, B_0 is given by equation 2.4, assuming that the static magnetic field lies along the z-direction

$$\widehat{\mathcal{H}_e} = -\overrightarrow{\boldsymbol{\mu_e}}.\boldsymbol{B_0} = -\hbar\boldsymbol{\gamma_e}\boldsymbol{B_0}\boldsymbol{S_z} = -\boldsymbol{g_e}\boldsymbol{\beta_e}\boldsymbol{B_0}\boldsymbol{S_z} \qquad \textbf{[2.4]}$$

For a half integer electron spin, $S_z = \pm ½$, an energy level diagram similar to figure 2.3 can be made, as shown in figure 2.4, showing first the splitting in the energy levels for an electron spin and second the levels for a pair of one electron and one nuclear spin.

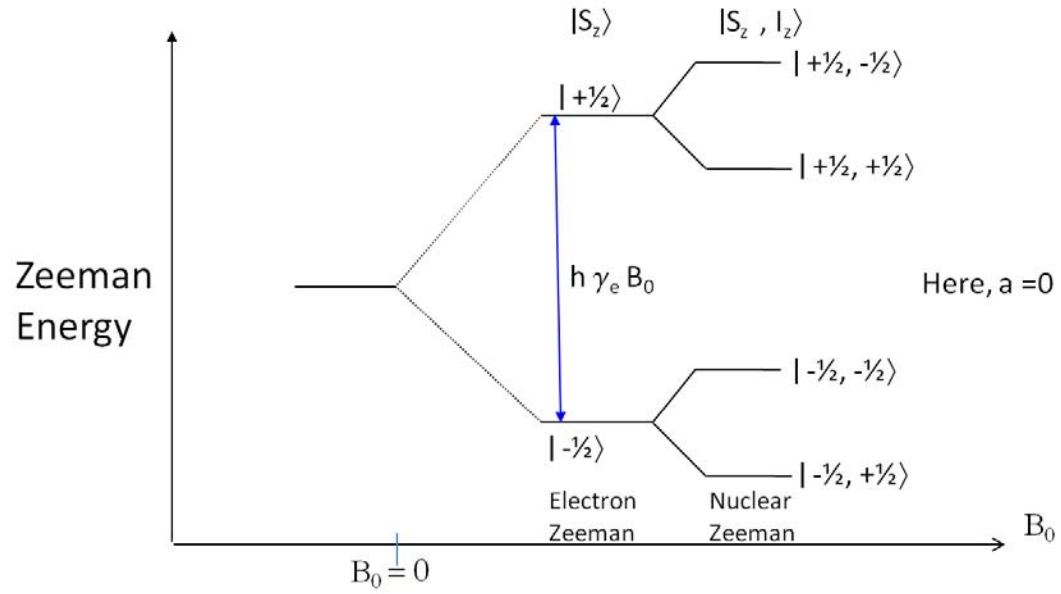

Figure 2.4 Energy levels for free electron with spin= ½ as a function of external field strength. The non-interacting protons further split the energy levels (magnified x100), as shown on the right side of the figure

It is worth mentioning that the relative energy of the splitting in figure 2.4 is 658.23 (the ratio of magnetic moments of electron to a proton). Also, the level scheme is inverted because the magnetic moment of a proton is of opposite sign as compared to an electron. Assuming no interaction between the proton and the electron (in other words, Fermi contact coupling constant, a = 0), the overall Hamiltonian can then be written as

$$\widehat{\mathcal{H}_0} = (g_e \beta_e S_z - \hbar \gamma_N I_z) B_0 \qquad \textbf{[2.5]}$$

However this is not a realistic description when the proton and the free electron are in close proximity (for example, to form hydrogen atom), giving rise to additional terms to the Hamiltonian. Their interaction provides an additional contribution to the energy, called the hyperfine shift, making NMR peaks shift (upfield as well as downfield)

compared to the pure diamagnetic shifts. Hyperfine shift is the sum of Fermi[34] (also known as Contact or Isotropic) shifts and dipolar (also known as Pseudocontact) shifts. The observed total shift is therefore a sum of hyperfine shifts (Fermi + Dipolar) and the Chemical shift,

$$\boldsymbol{\delta_{total} = \delta_{Fermi} + \delta_{Dipolar} + \delta_{Diamagnetic}} \qquad \textbf{[2.6]}$$

The delocalization of the unpaired electron spin density in a paramagnetic molecule contributes to the spin density on the nucleus, causing Fermi contact shifting of the NMR lines. Therefore, the Fermi contact shift can be given by equation 2.7, where A is isotropic hyperfine constant (Joules). The average value of $\langle S_z \rangle$ is used because electron relaxation time is much faster (by a few orders of magnitude) than the coupling frequency.

$$\boldsymbol{\delta_{Fermi} = \frac{A}{\hbar\, \gamma_N B_0} \langle S_z \rangle} \qquad \textbf{[2.7]}$$

When first order orbital angular momentum and zero field splitting are absent, the Fermi contact shift is given by equation 2.8. In this equation, g is the average molecular g-value of free electron and k_B is the Boltzmann constant.

$$\boldsymbol{\delta_{Fermi} = \left(\frac{A}{\hbar}\right) \frac{g \mu_B\, S\,(S+1)}{3\, \gamma_N k_B T}} \qquad \textbf{[2.8]}$$

The unpaired spin density in an atomic orbital fluctuates due to spin polarization of electrons in a doubly occupied molecular orbital, causing both upfield shift and

downfield shift in NMR lines. This is something which we see in our experimental data, where NMR lines shift by about 400 ppm in both directions of the diamagnetic state.

The other contribution to the frequency shift is the pseudocontact (Dipolar) shift. The dipolar term is very similar to the classical interaction between two magnetic dipoles. The Dipolar shift depends on the position of nucleus with respect to electron (r). The magnetic moment of electron, being a tensor is anisotropic, giving an average isotropic value (rather than zero) with molecular tumbling. Equation 2.9 shows the expression for calculating pseudocontact shift.

$$\boldsymbol{\delta_{Dipolar} = \frac{1}{8\pi r^3}\Big[(3\cos^2\theta - 1) \times \Big(\frac{2}{3}\,\mathrm{X}_{zz} - \frac{1}{3}\,X_{xx} - \frac{1}{3}\,X_{yy}\Big) + \sin^2\theta\ \cos 2\emptyset\big(X_{xx} - X_{yy}\big)\Big]} \qquad \textbf{[2.9]}$$

X_{xx}, X_{yy} and X_{zz} are principal component of the magnetic susceptibility tensor, and θ and ϕ are the angles between molecular axis and r. The total Hamiltonian for hydrogen like spin system can be expressed as equation 2.10[35].

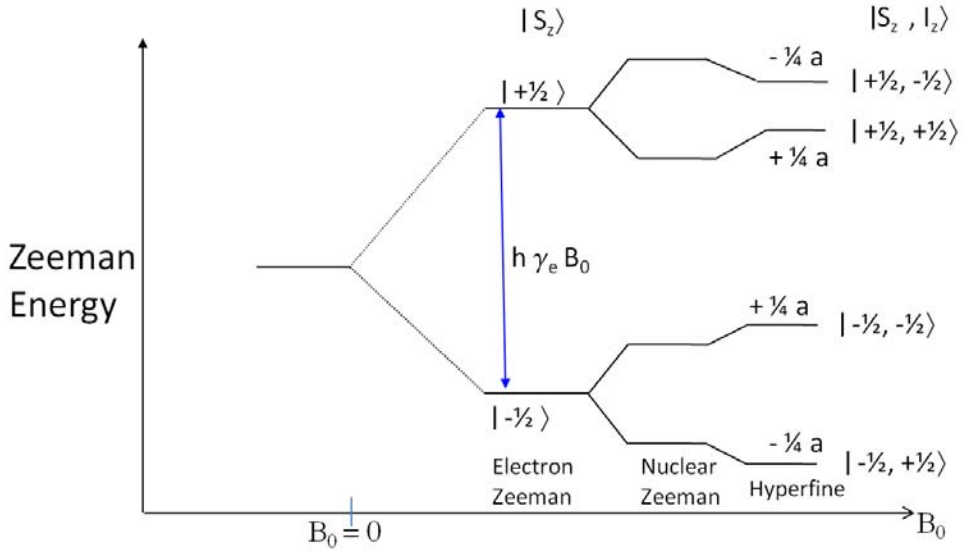

Figure 2.5 Energy levels for free electron with spin= ½ as a function of external field strength with interacting proton-electron Hamiltonian

$$\widehat{\mathcal{H}} = (g_e \beta_e S_z - \hbar \gamma_N I_z) B_0 + aS.I + \widehat{\mathcal{H}}_{Dipolar} \qquad \textbf{[2.10]}$$

Equation 2.10 can be used to draw an energy level diagram (Figure 2.5) for a free electron interacting with a proton in external magnetic field.

2.3 ^{13}C CPMAS Spectra of Butyl-substituted spiro-biphenalenyl radicals

Acquiring data on a paramagnetic solid sample can be a challenge[36,37]. The electron-nucleus coupling has three counteracting effects on the NMR parameters. The first and most prominent effect is the shifting of NMR peaks, leading to a wide range for chemical shift spread. Short excitation pulses and fast analog-to-digital converters (F-ADC) are therefore needed to collect data. The second effect of presence of paramagnetic center is shortening of T_1 relaxation time, which can actually be useful for faster data collection, increasing the signal-to-noise ratio, which is highly desired in solid-state NMR studies. However, short T_2 relaxation time gives broader NMR lines. This can lead to loss of resolution of NMR lines in these experiments. Like protons, the population of electron in a two state level system is also governed by Boltzmann distribution, which can lead to a small static magnetic moment. Curie spin relaxation (or magnetic

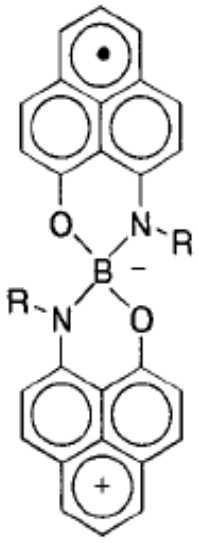

Figure 2.6 Spiro-biphenalenyl radical conductor, R = Butyl group. ***(Published with permission from ref 14. Copyright 2001 American Chemical Society)***

susceptibility relaxation), is caused by the interaction of nuclear spins with this electron static magnetic moment. Large spectral width is therefore required to make sure all the broadened and shifted NMR lines are being collected for a given paramagnetic sample. Curie spin relaxation can also contribute to line broadening. It can be reduced by running experiments at lower NMR field strengths. We chose to run our experiments on a Bruker DSX 400 spectrometer with ^{1}H resonance frequency of 400.42 MHz and ^{13}C resonance frequency of 100.70 MHz. A double resonance probe, with proton and carbon as the two channels was used to carry out cross-polarization experiments at a magic angle spinning (MAS) rate of 15 kHz. This spinning speed was carefully chosen to avoid the overlap of any spinning side bands with the acquired NMR peaks. The probe holds sample in a 2.5 mm solid zirconia rotor. 3μs ^{1}H pulse was used before Cross Polarization. During Cross Polarization (CP), the rf (radio frequency) power on ^{1}H was ramped from 75% to 100% at 83 kHz frequency maximum amplitude. Accordingly ^{13}C power was adjusted for maximum polarization transfer. 2 ms contact pulses were used on both channels during CP. A large spectral width of 100 kHz was used to acquire all the data. This ensured that all the resonances are being collected, even at higher temperatures, when the molecule becomes highly paramagnetic, shifting the lines farther away from the center. A large spectral width gave a short acquisition time of 0.020 seconds (total data points TD = 4k, Dwell time DW = 5 μs) enabling us to collect more data in a shorter period of time (NS, number of scans = 8k).

$$AQ = \frac{TD}{2 \times SW} = \frac{4096}{2 \times 10000\ Hz} = 0.020\ s$$

80 kHz nutation was used for ^{1}H decoupling (SPINAL64) while an echo pulse sequence was used on the ^{13}C channel at the same time. A one rotor-period Echo pulse sequence was required at the end of a typical cross-polarization sequence to avoid baseline distortion in these 100 kHz wide spectra. Echo pulse sequence can refocus the chemical shift evolution, heteronuclear J-couplings and magnetization vector dephased by magnetic field inhomogeneity. Since we wanted to follow the hysteresis which these spiro-biphenylenal molecules show as a function of temperature (Figure 2.2), data was acquired from -25 ˚C to +80 ˚C with five degree increments. In order to follow the hysteresis, we collected data from +80 ˚C to -25 ˚C on the way down of the hysteresis curve, cooling the sample, at every ten degree change in temperature. Longer scans were required for data collection at higher temperatures to obtain better signal-to-noise. A series of spectra which were obtained as a function of temperature are shown in Figure 2.7 below.

Figure 2.7 A series of ^{13}C CPMAS NMR spectra of Spiro-biphenalenyl radical conductor as a function of temperature is shown in the next five pages. Spectra on the left panel show the data obtained when the sample was heated up in temperature and spectra on the right hand panel show the data obtained when the sample was cooled in temperature (labeled 'cooling'). All data were acquired at a MAS rate of 15 kHz

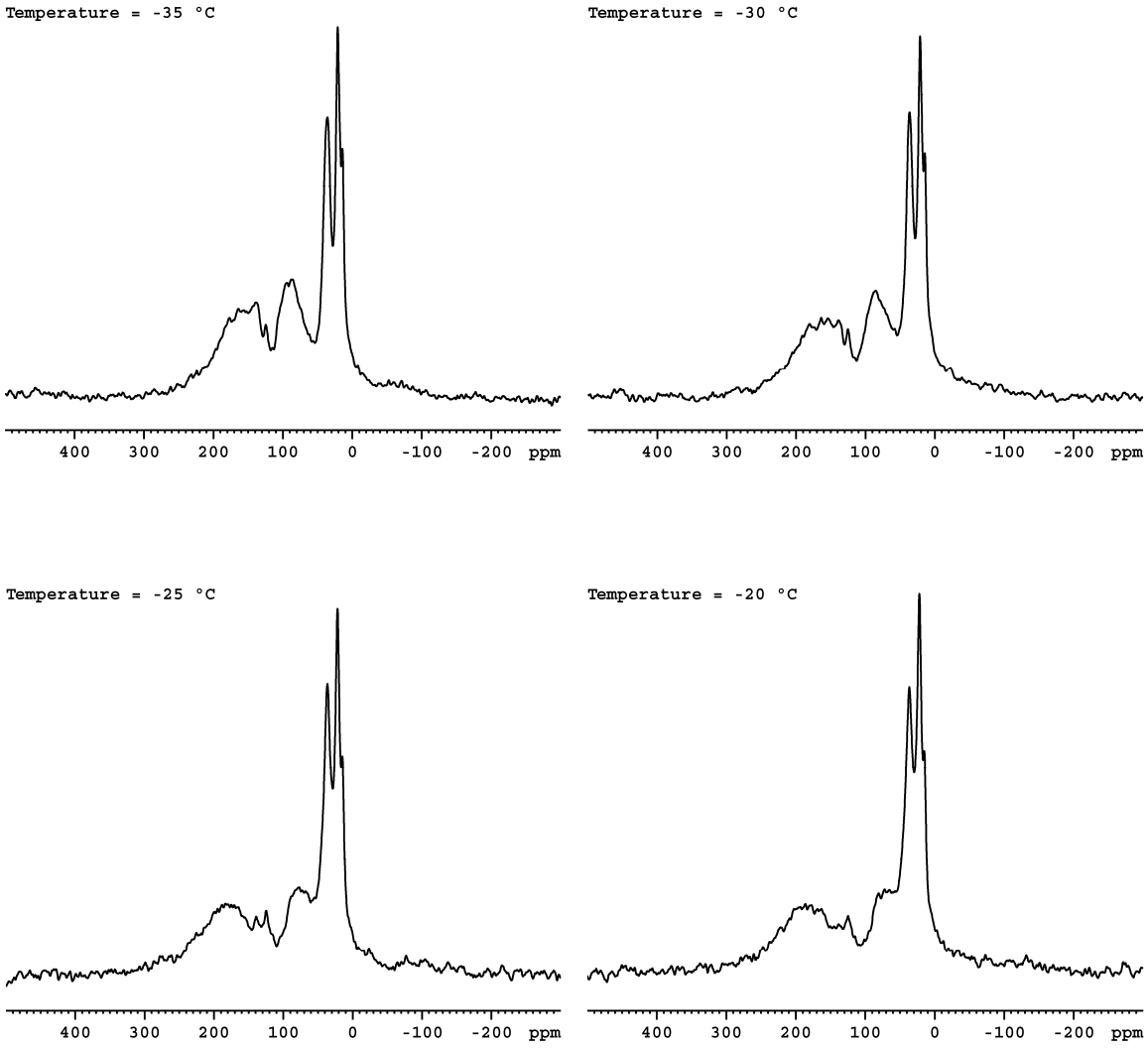

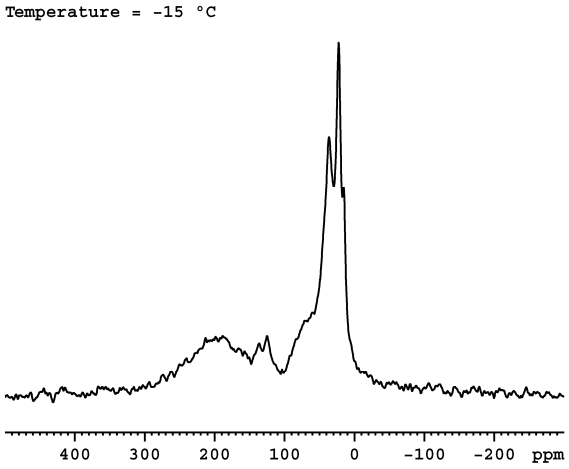
Temperature = -15 °C
400 300 200 100 0 -100 -200 ppm

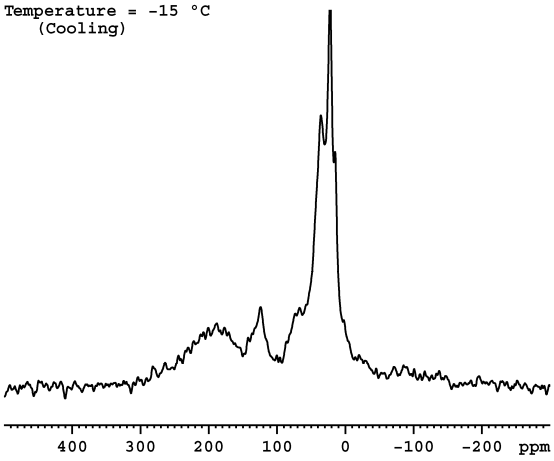
Temperature = -15 °C
(Cooling)
400 300 200 100 0 -100 -200 ppm

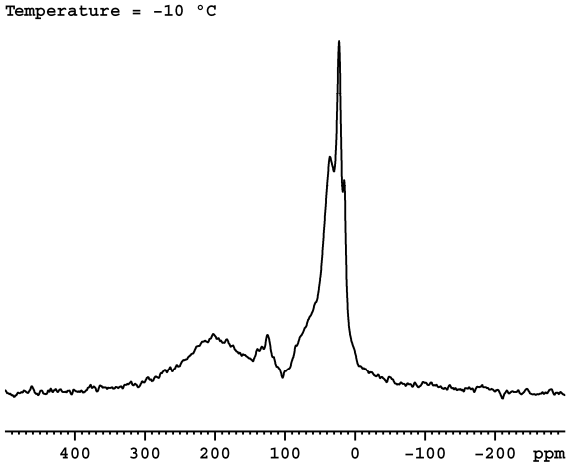
Temperature = -10 °C
400 300 200 100 0 -100 -200 ppm

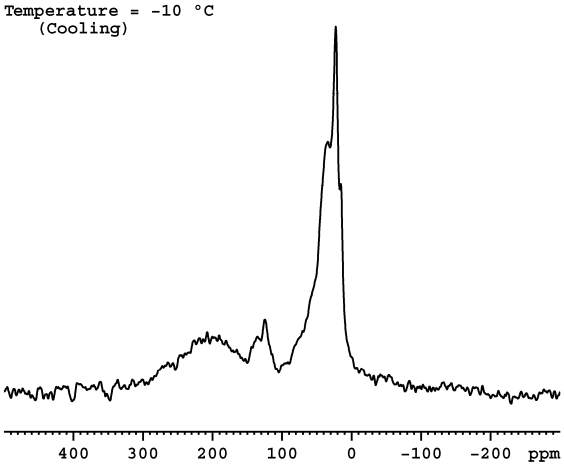
Temperature = -10 °C
(Cooling)
400 300 200 100 0 -100 -200 ppm

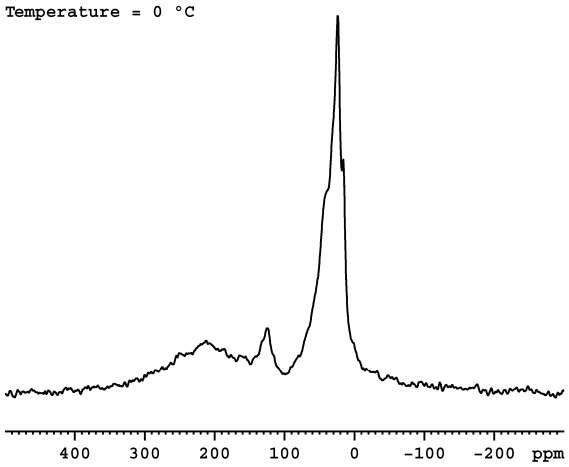
Temperature = 0 °C
400 300 200 100 0 -100 -200 ppm

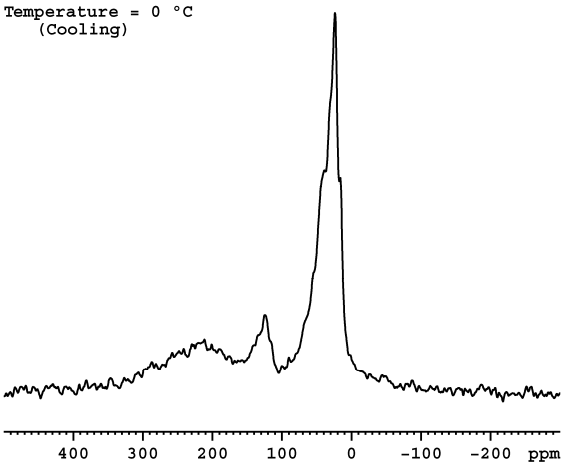
Temperature = 0 °C
(Cooling)
400 300 200 100 0 -100 -200 ppm

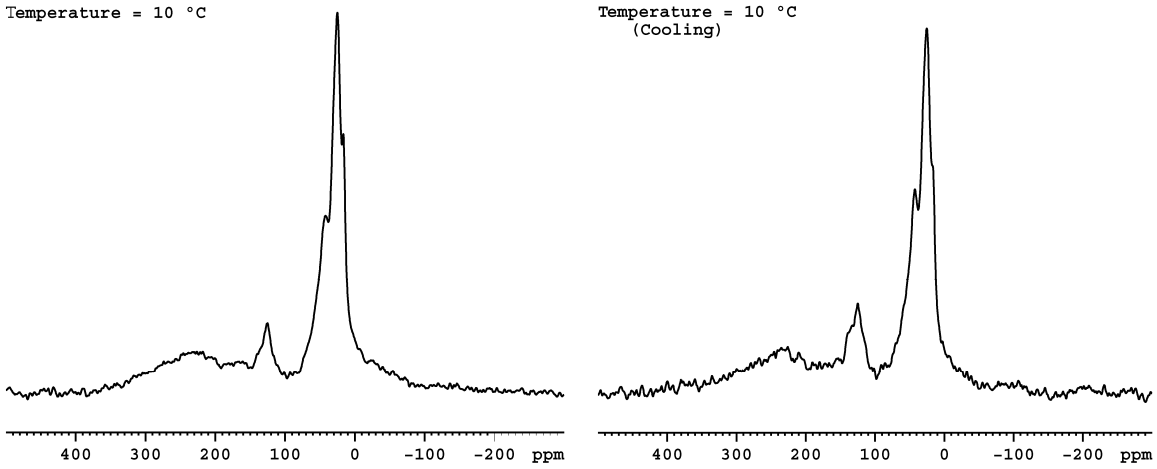
Temperature = 10 °C
400 300 200 100 0 -100 -200 ppm

Temperature = 10 °C
(Cooling)
400 300 200 100 0 -100 -200 ppm

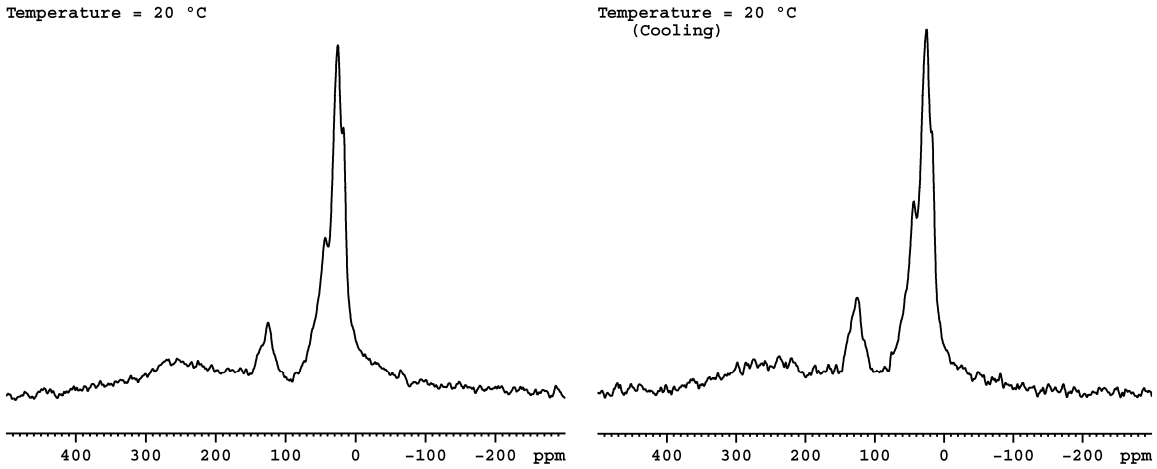
Temperature = 20 °C
400 300 200 100 0 -100 -200 ppm

Temperature = 20 °C
(Cooling)
400 300 200 100 0 -100 -200 ppm

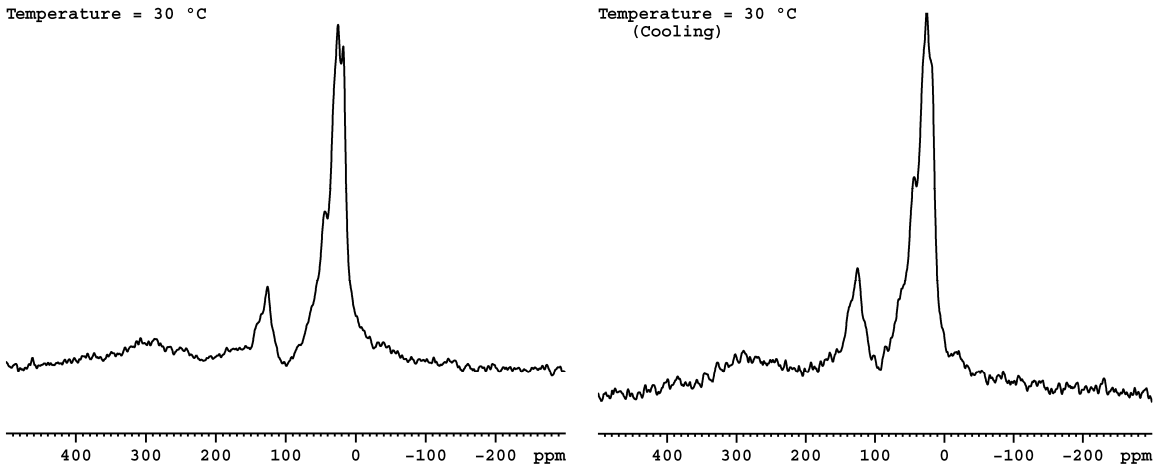
Temperature = 30 °C
400 300 200 100 0 -100 -200 ppm

Temperature = 30 °C
(Cooling)
400 300 200 100 0 -100 -200 ppm

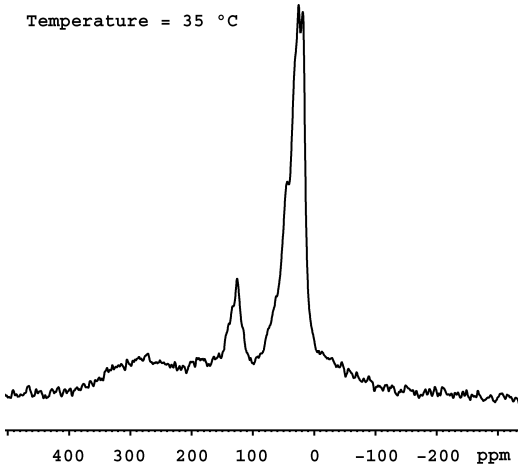
Temperature = 35 °C
400 300 200 100 0 -100 -200 ppm

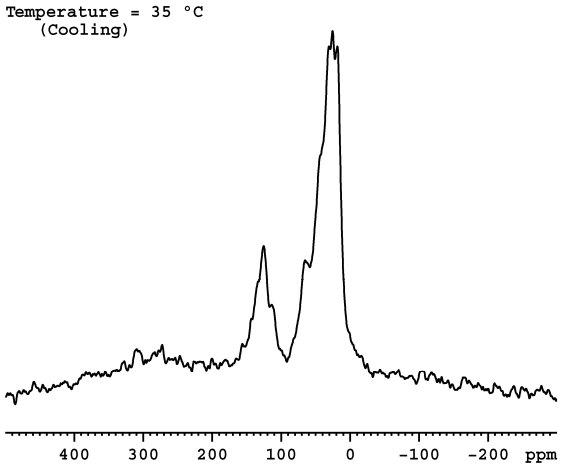
Temperature = 35 °C
(Cooling)
400 300 200 100 0 -100 -200 ppm

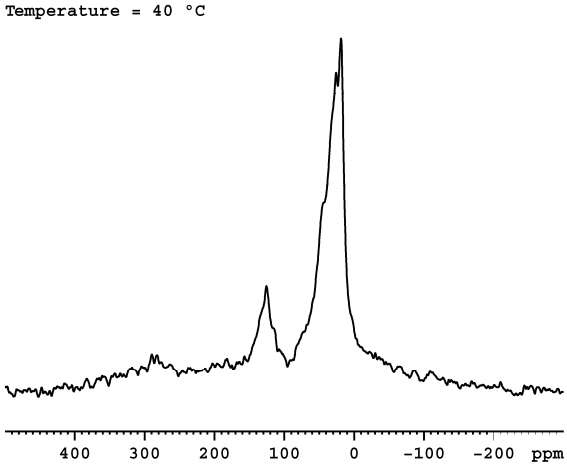
Temperature = 40 °C
400 300 200 100 0 -100 -200 ppm

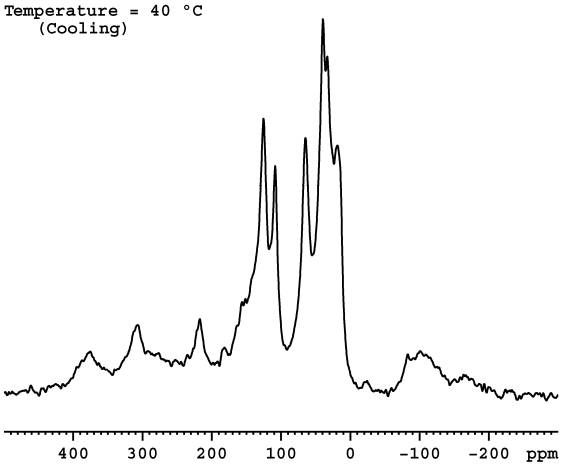
Temperature = 40 °C
(Cooling)
400 300 200 100 0 -100 -200 ppm

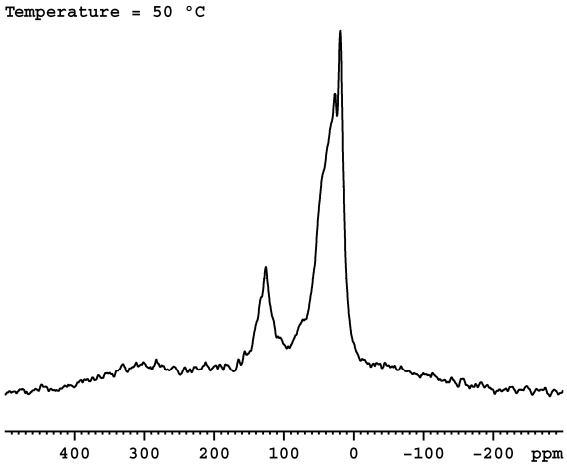
Temperature = 50 °C
400 300 200 100 0 -100 -200 ppm

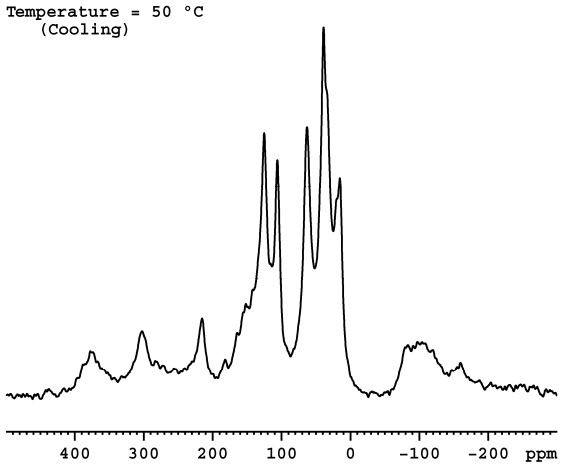
Temperature = 50 °C
(Cooling)
400 300 200 100 0 -100 -200 ppm

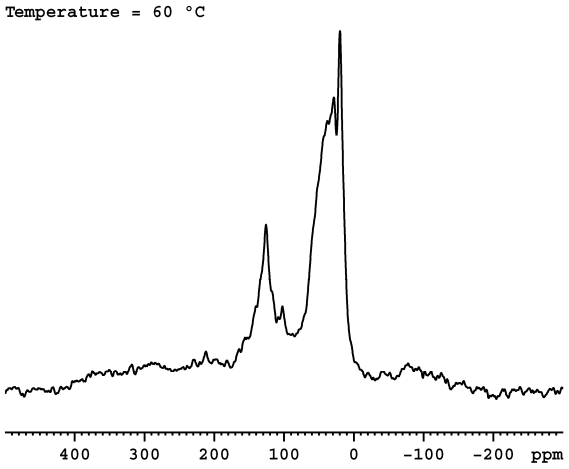
Temperature = 60 °C
400 300 200 100 0 -100 -200 ppm

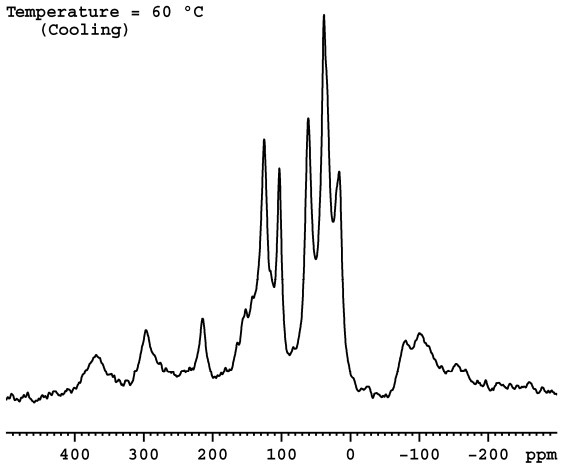
Temperature = 60 °C
(Cooling)
400 300 200 100 0 -100 -200 ppm

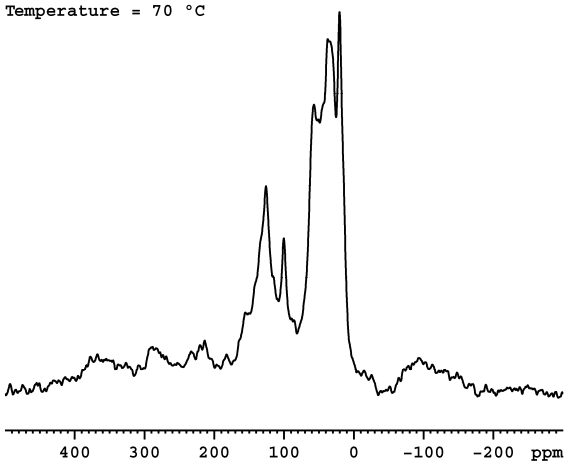
Temperature = 70 °C
400 300 200 100 0 -100 -200 ppm

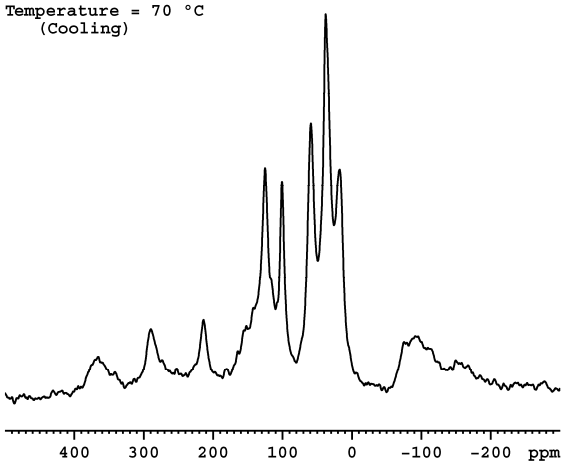
Temperature = 70 °C
(Cooling)
400 300 200 100 0 -100 -200 ppm

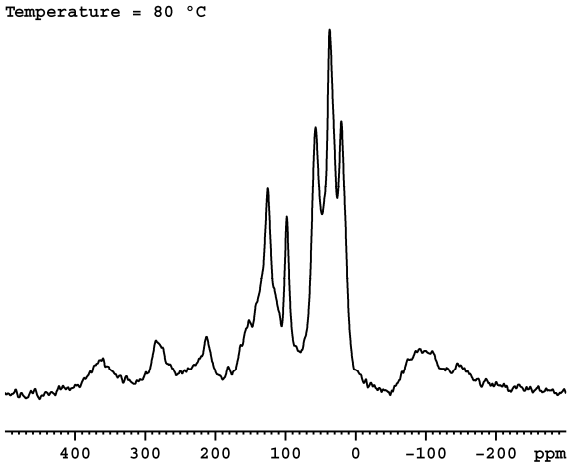
Temperature = 80 °C
400 300 200 100 0 -100 -200 ppm

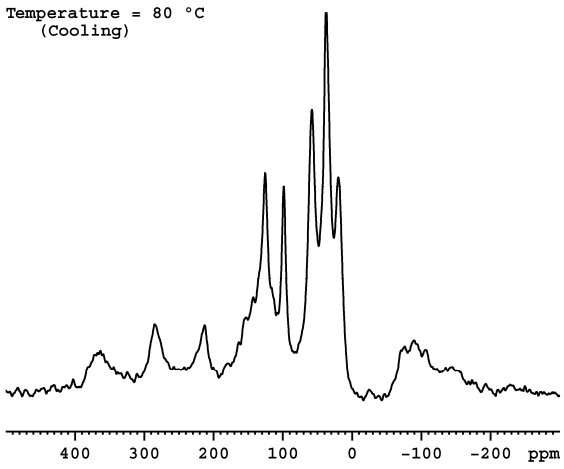
Temperature = 80 °C
(Cooling)
400 300 200 100 0 -100 -200 ppm

At the lowest temperature (-35 ˚C), the ^{13}C CPMAS spectrum has two prominent features. The aliphatic (Butyl) functional group is seen between 0-50 ppm where as the aromatic part shows up between 50-200 ppm. There are two peaks in the aromatic region, one between 60-105 ppm and the other, downfield between 130-230 ppm. This is rather unique for aromatic carbons, since they are typically present between 120-160 ppm[38,39]. This shift and broadening effect can be attributed to the paramagnetic behavior of the sample. As seen in Figure 2.2 (b), from the Curie spin measurement, the number of unpaired electrons is greater than zero at temperatures about --73 ˚C. Thus the molecule starts to show paramagnetic behavior over and above -73 ˚C. This implies that the sample is partially paramagnetic at -35 ˚C, when the first set of NMR data was collected, making the lines broaden and shift in either directions, a feature commonly seen in the NMR of paramagnetic molecules[29,40,41]. This phenomenon of line broadening and shifting from its original position follows the explanation in section 2.2 of this chapter. As the temperature is raised, the aliphatic peaks remain at the same position, between 0-50 ppm. However the two aromatic peaks, which arise from the two Phenalenyl rings in the molecule, start to shift in opposite directions, paramagnetically, and also broaden at the same time. At about 0 ˚C, the upfield aromatic peak shifts underneath the aliphatic peaks, and therefore cannot be seen. At this temperature, the other set of aromatic peaks shift between 160-300 ppm. Another noteworthy observation is that there is a sharp rise of a peak at about 125 ppm throughout the temperature range. When the temperature is increased to 35 ˚C the downfield aromatic peak shifts between 180-400 ppm, centered at 280 ppm. At the same time, the other aromatic peak finally starts to become visible, shifting between 0 ppm and

-80 ppm. A shift in these aromatic peaks indicates that the molecule has become more paramagnetic at this temperature. The aromatic peaks continue to shift and broaden, until the temperature reaches 60 ˚C, when a few changes can be seen in the NMR spectrum. The downfield peak can be seen between 180-430 ppm, over 250 ppm wide (100 kHz on a ^{1}H 400 MHz magnet). The upfield shifted aromatic peak can now be seen between -50ppm and -150 ppm. Another non-paramagnetically shifted aromatic peak can be seen at 100 ppm, along with the 125 ppm peak. All of the above mentioned observations indicate the transition of these neutral organic molecular conductors from a diamagnetic phase to a paramagnetic phase, as a function of temperature. However, interesting changes in the spectrum can be seen at 70 ˚C. The broad downfield shifted peak between 180-430 ppm resolves into three separate peaks, ranging from 320-430 ppm, 250-320 ppm and 195-250ppm. The upfield shifted aromatic peaks stay between -50ppm and -180 ppm, broadening a little, indicating the increase in the paramagnetic strength of the molecules. The aliphatic peaks stay unmoved at 100 ppm and 125 ppm respectively. This behavior persists until 85 ˚C, which is the highest temperature we collected NMR data at.

In order to follow the hysteresis which spiro-biphenalenyl molecules show, data was collected by cooling the sample from 85 ˚C, every ten degree change in temperature. The electrons were completely unpaired by raising the sample temperature to 90 ˚C for a few minutes and then the sample was cooled back down to collect data at 80 ˚C. As expected, the nature of NMR spectrum remains completely identical to the higher temperature paramagnetic state, which indicates that cooling the sample does not change the electron spin distribution between the two Phenalenyl rings of the molecule. As a

matter of fact, the NMR spectra show the exact same features all the way down to 40 ˚C, upon cooling, where the three well resolved downfield shifted peaks, the upfield shifted shoulder and two sharp non-paramagnetically shifted peaks are all present. This observation establishes that these molecular conductors hold their paramagnetic nature between 90 ˚C and 40 ˚C, without any change, as seen by Haddon et al[14], and as shown in the plateau region of the plot of fraction of Curie spin vs. temperature in Figure 2.2. The sharp resolved peaks in the NMR spectrum are lost when the sample is cooled to 35 ˚C. The 35 ˚C spectrum has the same features as the 50 ˚C spectrum which was obtained on the heating cycle, namely a broad downfield shifted line between 220-430 ppm, centered at 280 ppm, the aliphatic chain signal between 0-50 ppm, and the non-paramagnetically shifted aromatic peak at 125 ppm. Further cooling of the sample does not alter the NMR spectra, compared with the heating cycle. This suggests that the molecule goes into the same electronic state with respect to the previously discussed heating cycle as the temperature is dropped. There is no significant difference in the NMR spectra of corresponding temperatures between -35 ˚C and 35 ˚C, regardless of the sample being heated or cooled.

However, our temperature calibration seems to be slightly offset compared with the work done by Haddon et al[14], since according to our NMR data, the hysteresis persists until the sample is cooled down to 35 ˚C, unlike their data, which shows severe loss of conductivity below 47 ˚C. In order to calibrate the temperature scale that was used in our experiments, low temperature methanol NMR chemical shifts and high temperature ethylene glycol chemical shifts were obtained, and a calibration curve plotted for the

correct temperatures[42-44]. This allows us to get a much precise temperature reading for the variable temperature experiments.

2.4 Electron Paramagnetic Resonance

Electron Paramagnetic Resonance (EPR/ Electron Spin Resonance, ESR) detects the presence of unpaired electron in a molecule by measuring the amount of microwave radiation that can be absorbed by the sample placed in a magnetic field. The amount of energy absorbed typically depends on the magnitude of energy splitting of the unpaired electron according to the Boltzmann equation. In this case, however, the primary change in the number of unpaired electrons is not the temperature, but the structural changes in the crystal that lead to a larger spacing between π-dimmers and the formation of the paramagnetic states. EPR can give useful information about the structure and dynamics of an EPR active species[45-47]. Variable temperature EPR was carried out from 100 K to 360 K back to 100 K in order to see the effect of temperature on the number of unpaired electron of the spiro-biphenalenyl radical conductor. Since the protons are orthogonal to the carbons in the aromatic rings of the Phenalenyl system, the EPR signal has just one line, without any presence of hyperfine coupling (Figure 2.8).

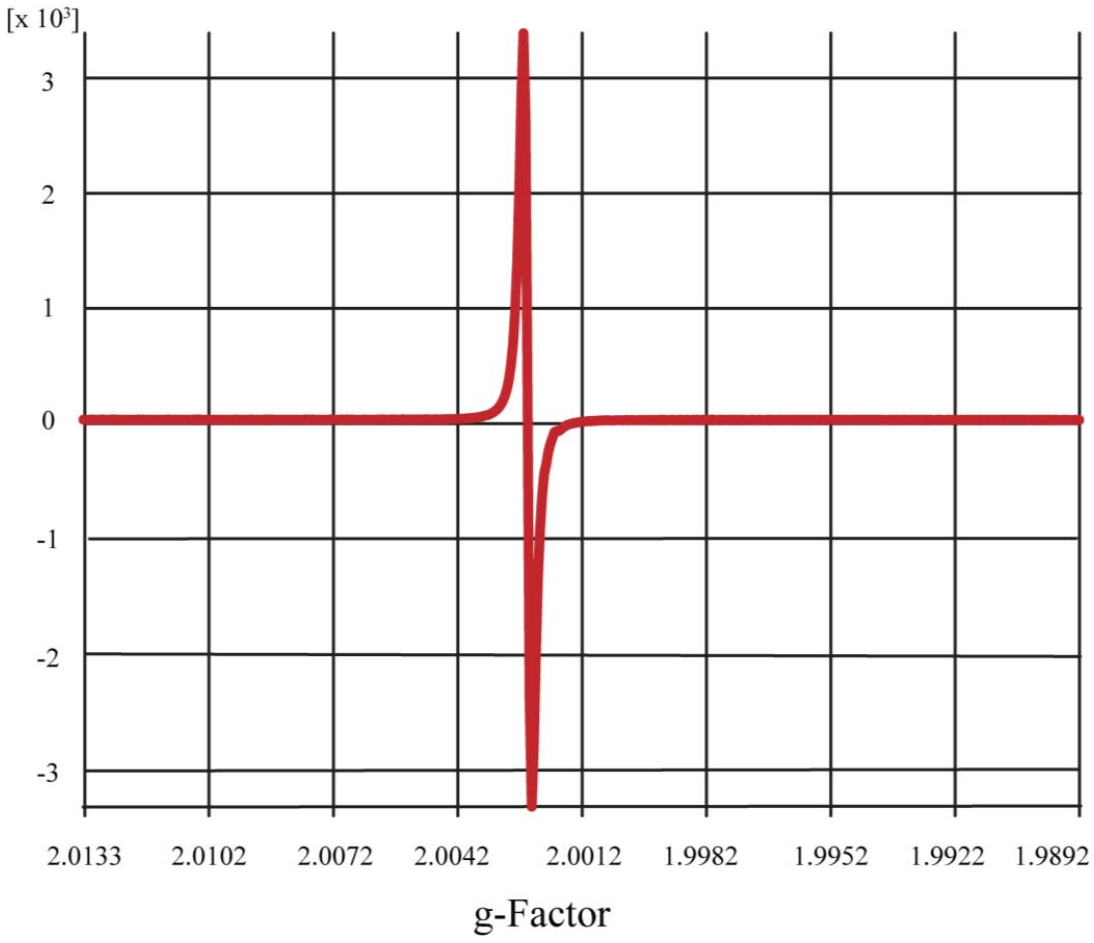

Figure 2.8 EPR spectrum of butyl-substituted spiro-biphenalenyl radical at 310 K

Thus, electron paramagnetic resonance is merely another measure of the amount of unpaired spins in spiro-biphenalenyl radical conductor. Integrated area under the curve of the EPR signal was plotted as a function of temperature (Figure 2.9), and the result matches the Curie spin measurement data shown in Figure 2.2. The hysteresis can be seen between 325 K and 350 K. Although EPR data does not shed any additional insight into the electronic structure of these molecules, it shows a reliable affirmation of magnetic phase change in these interesting molecular systems.

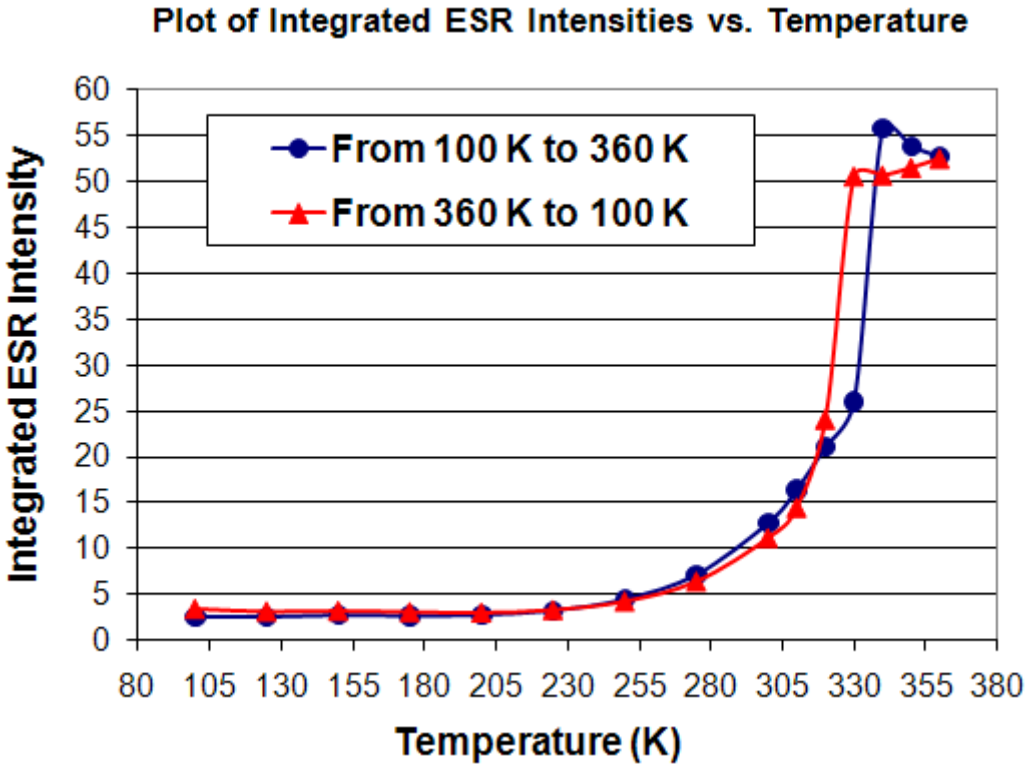

Figure 2.9 Plot of integrated EPR intensity (non-normalized) vs. temperature (K) for butyl-substituted spiro-biphenalenyl radical. Blue line represents heating curve, and red line represents cooling curve

2.5 An Electron Chemical-Exchange Model of the NMR Spectra

The low temperature NMR data could be explained using the concepts of paramagnetic NMR in section 2.3 of this chapter. However, sharpening of NMR peaks at higher temperature in the range of 200-430 ppm cannot be justified using such ideas as there is no mechanism to yield the sharpening of spectra in the high temperature experiments. This behavior is reminiscent of chemical exchange in NMR and we propose an equilibrium model shown in Figure 2.10, which we use to model the spectra below.

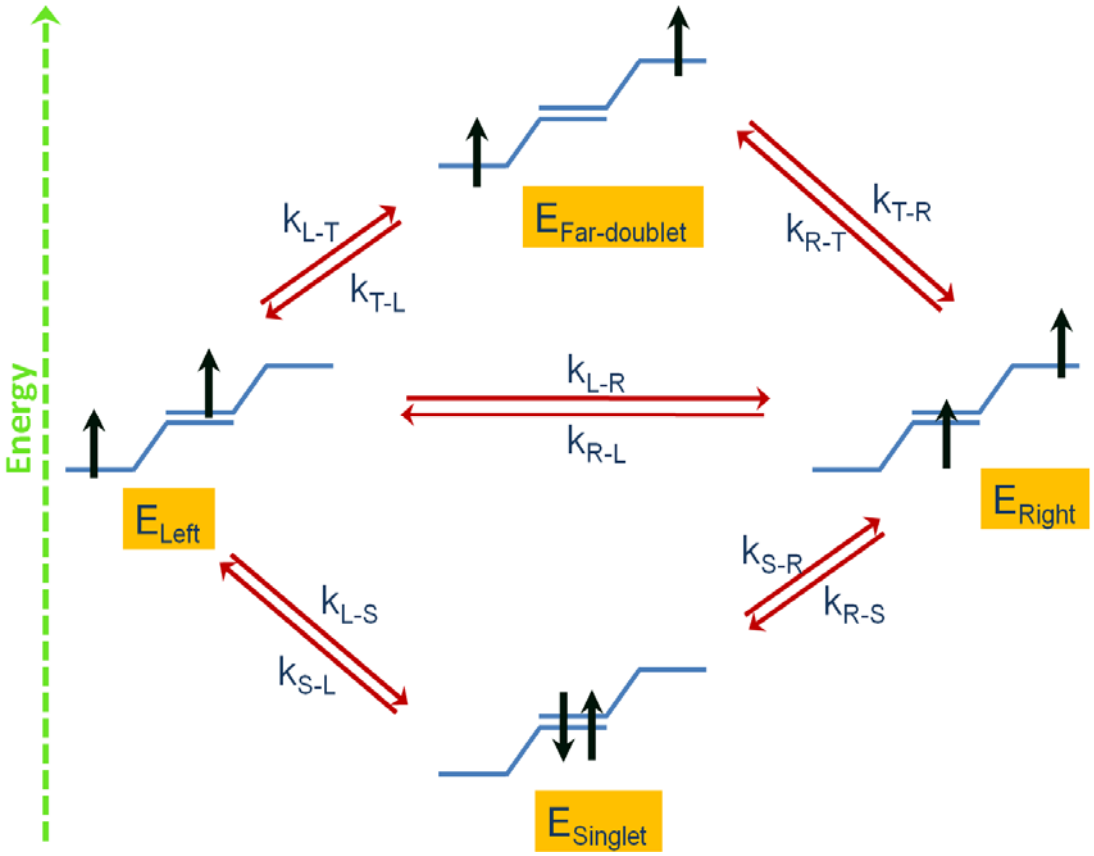

Figure 2.10 Chemical equilibrium cartoon model for butyl-substituted spiro-biphenalenyl radical showing the position of unpaired electrons on the two Phenalenyl rings in a dimer crystal packing

The chemical exchange model assumes the free electron to be in a fast exchange between the two Phenalenyl rings, rather than it being completely or fully delocalized over both. The exchange rate depends on the temperature of the system. There are four possible arrangements for the electron in the π-stacked dimer pair of molecules, giving four energy levels. When both of the free electrons reside on the inner Phenalenyl rings, they are assumed to pair up, giving rise to a singlet (non-paramagnetic) state. However, with a rise in temperature, the free electrons can unpair and move away from each other, since the inter-planar distance between the dimer molecules increase from 3.1 Å to 3.33 Å. This can lead into three different energy states, two of which are degenerate. One of the inner electrons can move to the outer ring, leaving the other electron on the inner ring in the dimer. There are two such (degenerate) possibilities, called E_{Left} and E_{Right} in Figure 2.10. Finally the two electrons can be on the outer ring of the respective dimer molecule, giving the highest energy (as shown) for the far-doublet state. The rate constants and the equilibrium constants can then be manipulated to generate fits for the observed NMR data and for equilibrium constants lower than 1, the energy diagram actually inverts. Figure 2.11 through figure 2.13 shows the experimental data (blue) and simulated plot (red) for three different temperatures. The three plots were chosen to represent a low temperature (-25 $^{\circ}$C), a mid-range temperature (25 $^{\circ}$C) and a high temperature (80 $^{\circ}$C) sample. While this fitting is admittedly preliminary, we note that we can qualitatively reproduce the observed of shifts, broadening, and coalescence in this series of spectra. More quantitative modeling is underway.

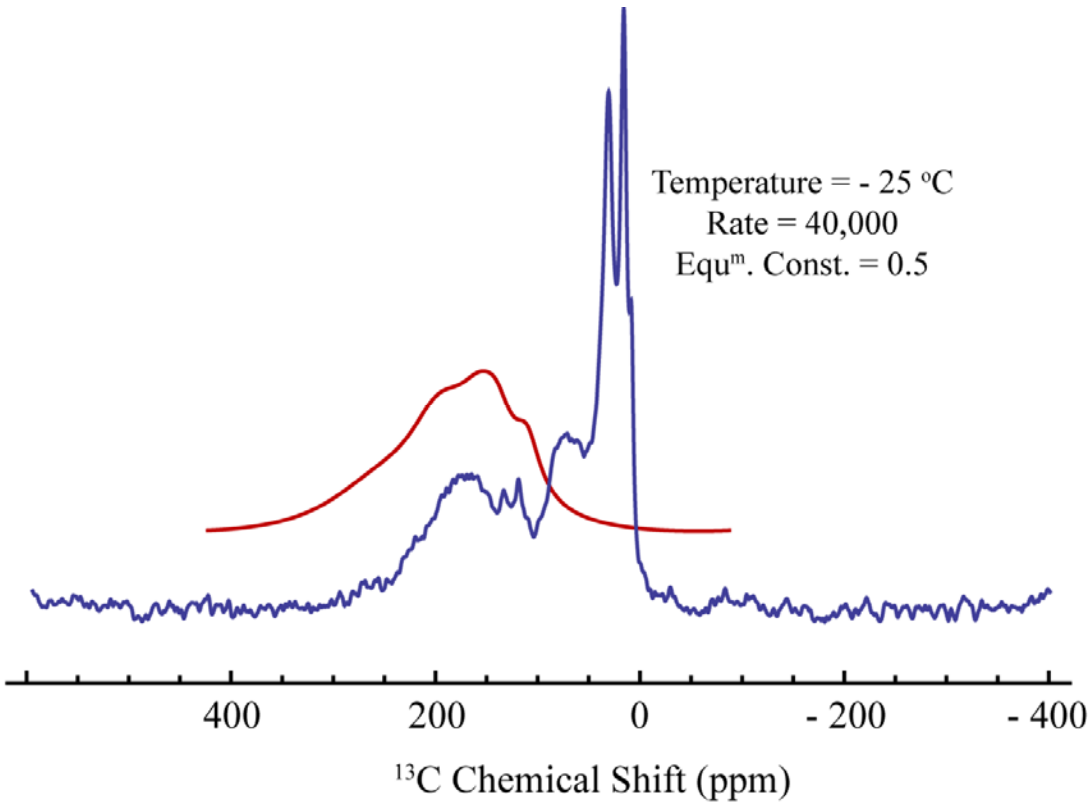

Figure 2.11 Experimental data (in blue) and simulated spectrum (in red) at -25 ˚C. the rate constant is keep fixed at 40000, and the equilibrium constant is 0.5

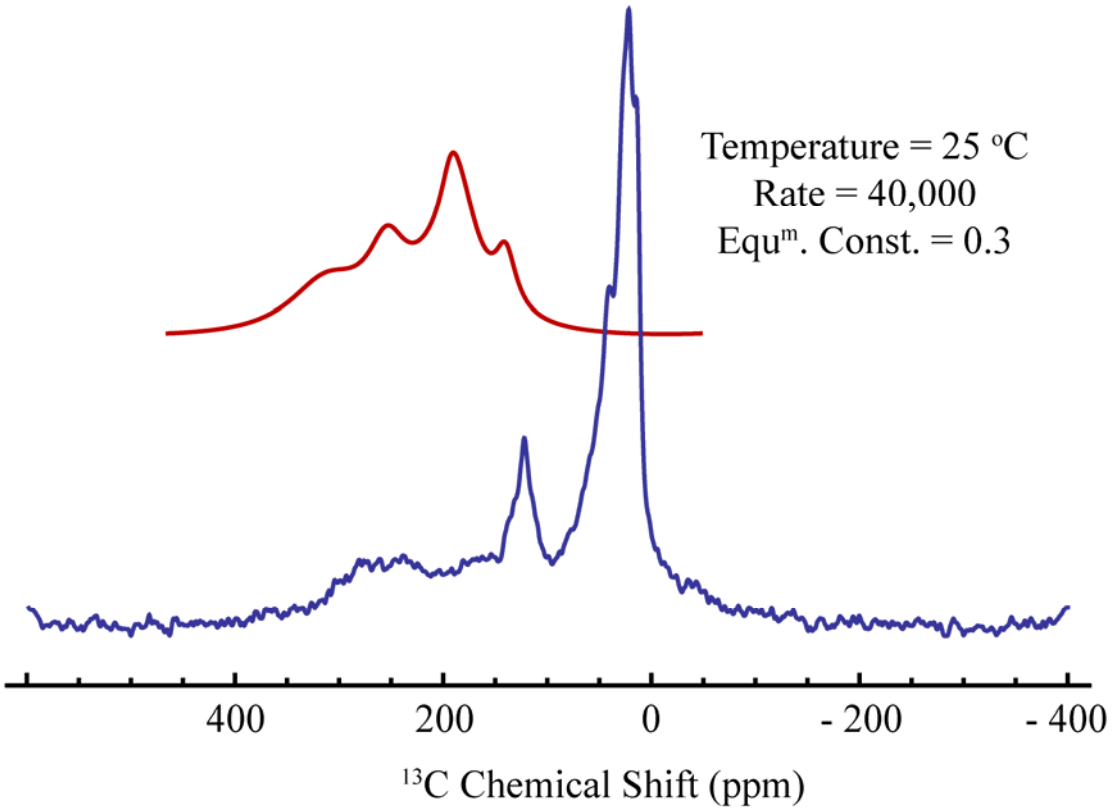

Figure 2.12 Experimental data (in blue) and simulated spectrum (in red) at 25 ˚C. the rate constant is keep fixed at 40000, and the equilibrium constant is 0.3

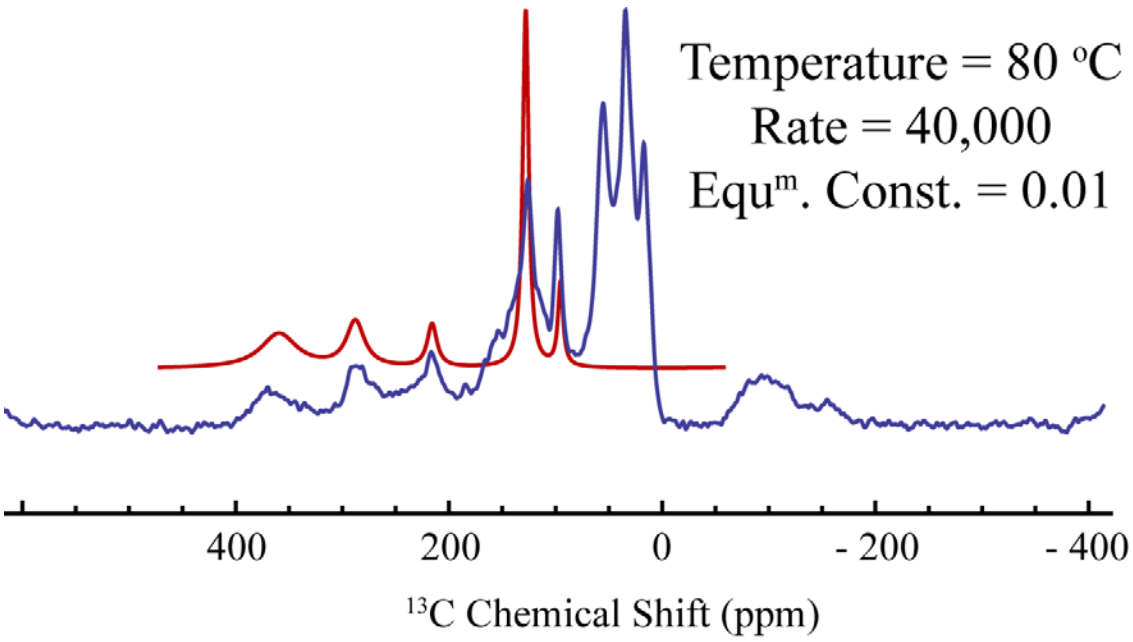

Figure 2.13 Experimental data (in blue) and simulated spectrum (in red) at 80 ˚C. the rate constant is keep fixed at 40000, and the equilibrium constant is 0.01

2.6 Conclusion

Butyl-substituted spiro-biphenalenyl radicals are the best known neutral organic radical conductors and have potential application in the materials industry. These molecules show an interesting phase change from the non-conducting diamagnetic state to the conducting paramagnetic state, as a function of temperature. Since the NMR signal depends on the electronic environment, changes in the amount of unpaired electron spin in a radical conductor changes the position and the width of NMR lines. This effect is called paramagnetic shifting and broadening of the NMR signal. Movement of electron spin between Phenalenyl rings of these molecules with changes in temperature causes the spin Hamiltonian to fluctuate randomly. Since the rate of fluctuation is much higher than the difference in chemical shift at higher temperatures, average exchange narrowed peaks are seen in the NMR spectra. This chapter shows the application of solid state NMR spectroscopy in the study of such dynamic systems and leads to a new hypothesis that the electron is actually exchanging between the rings rather than being fully delocalized over both rings at all times. The ideas discussed in this chapter can be further extended to study other paramagnetically active compounds, such as natural organic matter containing clays and metallo-proteins.

REFERENCES

(1) Garito, A. F.; Heeger, A. *J. Acc. Chem. Res.* **1974**, *7*, 232.

(2) Haddon, R. C. *Acc. Chem. Res.* **1992**, *25*, 127.

(3) Wolf, S. A.; Awschalom, D. D.; Buhrman, R. A.; Daughton, J. M.; von Molnar, S.; Roukes, M. L.; Chtchelkanova, A. Y.; Treger, D. M. *Science* **2001**, *294*, 1488-1495.

(4) Haddon, R. C. *Nature* **1975**, *256*, 394.

(5) Ohashi, K.; Kubo, T.; Masui, T.; Yamamoto, K.; Nakasuji, K.; Takui, T.; Kai, Y.; Murata, I. *Journal of the American Chemical Society* **1998**, *120*, 2018-2027.

(6) Andrews, M. P.; Cordes, A. W.; Douglass, D. C.; Fleming, R. M.; Glarum, S. H.; Haddon, R. C.; Marsh, P.; Oakley, R. T.; Palstra, T. T. M.; Schneemeyer, L. F.; Trucks, G. W.; Tycko, R.; Waszczak, J. V.; Young, K. M.; Zimmerman, N. M. *J. Am. Chem. Soc.* **1991**, *113*, 3559.

(7) Cordes, A. W.; Haddon, R. C.; Oakley, R. T.; Schneemeyer, L. F.; Waszczak, J. V.; Young, K. M.; Zimmerman, N. M. *J. Am. Chem. Soc.* **1991**, *113*, 582.

(8) Oakley, R. T. *Can. J. Chem.* **1993**, *71*, 1775.

(9) Itkis, M. E.; Chi, X.; Cordes, A. W.; Haddon, R. C. *Science* **2002**, *296*, 1443-1445.

(10) Sitzmann, H.; Bock, H.; Boese, R.; Dezember, T.; Havlas, Z.; Kaim, W.; Moscherosch, M.; Zanathy, L. *J. Am. Chem. Soc.* **1993**, *115*, 12003.

(11) Koutentis, P. A.; Chen, Y.; Cao, Y.; Best, T. P.; Itkis, M. E.; Beer, L.; Oakley, R. T.; Brock, C. P.; Haddon, R. C. *J. Am. Chem. Soc.* **2001**, *123*, 3864.

(12) Peierls, R. E. *Quantum theory of solids*; Clarendon Press: Oxford,, 1956.

(13) Chi, X.; Itkis, M. E.; Patrick, B. O.; Barclay, T. M.; Reed, R. W.; Oakley, R. T.; Cordes, A. W.; Haddon, R. C. *J. Am. Chem. Soc.* **1999**, *121*, 10395.

(14) Chi, X.; Itkis, M. E.; Kirschbaum, K.; Pinkerton, A. A.; Oakley, R. T.; Cordes, A. W.; Haddon, R. C. *Journal of the American Chemical Society* **2001**, *123*, 4041-4048.

(15) Krober, J.; Codjovi, E.; Kahn, O.; Groliere, F.; Jay, C. *Journal of the American Chemical Society* **1993**, *115*, 9810-9811.

(16) Torrance, J. B. *Acc. Chem. Res.* **1979**, *12*, 79.

(17) Stocklein, W.; Seidel, H.; Singel, D.; Kendrick, R. D.; Yannoni, C. S. *Chemical Physics Letters* **1987**, *141*, 277-282.

(18) Thier, K. F.; Mehring, M. *Physical Review B* **1994**, *50*, 2142-2149.

(19) Fukui, K.; Sato, K.; Shiomi, D.; Takui, T.; Itoh, K.; Gotoh, K.; Kubo, T.; Yamamoto, K.; Nakasuji, K.; Naito, A. *Synth. Met.* **1999**, *103*, 2257.

(20) Fischer, G.; Dormann, E. *Synthetic Metals* **1999**, *103*, 2172-2175.

(21) Kaiser, A.; Dormann, E. *Physical Review B* **2005**, *71*, -.

(22) Morita, Y.; Nishida, S.; Fukui, K.; Hatanaka, K.; Ohba, T.; Sato, K.; Shiomi, D.; Takui, T.; Yamamoto, G.; Nakasuji, K. *Polyhedron* **2005**, *24*, 2194-2199.

(23) Nishida, S.; Morita, Y.; Ueda, A.; Kobayashi, T.; Fukui, K.; Ogasawara, K.; Sato, K.; Takui, T.; Nakasuji, K. *Journal of the American Chemical Society* **2008**, *130*, 14954-+.

(24) Bertini, I.; Luchinat, C.; Aime, S. *Coordination Chemistry Reviews* **1996**, *150*, R7-+.

(25) Bertini, I.; Luchinat, C.; Rosato, A. *Advances in Inorganic Chemistry, Vol 47* **1999**, *47*, 251-282.

(26) Bertini, I.; Emsley, L.; Lelli, M.; Luchinat, C.; Mao, J. F.; Pintacuda, G. *Journal of the American Chemical Society* **2010**, *132*, 5558-+.

(27) Bezsonova, I.; Forman-Kay, J.; Prosser, R. S. *Concepts in Magnetic Resonance Part A* **2008**, *32A*, 239-253.

(28) Wilkens, S. J.; Xia, B.; Weinhold, F.; Markley, J. L.; Westler, W. M. *Journal of the American Chemical Society* **1998**, *120*, 4806-4814.

(29) Lin, I. J.; Xia, B.; King, D. S.; Machonkin, T. E.; Westler, W. M.; Markley, J. L. *Journal of the American Chemical Society* **2009**, *131*, 15555-15563.

(30) Bertini, I.; Luchinat, C. *NMR of paramagnetic molecules in biological systems*; Benjamin/Cummings Pub. Co.: Menlo Park, Calif., 1986.

(31) Bothnerby, A. A.; Domaille, P. J.; Gayathri, C. *Journal of the American Chemical Society* **1981**, *103*, 5602-5603.

(32) Volkman, B. F.; Wilkens, S. J.; Lee, A. L.; Xia, B.; Westler, W. M.; Beger, R.; Markley, J. L. *Journal of the American Chemical Society* **1999**, *121*, 4677-4683.

(33) Banci, L.; Bertini, I.; Luchinat, C. *Nuclear and electron relaxation : the magnetic nucleus-unpaired electron coupling in solution*; VCH: New York, N.Y., 1991.

(34) Fermi, E. *Nature* **1930**, *125*, 16-16.

(35) La Mar, G. N.; Horrocks, W. D.; Holm, R. H. *NMR of paramagnetic molecules; principles and applications*; Academic Press: New York,, 1973.

(36) Machonkin, T. E.; Westler, W. M.; Markley, J. L. *Inorganic Chemistry* **2005**, *44*, 779-797.

(37) Kostic, M.; Pochapsky, T. C. *Paramagnetic Resonance of Metallobiomolecules* **2003**, *858*, 214-+.

(38) Laws, D. D.; Bitter, H. M. L.; Jerschow, A. *Angewandte Chemie-International Edition* **2002**, *41*, 3096-3129.

(39) Tishmack, P. A.; Bugay, D. E.; Byrn, S. R. *Journal of Pharmaceutical Sciences* **2003**, *92*, 441-474.

(40) Kervern, G.; Pintacuda, G.; Zhang, Y.; Oldfield, E.; Roukoss, C.; Kuntz, E.; Herdtweck, E.; Basset, J. M.; Cadars, S.; Lesage, A.; Coperet, C.; Emsley, L. *Journal of the American Chemical Society* **2006**, *128*, 13545-13552.

(41) Huang, W. L.; Schopfer, M.; Zhang, C.; Howell, R. C.; Todaro, L.; Gee, B. A.; Francesconi, L. C.; Polenova, T. *Journal of the American Chemical Society* **2008**, *130*, 481-490.

(42) Van Geet, A. L. *Analytical Chemistry* **1970**, *42*, 679-680.

(43) Van Geet, A. L. *Analytical Chemistry* **1968**, *40*, 2227-2229.

(44) Raiford, D. S.; Fisk, C. L.; Becker, E. D. *Analytical Chemistry* **1979**, *51*, 2050-2051.

(45) Bersohn, M.; Baird, J. C. *An introduction to electron paramagnetic resonance*; W. A. Benjamin: New York,, 1966.

(46) Weil, J. A.; Bolton, J. R. *Electron paramagnetic resonance : elementary theory and practical applications*; 2nd ed.; Wiley-Interscience: Hoboken, N.J., 2007.

(47) Royal Society of Chemistry (Great Britain) In *Specialist periodical report.*; Royal Society of Chemistry: Cambridge, UK, 1998, p v.

CHAPTER III

SOLID-STATE PHOTOCHEMICAL AND PHOTOMECHANICAL PROPERTIES OF MOLECULAR CRYSTAL NANORODS COMPOSED OF ANTHRACENE ESTER DERIVATIVES: NMR CRYSTALLOGRAPHY

3.0 ABSTRACT

A series of 9-anthracene esters that can be prepared as nanorods and display significant photomechanical response while remaining intact are investigated in this chapter. In order to determine the molecular-level motions that give rise to the nanorod photomechanical response, the reaction of 9-tertbutyl-anthracene-ester is studied in detail using solid-state NMR techniques and X-ray diffraction. The photomechanical response of the nanorods is driven by a metastable crystalline intermediate that slowly converts into the low energy dimer crystal structure over the course of weeks. Based on the experimental data, coupled with *ab initio* calculations, we find that the intermediate is most likely the [4+4] photodimer that retains the orientation and packing of the monomer pair precursor, but has not yet undergone the ester group rotations and repacking necessary to form the final product crystal. Calculations based on this structure can reproduce the experimental values for the maximum shape change associated with

nanorods composed of 9-tertbutyl-anthracene-ester. The tilt of the reactive pair relative to the nanorod axis is crucial for generating the large expansions seen in nanorods composed of 9-tertbutylanthracene. Our results show that even though the photomechanical response of the molecular crystal nanostructures cannot be predicted based solely on knowledge of the equilibrium reactant and product crystals, it is still possible to quantitatively connect the molecular-level motions associated with the photochemical reaction in the crystal to the photomechanical motions of the nanostructure.

3.1 Introduction

Organic solid-state photoreactions have long served as a testbed for theories about how spatial constraints influence chemical reactivity. [1-3] Reactions in the crystal provide an environment where the positions and orientations of both the reactant and product molecules can be determined to atomic precision using x-ray diffraction (XRD) analysis. But the study of photochemical reactions in organic crystals is hampered by the tendency of such crystals to shatter under illumination. This fragmentation is believe to result from the build-up of interfacial strain between reacted and unreacted regions of the crystal, and the resulting phase reconstruction leads to fracture and decomposition. [4] Attempts to circumvent this problem using irradiation in the long-wavelength tail of the reactant absorption[5,6], or using two-photon absorption[7], have been successful only in a few select cases. On the whole, observations of single crystal-to-crystal phototransformations of macroscopic organic molecular crystals remain relatively rare. But interest in such photoreactive systems is increasing because of their possible use as photomechanical transducers[8], providing an alternative type of material to complement well-known polymer based photomechanical materials. [9-14] Reversible photomechanical changes were first observed in charge-transfer crystals[15] and later workers have exploited photoinduced charge transfer dynamics to drive rapid mechanical motions in microcrystals.[16,17] Recently, Irie and others have demonstrated that the reversible ring

opening/closing reaction in diarylethene derivatives[18] can be used to drive shape changes and induced motions in single crystals. [19-22] Thermally reversible photoinduced motion has also been observed in single crystals of an azobenzene derivative[23], while dramatic bending motions have been observed in crystals composed of the photodimerized analog of the Green Fluorescence Protein chromophore. [24] These examples show that it is possible to find molecules that can undergo physical rearrangements large enough to induce crystal deformation, but not so large that they disrupt the overall crystal integrity.

The use of nanostructured molecular crystals provides a general way to harness organic solid-state photochemical reactions to generate larger motions and perhaps do useful work on submicron lengthscales. But there are still several outstanding scientific questions in this work. First, how general is this phenomenon – can it be extended beyond the two molecules (9TBAE and 9AC) studied thus far? Second, what is the molecular-level mechanism that underlies the observed photomechanical response? The role of molecular alignment within the nanorods, the nature of the crystal-to-crystal transformation, and the ability to predict the magnitude of the physical displacements are all open questions raised by our previous work. In this work, we attempt to address these questions in a systematic way, primarily using ssNMR techniques coupled with *ab initio* calculations. Professor Bardeen's group have concluded that there exists a large family of anthracene ester derivatives, crystallizing in a variety of packing motifs, that can be

formed into nanorods and that exhibit a significant photomechanical response. In order to better understand the molecular level origins of the photomechanical response, we study the 9TBAE system in detail. Using solid-state Nuclear Magnetic Resonance (SSNMR) and XRD, it was found that the monomer nanorods consist of ordered single crystal domains, and that irradiation leads to a continuous transition into a second crystalline form. Surprisingly, our SSNMR data show that the crystal formed immediately after photoreaction of the monomer solid is not the same as the crystal obtained by crystallization of the photodimer directly from solution. The photomechanical response is actually determined by a crystalline intermediate that converts into the low-energy polymorph only after a period of months. The creation of metastable intermediate crystal structures via the solid-state photoreaction appears to be a general feature of the anthracene esters. Detailed comparison of our data with *ab initio* calculations and partially converted crystal data provide a model for the structure of this intermediate. Calculations based on the proposed intermediate structure are consistent with the observed changes in nanorod length and diameter upon irradiation. Our results provide a molecular-level mechanism for the photomechanical response observed in this class of molecules. An important conclusion is that the photomechanical response of this class of materials cannot be predicted based on equilibrium structures of the reactant and product molecular crystals, but instead arises from nonequilibrium crystal structures

whose characterization is quite challenging. The results in this research establish the generality of the anthracene esters as a versatile family of compounds which are capable of forming photoactive organic nanorods and indicate that a deeper understanding of solid-state reactivity is required to gain a predictive understanding of how solid-state photochemistry gives rise to micron-scale motions.

3.2 Experimental

3.2.1 Synthesis of Materials

The anthracene-9-carboxylic acid esters (1, 2, 7-13) were synthesized and the nanorods were prepared by Professor Christopher Bardeen's group at UC Riverside [Zhu, L.; Agarwal, A.; Lai, J.; Al-Kaysi, R.; Tham, F.; Ghaddar, T.; Mueller, L. J.; Bardeen, C. J. "Photochemical and photomechanical properties of molecular crystal nanorods of anthracene ester derivatives", Submitted, J. Am. Chem. Soc., 2010.].

3.2.2 ^{13}C Solid-State Nuclear Magnetic Response (SSNMR) measurements

Cross-polarization (CP) magic-angle-spinning (MAS) solid-state NMR experiments were performed at 14.1T (^{1}H frequency 600 MHz) on a Bruker AVANCE spectrometer equipped with a double-resonance 2.5 mm MAS probe, spinning at a magic angle spinning (MAS) rate of 27 kHz to avoid the overlap of spinning sidebands. 83 kHz ^{1}H $\pi/2$ and decoupling pulses were used along with a 2 ms CP spin-lock. During CP the

^{13}C nutation rate was set to 40.5 kHz and the ^{1}H nutation rate ramped from 58 kHz – 77 kHz. For each spectrum, 4096 complex data points with a dwell of 12.5 μs (spectral width 40 kHz, total acquisition time 51.26 ms) were acquired with a recycle delay of 5 s for a total experiment time of 5 hours and 45 minutes. A pulse diagram for Cross-polarization is shown in Figure 3.1.

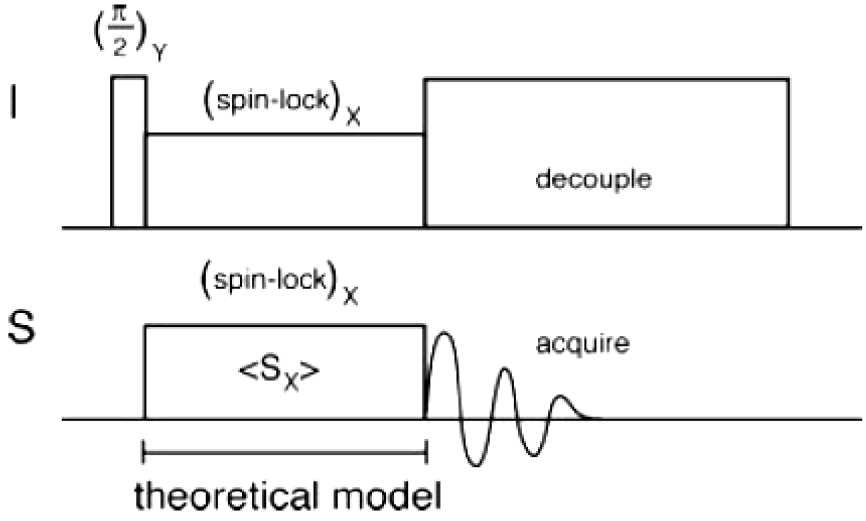

Figure 3.1 A typical CP pulse sequence diagram

3.2.3 *Chemical Shift Calculations*

Ab initio calculations were performed at the density functional (DFT) level of theory using the B3LYfunctional [25-27] within the Gaussian 03 software package.[28] Molecules were optimized to their ground state geometries using the 6-31G(d,p) basis

and NMR chemical shifts calculated with the 6-311++G(d,p) basis. Once the calculations are done, the results can be read in the form of a log file on a notepad. The calculated chemical shifts can then be plotted on any graphing software. The final spectra can be generated by adding Gaussians or Lorentzians lineshapes to the obtained shifts. Calculated ^{13}C chemical shifts were referenced to benzene at 128.0 ppm from TMS.

3.3 Results and Discussion

Figure 3.2 shows the molecular structures of the compounds studied in our work. We are interested in the anthracene esters because they comprise a family of compounds whose molecular structure and crystal packing can be tuned by changing the ester group

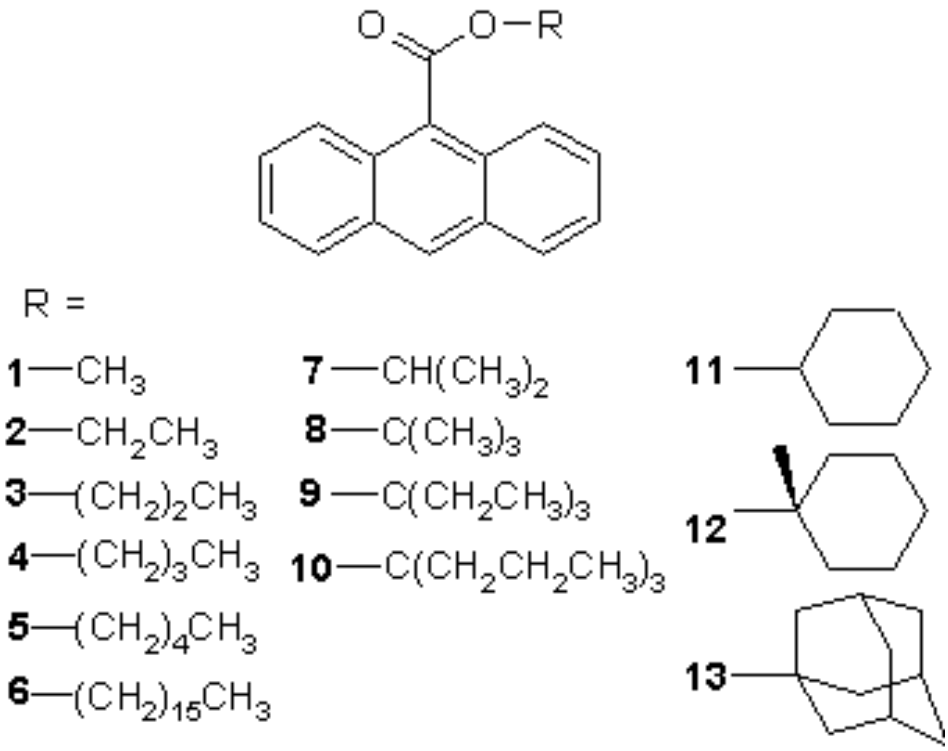

Figure 3.2 Molecular structures of anthracene esters studied in this chapter.

attached at the 9-anthracene position. They are highly soluble and, as shown in Figure 3.4, amenable to nanorod growth. This family of compounds was previously studied in the context of solid-state triboluminescence[29], but here we are concerned with their solid-state photochemistry. The ester substituents can be divided into three broad classes: n-alkyl chains (**1**-**6**), branched alkyl chains (**7**-**10**), and cyclohexyl derivatives (**11**-**13**). Single crystal XRD was used by our collaborators to determine the crystal structures for all the molecules in Figure 3.2. The photoreactive molecules crystallized into one of the two basic crystal classes summarized in Figure 3.3: herringbone pair (HBP) and layered pair (LP).

The other molecules crystallized into structures where either neighboring

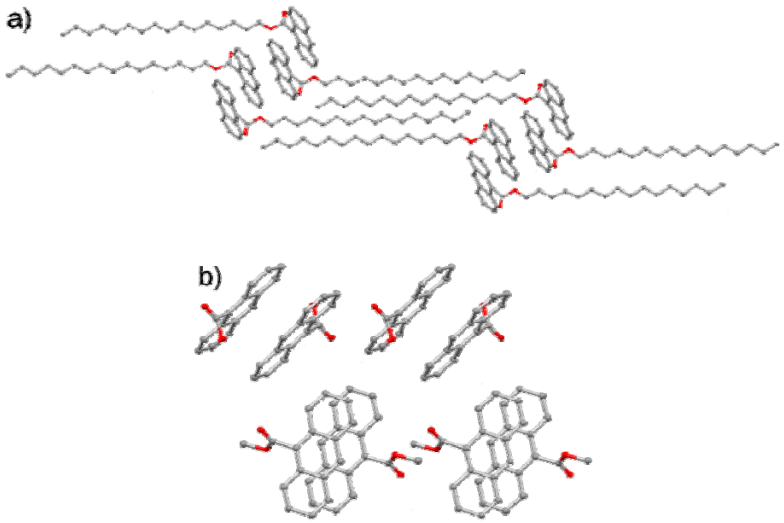

Figure 3.3 Crystal packing motifs of the two classes of photoreactive anthracene esters: a) Layered Pair (6); b) Herringbone Pair (1)

anthracene rings were not cofacial, for example herringbone packing (**2**) or where the anthracene rings were too far away from each other to react (**10**, **13**). Note that the distance limit for photodimerization is estimated to be 4.7 Å.[30] One sign that a solid would be reactive was a yellow color and yellow-green fluorescence, indicating excimer formation due to interacting anthracene π systems. As found by our collaborators, in one case (**13**), the room temperature crystal was unreactive, but the growth of a different polymorph inside the AAO could be induced by modifying the nanorod growth conditions. For **13**, this entailed simply placing a microscope coverslip underneath the AAO template during the solvent annealing step. This polymorph was found to be photoreactive, but its structure remains unknown since we were unable to grow bulk crystals. A second point is that while molecules **4** and **5** were photoreactive in the solid, their very low melting points prevented observation of a mechanical response. The melting points of antracene ester derivatives are shown in table 3.1.

Table 3.1 Melting point of **1** to **13**

Anthracene Esters	Melting Point (C°)
1	110~111
2	112~113
3	74~76
4	44.5~46
5	42~43
6	56.5~57
7	92.5~93.5
8	158~159
9	126~127
10	105.5~106.5
11	125~126
12	124~125
13	211~212

The n-butyl and n-pentyl groups appear to lead to a high amount of packing disorder, making it difficult to grow single crystals and impossible to grow nanorods. All the photoreactive molecules (**1**-**3**, **6**-**12** and the photoreactive polymorph of **13**) could be formed into 200 nm diameter nanorods using solvent annealing methods in AAO templates. SEM images of some representative examples are shown in Figure 3.4 for completeness.

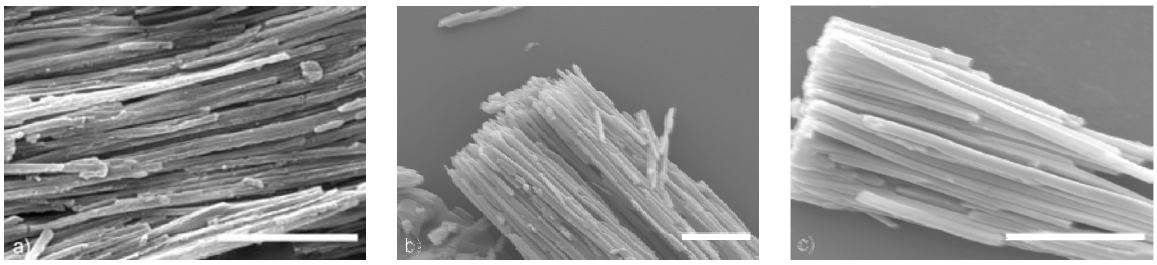

Figure 3.4 SEM images of 200nm nanorods composed of different anthracene esters: a) **7**; b) **11**; c) **12** (Scale bas is 5 μm)

In these samples, where the rods are clustered together, it was observed that over the course of several weeks, individual rods would sometimes merge with neighboring rods to form larger diameter crystals. This indicates that the nanorods are not the equilibrium structure, and that the molecules retain some mobility and the ability to merge into larger crystals in the absence of the template constraints.

When nanorods composed of photoreactive molecules were exposed to 365 nm light in a fluorescence microscope, they typically underwent movement and expanded in length. Bundles tended to separate under the influence of the light (Figure 3.5; Atomic Force Microscopy of nanorod **8**).

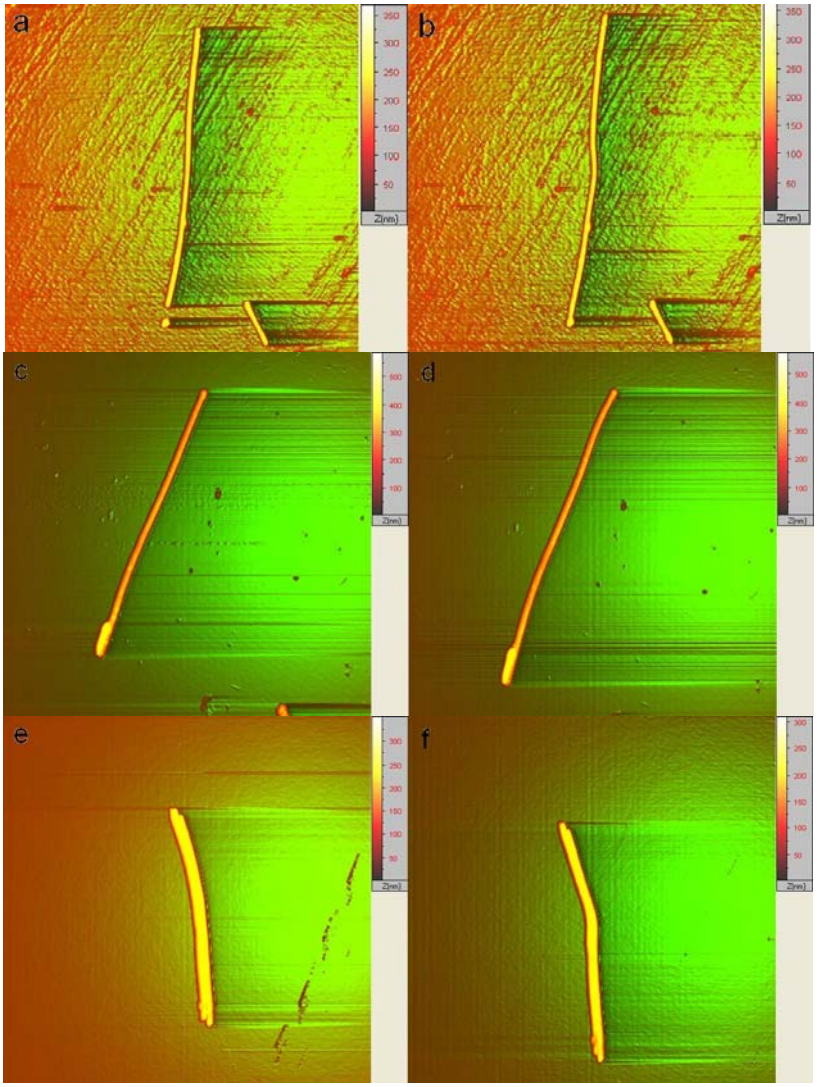

Figure 3.5 AFM images of (a, b) nanorod **8** expands by 11.5% after irradiation; (c, d) nanorod **8** expands by 10.5% after irradiation; (e, f) nanorod **8** expands by 9% after irradiation. The expansion of nanorods varies from rod to rod which may be due to the varying crystalline nature of nanorods and their degree of surface adhesion.

But the rods retained their shape and did not break. It was found that the amount of length change for a given molecular crystal nanorod varied within a sample. For example, for nanorods composed of **12**, expansions ranged from 5% to 25%. This variability has also been observed in rods composed of 9AC that undergo reversible bending. [31] Variations in crystallinity or the degree of surface adhesion have been identified as possible factors that contribute to the observed variability. Nevertheless, we can say that the anthracene-9-carboxylic acid esters form a large family of compounds that can be solvent annealed into crystalline nanorods manifesting measurable photomechanical motions in response to near-UV irradiation. Table 3.2 summarizes the properties of the molecules studied in this chapter. One surprising aspect of Table 3.2 is that the presence of a photomechanical response is not specific to a single crystal type.

Table 3.2 Properties of anthracene esters

Anthracene Esters	Crystal Packing	Photoreactivity of crystal	Nanorods Growth	Photomechanical response
1	HBP	Shatter	Yes	Yes
2	HB	No Response	Not attempted	-
3	LP	Shatter	Yes	Yes
4	HBP	Melt	No	-
5	LP	Melt	No	-
6	LP	Shatter	Yes	Yes
7	HBP	Shatter	Yes	Yes
8	HBP	Shatter	Yes	Yes
9	HBP	Shatter	Yes	Yes
10	DP	No Response	Not attempted	-
11	HBP	Shatter	Yes	Yes
12	LP	Shatter	Yes	Yes
13	OHBP	Shatter*	Yes	Yes

HB = herringbone, HBP = herringbone pair, LP = layered pair, DP = distant pair where anthracenes are too far apart to react, OHBP = offset herringbone pair where anthracenes are not aligned for reaction

*photoreactivity and photomechanical response for 13 reported for polymorph with unknown crystal structure

With the photomechanical response of the anthracene ester nanorods established as a general phenomenon, the next question concerns the physical basis of this response. We have concentrated on the case of 9TBAE **8**, as a prototypical ester with a sizable photomechanical response. The room temperature single crystal XRD structure reveals rotational disorder in the tertbutyl groups that disappears at 100 K. The details of the XRD monomer crystal structure are summarized in Table 3.3. An earlier 9TBAE crystal structure[29] neglected this disorder and had larger standard deviations in the unit cell dimensions as well as a larger R1 value in comparison to our tert-butyl disordered model, which we believe is a more accurate representation of the structure of **8**. Both structures give the same overall picture of the herringbone-pair packing motif in the bulk and thus the first question concerns the form of the monomer crystal within the nanorods: is it the same as the bulk monomer crystal, and does it have a preferred orientation? The powder XRD data in Figure 3.6 answer both questions in the affirmative. The powder XRD pattern calculated from the bulk single crystal (Figure 3.6 a) structure matches up well with that obtained experimentally from the powdered nanorods (Figure 3.6 b) – all predicted diffraction peaks are observed. If the nanorods are left in the amorphous AAO template, oriented vertically relative to the scanning x-ray beam, only a single diffraction peak appears, corresponding to the (011) plane as assigned from the calculated XRD pattern (Figure 3.6 c). This plane is shown in Figure 3.6 d.

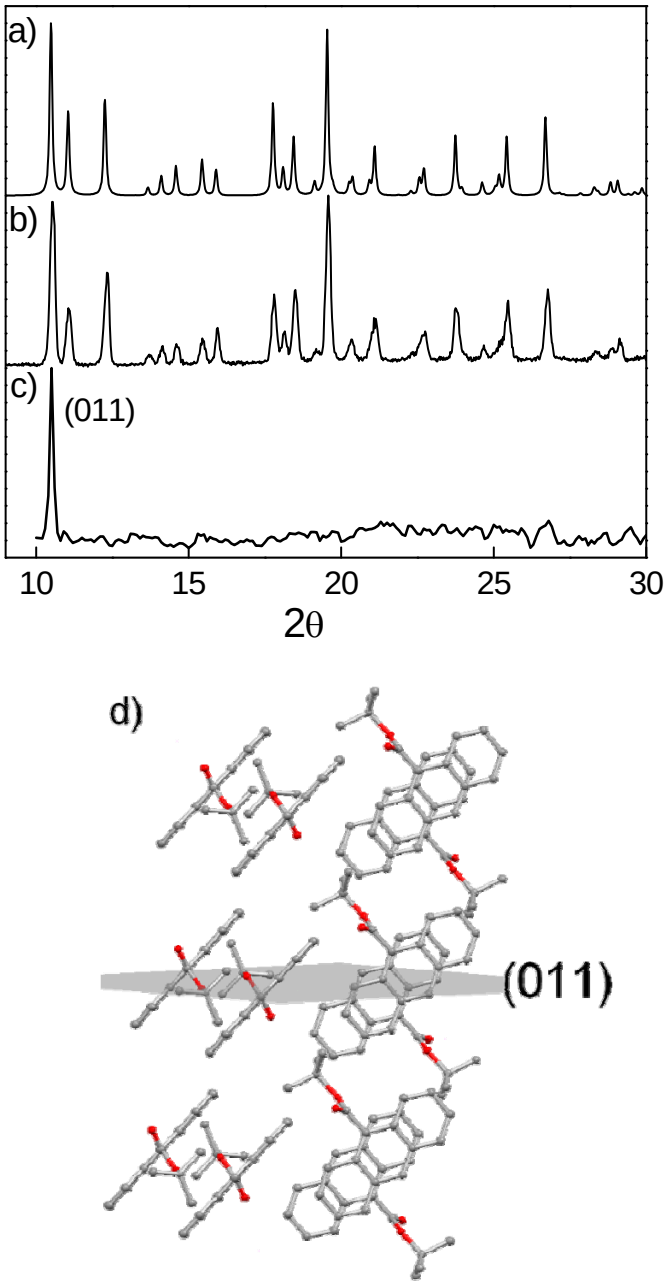

Figure 3.6 Powder X-ray diffraction patterns of 9TBAE **8** monomers: **a)** pattern of 9TBAE monomer calculated based on the single crystal structure; **b)** experimental pattern of 9TBAE monomer bulk; **c)** orientated 9TBAE monomer nanorods; **d)** orientated 9TBAE monomer nanorods in AAO template.

Table 3.3 Crystal data and structure refinement for monomer, PRD and SGD

Empirical formula	**$C_{19}H_{18}O_2$ (monomer)**	**$C_{19}H_{18}O_2$ (PRD)**	**$C_{38}H_{36}O_4$ (SGD)**
Formula weight	278.33	278.33	556.67
Temperature	296(2) K	296(2) K	100(2)K
Wavelength	0.71073 Å	0.71073 Å	0.71073 Å
Crystal system	Monoclinic	Monoclinic	Triclinic
Space group	P2(1)/n (#14)	P2(1)/n (#14)	P-1
Unit cell dimensions	a = 9.1313(7) Å, α= 90°	a = 9.1419(7) Å, α= 90°	a = 9.1605(2) Å, α= 67.1901(3)°
	b = 17.5205(14) Å, β= 99.9029(14)°	b = 17.5398(14) Å, β= 99.8192(13)°	b = 9.6923(2) Å, β= 85.3952(4)°
	c = 9.7613(8) Å, γ = 90°	c = 9.7526(8) Å, γ = 90°	c = 10.2180(3) Å, γ = 62.2311(3)°
Volume	1538.4(2) $Å^3$	1540.9(2) $Å^3$	734.34(3) $Å^3$
Z	4	4	1
Density (calculated)	1.202 Mg/m^3	1.200 Mg/m^3	1.259 Mg/m^3
Absorption coefficient	0.077 mm^{-1}	0.077 mm^{-1}	0.080 mm^{-1}
F(000)	592	592	296
Crystal size	0.20 x 0.17 x 0.10 mm^3	0.47 x 0.39 x 0.18 mm^3	0.37 x 0.25 x 0.09 mm^3
Theta range	2.32 to 24.71°	2.32 to 29.57°	2.32 to 30.50°
Index ranges	-10<=h<=10,	-12<=h<=12,	-13<=h<=13,
	-20<=k<=20,	-24<=k<=24,	-13<=k<=13,
	=-11<=l<=11	=-13<=l<=13	=-14<=l<=14
Reflections collected	23942	22802	17538
Independent reflections	2630 [R(int) = 0.0352]	4329[R(int) = 0.0192]	4448[R(int) = 0.0224]
Completeness to theta = 24.71°	100.00%	100.00%	99.70%
Absorption correction	Semi-empirical from equivalents	Semi-empirical from equivalents	Semi-empirical from equivalents
Max. and min. transmission	0.9925 and 0.9845	0.9864 and 0.9649	0.9926 and 0.9710
Refinement method	F^2	F^2	F^2
Data / restraints / parameters	2630 / 36 / 224	4329 / 230 / 260	4448 / 0 / 193
Goodness-of-fit on F^2	1.038	1.021	1.056
Final R indices [I>2sigma(I)]	R1 = 0.0470, wR2 = 0.1144	R1 = 0.0391, wR2 = 0.1062	R1 = 0.0415, wR2 = 0.1110
R indices (all data)	R1 = 0.0688, wR2 = 0.1303	R1 = 0.0644, wR2 = 0.1254	R1 = 0.0467, wR2 = 0.1155
Largest diff. peak and hole	0.361 and -0.274 $e.Å^{-3}$	0.176 and -0.122 $e.Å^{-3}$	0.460 and -0.203 $e.Å^{-3}$

The oriented, crystalline nature of individual nanorods prepared by the solvent annealing method has been previously established by TEM observations on individual rods. [32] The data in Figure 3.6 is consistent with previous powder XRD measurements on 9AC nanorods [33] and confirms that the preferential crystal orientation is a property of the entire sample and does not vary from rod to rod. When the templated nanorods are exposed to 365 nm light, the diffraction peak at 10.5^{o} disappears and a new peak grows in at 10.8^{o}. A series of powder XRD patterns showing this crystal-to-crystal transformation is shown in Figure 3.7. Analysis of the peak areas in Figures 3.7.a-f indicates that the reaction is a simple two-state process, since the exponential decay of the reactant peak is mirrored by the growth of the product peak, as shown in Figure 3.7.g.

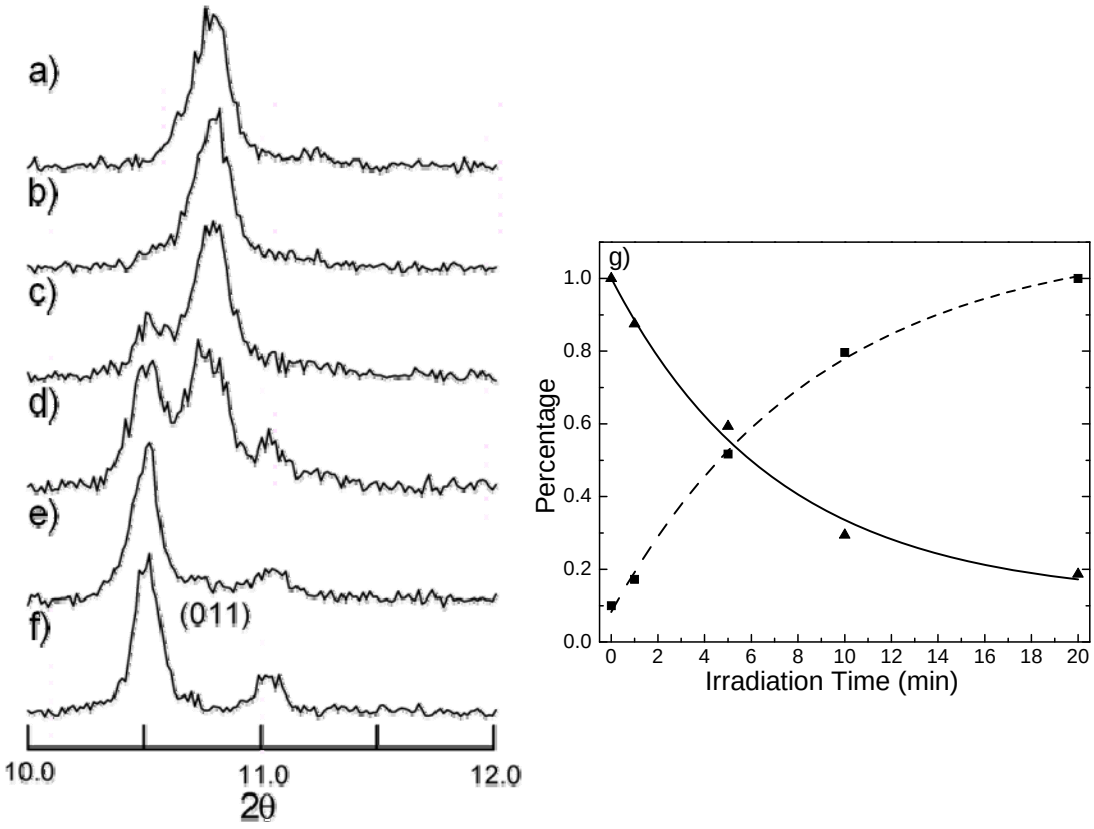

Figure 3.7 Powder X-ray diffraction patterns of single-crystal-to-single-crystal transition from orientated 9TBAE monomer nanorods to dimer: **a)** (011) peak of 9TBAE monomer nanorods before irradiation; **b)** after 1 min irradiation; **c)** after 5 min irradiation; **d)** after 10 min irradiation; **e)** after 20 min irradiation; **f)** after 1 hour irradiation; **g)** exponential fit of the decay of the monomer peak (solid line) and the growth of the dimer peak (dashed line)

When the nanorods are exposed to 365 nm light for varying time durations (from 0 hours to 24 hours), systematic changes in the ssNMR spectra of the bulk powder sample can be observed as well. A series of ssNMR spectra showing this transformation is shown in Figure 3.8 along with an expanded region of the spectra.

Figure 3.8 Solid state NMR spectra of single-crystal-to-single-crystal transition from orientated 9TBAE monomer nanorods to dimer: a) 9TBAE monomer nanorods before irradiation; b) after 1 hour irradiation; c) after 3.5 hours irradiation; d) after 5 hours irradiation; e) after 24 hours irradiation

We observe the appearance of two new sp^3 carbon resonances at 55 ppm and 65 ppm as well as at 85 ppm. There is a shift of aromatic peaks from 130 ppm to 145 ppm as well as that of the carbonyl carbon from 172.7 ppm to 176 ppm. These changes in the NMR spectra of the bulk powder sample, as a function of irradiation time, indicate that the reaction is a simple two-state process, where the photodimerized nanorod gradually forms from the 9-TBAE monomer sample. Both observations indicate that the photodimerization of solid 9TBAE results in the formation of a new crystal structure. In bulk crystals, the coexistence of the two different crystalline phases during the course of the photodimerization reaction causes the crystal to build up internal stress and shatter. The nanorods' large surface-to-volume ratio allows them to accommodate the volume changes during photodimerization and remain intact.

The next question concerns the structure and orientation of the newly formed dimer crystal, which we will refer to as the solid-state reacted dimer (SSRD). Our collaborator, Prof. Bardeen and his group found that slow evaporation of a monomer solution in n-hexane during UV irradiation could produce large photodimer crystals without solvent of crystallization molecules. This crystal structure, which we will refer to as the solution grown dimer (SGD), is shown in Figure 3.9.a.

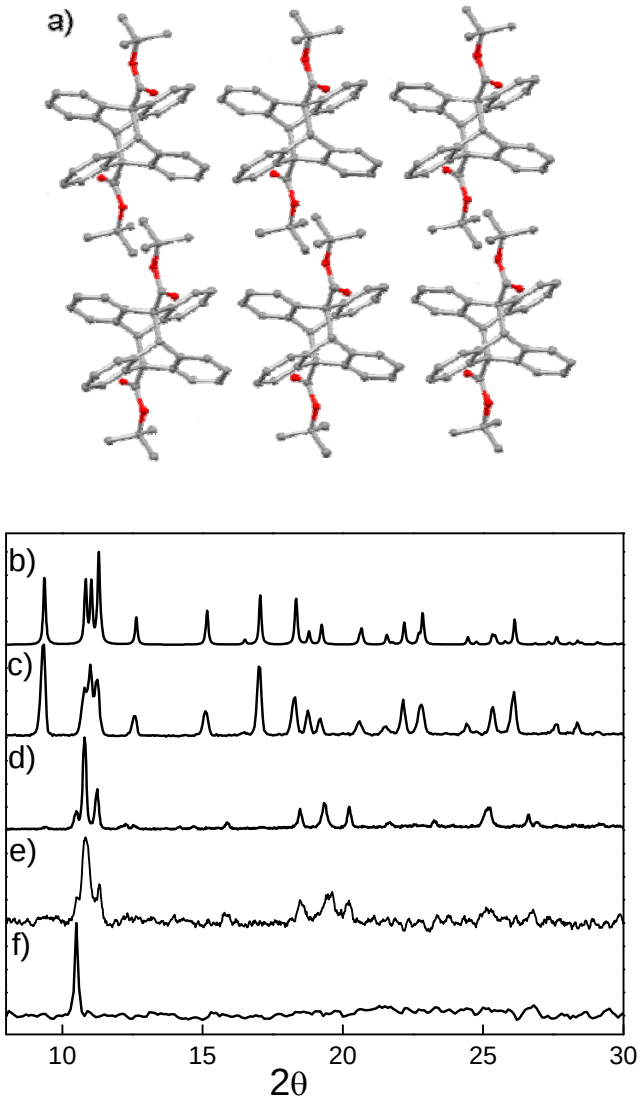

Figure 3.9 **a)** Crystal structure of solution grown dimer (SGD) from hexane; Powder X-ray diffraction patterns: **b)** calculated pattern of SGD; **c)** experimental pattern of SGD; **d)** experimental pattern of dimer nanorods; **e)** experimental pattern of SSRD bulk; **f)** experimental pattern of dimer nanorods in AAO template.

In addition to the cyclohexyl bridge structure seen in all anthracene dimers, there are two other important changes in the SGD structure when compared to the monomer crystal in Figure 3.6.d. First, the ester groups are now rotated ~180^{o} so that the tert-butyl group on one anthracene points outward, away from the neighboring anthracene. Second, the anthracene dimers have rearranged themselves from the HBP structure into a layered crystal where the anthracene rings are parallel with each other. It was seen that the volume per anthracene of the SGD is significantly smaller than that of the monomer crystal. At first glance, this result is surprising given our previous results that indicated a volume increase after irradiation. [34] But the powder XRD data make it clear that the crystal structure of the SGD is different from that of the SSRD crystal formed immediately after irradiation of the crystalline monomer. Figures 3.9.b and 3.9.c compare the calculated powder XRD pattern for the SGD to the experimental data for the powdered SGD. The good agreement between the two patterns shows that there is no systematic error in our powder XRD measurements. But when this diffraction pattern is compared to that of the SSRD, obtained either from an irradiated powder (Figure 3.9.d) or from the nanorods (Figure 3.9.e), there are clear differences in peak positions and relative intensities. Figure 3.9.f shows the powder XRD of the reacted nanorods in the AAO template, which exhibit only a single peak from the SSRD powder pattern,

providing evidence that the crystal orientation in the nanorod is retained after photoreaction.

The crystal structure of the SSRD is different from that of the SGD is further supported by SSNMR measurements. The inset in Figure 3.10 shows the carbon numbering of the carbons in **8**, while Figure 3.10.a shows the ^{13}C spectrum of a monomer crystal powder of **8**.

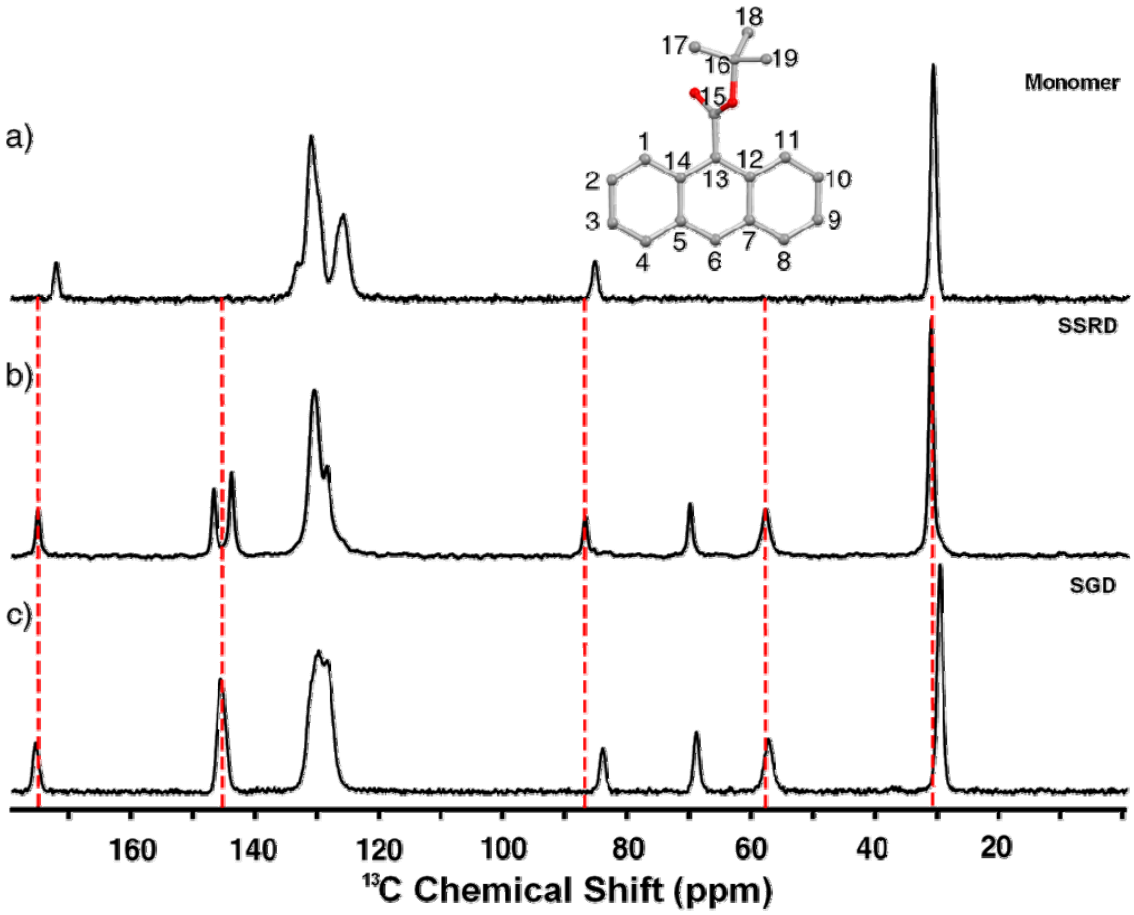

Figure 3.10 inset) carbon numbering for 9TBAE monomer; a) the ^{13}C solid state NMR spectra for the monomeric 8; b) SSRD; c) SGD. The SSRD chemical shifts for C6 (58.6 ppm); C15 (175.8 ppm); C5, C7,C12 and C14 (144.5/147.5 ppm); C16 (87.6 ppm); and C18 (31.8 ppm) are marked with red dashed lines in order to facilitate evaluations of chemical shift changes between the three species as per the discussion in the text.

When this powder is irradiated, the spectrum smoothly transforms into that in Figure 3.10.b. If, on the other hand, we irradiate the monomer in solution and grow the dimer crystal after reaction, this solid yields the SGD ^{13}C spectrum in Figure 3.10.c. Obvious changes in both Figures 3.10.b and 3.10.c include the shift of four aromatic carbons (5, 7, 12 and 14) from 130 ppm to 145 ppm due to the creation of neighboring sp^3 carbons, the appearance of 2 new sp^3 (9, 10) carbon resonances at 55 ppm and 65 ppm, and the shift of the carbonyl carbon (15) from 172.7 ppm to ~176 ppm in the dimer. In addition, two significant differences between the spectra of the SSRD and SGD should be highlighted. First, we observe a shift of the methyl carbons (17-19) from 31.5 ppm in the monomer and 31.8 ppm in the SSRD to 30.4 ppm in the SGD. A more obvious difference between the two spectra is a symmetric pairing of the sp^2 carbon peak at 145 ppm in the SSRD. This feature likely results either from a perfectly symmetrical static environment with both ester groups perpendicular to the aromatic rings, or from a fast dynamical averaging between symmetric deviations from this position. The origin of this splitting will be discussed below.

We have found that the SSRD crystal structure is metastable. Over the course of several months, both powder XRD and SSNMR measurements indicate that the SSRD slowly converts into the SGD structure, which is stable on this timescale, and also partially back to the monomer. This can be inferred from Figure 3.11, which shows a

ssNMR spectrum of SSRD after being stored in the rotor for about one year. The spectrum obtained under exactly identical conditions to that of Figure 3.10, has resemblance to both the monomer as well as the SGD. This same phenomenon has also been observed in molecules **1** and **12**, and the existence of a metastable SSRD structure that slowly relaxes to the more stable SGD structure appears to be a general feature of the anthracene esters.

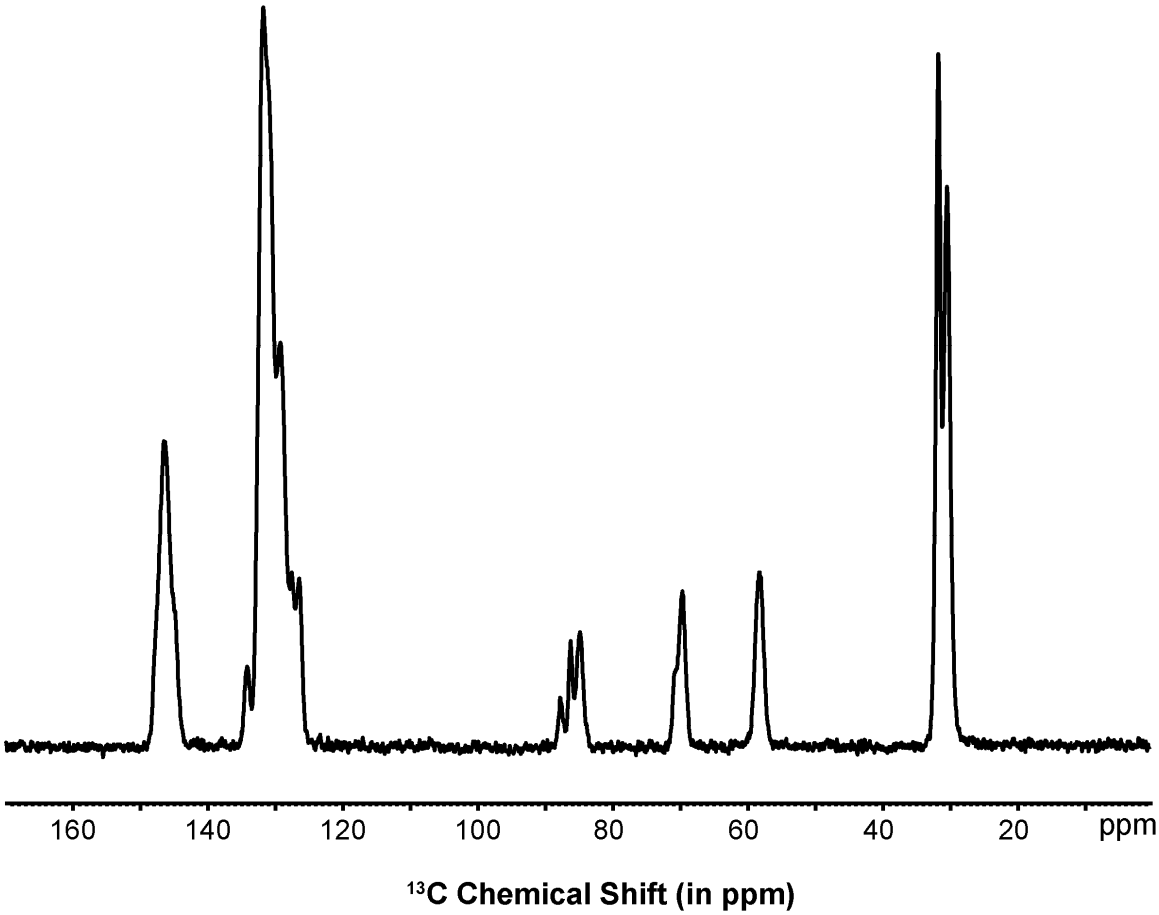

Figure 3.11 ^{13}C ssNMR spectrum of SSRD sample one year after being packed in the rotor

In an attempt to determine the structure of the SSRD, we used the long wavelength tail irradiation method to photoreact a millimeter-scale crystal without fragmenting it. Many workers have used single crystal XRD to follow the progress of solid-state photodimerization reactions, with trans-cinnamic acid derivatives comprising the most commonly studied system [35-39] in addition to other molecules.[40-43] After reacting a 9TBAE crystal under 400 nm illumination for 25min, ~20% of the crystal was converted into the dimer. The conversion was limited to about 20% due to crystal decomposition, so the reaction could not be followed to completion within a single macroscopic crystal, as seen previously for the solid-state [4+4] photodimerization of 9-methylanthracene.[42,43] The structure was solved assuming a mixture of the known monomer crystal structure and the unknown dimer. The resulting dimer structure, which we refer to as the partially reacted dimer (PRD) is shown in Figure 3.12.a with the 011 plane aligned horizontally to facilitate comparison with the monomer crystal in Figure 3.6.d. This structure is quite different from that of the SGD shown in Figure 3.9. First, the ester groups have not undergone the full 180^{o} rotation to adopt the outward-facing structure of the SGD. Second, the dimers retain the HBP packing of the monomer crystal. Thus this structure represents the structure immediately after dimerization but before ester group rotation and repacking can occur.

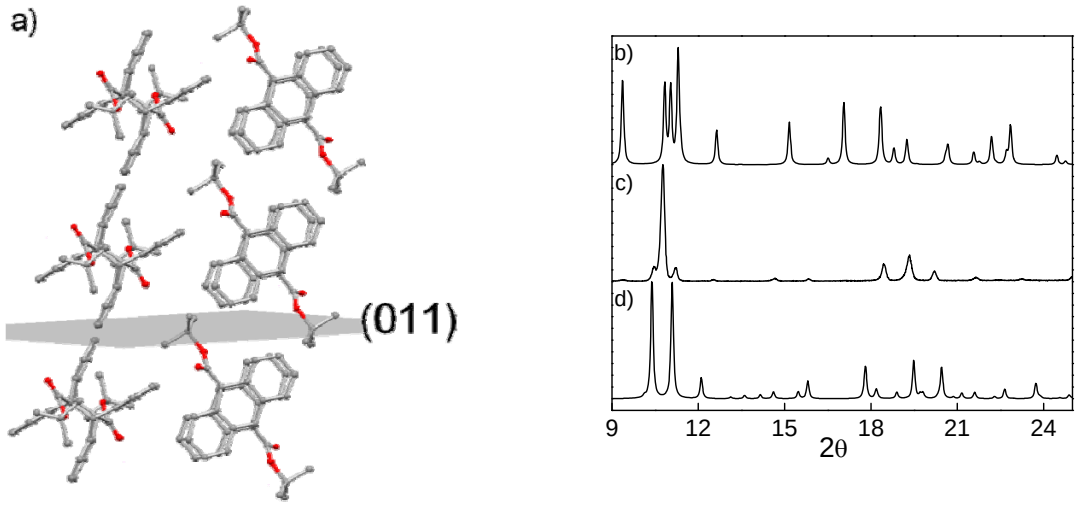

Figure 3.12 **a)** Crystal structure of solid-state intermediate dimer (PRD); **b)** calculated powder XRD pattern from SGD; **c)** experimental powder XRD pattern from SSRD; **d)** calculated powder XRD pattern from the PRD structure.

The ssNMR data suggest that the PRD and SSRD have similar structures. This can be established from closer examination of the ^{13}C chemical shifts obtained from SSNMR experiments. SSNMR experiments have been used successfully to analyze both geometry changes and reaction dynamics, particularly in the trans-cinnamic acid [2+2] photodimerization [39,44-47], but also for 9-methylanthracene.[48] In conjunction with *ab initio* calculations of the chemical shifts, these experiments can provide constraints on the molecular geometry.[49] Table 3.4 summarizes the experimental chemical shifts for the assigned carbons, along with the theoretically calculated values.

Table 3.4 Experimental chemical Shifts (ppm) for SSRD and SGD, and theoretical chemical shifts calculated for 0° rotation (inward-facing) ester group, and 180° rotation (outward-facing) ester group. The theoretical chemical shift of carbon C18 actually is the average chemical shift of carbons 17, 18, and 19, which are not resolved experimentally.

	Experimental		Theoretical	
	SSRD	SGD	0 degree	180 degree
C1			127.3	128.3
C2			125.0	124.7
C3			125.4	125.5
C4			127.8	126.7
C5	144.5	146.3	145.7	147.5
C6	58.6	58.0	57.1	55.6
C7	144.5	146.3	145.7	147.5
C8			127.8	126.7
C9			125.4	125.5
C10			125.0	124.7
C11			127.3	128.3
C12	147.5	146.3	150.0	149.5
C13	70.6	69.6	70.3	70.5
C14	147.5	146.3	150.0	149.5
C15	175.8	176.2	176.2	177.6
C16	87.6	84.8	84.1	83.8
C17				
C18	31.8	30.4	23.1	22.8
C19				

Note that we have not tried to resolve individual shifts in the crowded aromatic region around 130 ppm. To begin, we first note that the ^{13}C chemical shift of the methyl groups (carbons 17-19) for the monomer and SSRD solids are almost identical, within 0.3 ppm of each other. The chemical shift of the SGD methyls is more than 1 ppm upfield, easily seen in the experimental data in Figure 3.10. It is expected that these carbons will be sensitive to their crystal environment, and this explains why the calculated shifts for the isolated molecules are different from the experimental values. For these carbons, proximity to the aromatic rings will tend to shift the resonances slightly downfield. Thus both the monomer and SSRD methyl peak shifts are consistent with inward-facing tert-butyl groups, rather than the outward-facing tert-butyl groups in the SGD. Second, the pronounced symmetric pair at ~145 ppm in the SSRD is condensed into a single, broader peak in the SGD spectrum. This chemical shift corresponds to the sp^2 carbons on both sides of the newly formed sp^3 carbons in the photodimer (carbons 5, 7, 12 and 14). For any stationary structure, where the esters are asymmetrically tilted (e.g. all 3 structures for the monomer, PRD, and SGD), these four carbons would have distinct but similar chemical shifts. One way the symmetric splitting could arise is from a stationary structure where the ester groups are exactly symmetric (i.e. perpendicular) with respect to the anthracene rings. A second scenario that would give rise to the larger splitting is for the carbons to be dynamically averaged, most likely due to symmetric motion of the ester

groups from the perpendicular position. The question then becomes whether it is possible to distinguish between the outward-facing ester groups (180^o rotation from the monomer, as in the SGD) and the inward-facing ester groups (0^o rotation, corresponding to the PRD). From the theoretical values, we see that the splitting between carbons 5/7 and 12/14 is predicted to be larger for the 0^o ester (4.3 ppm) than for the 180^o ester (2.0 ppm), similar to what is observed for the SSRD (3.0 ppm) versus the SGD (<1.0 ppm). This agreement between the calculated trend in chemical shifts for the 0^o and 180^o ester conformations and that seen experimentally for the SSRD and SGD line positions extends to other carbons as well. For the carbonyl carbon 15, the theoretical shift from 0^o to 180^o is +1.4 ppm, versus +0.4 ppm experimentally for the SSRD versus the SGD. For carbon 6, theory predicts a shift of -1.5 ppm, while experimentally the shift is -0.6 ppm. For carbon 16, theory predicts a shift of -0.3 ppm, while experimentally the shift is -2.8 ppm. The only carbon for which theory predicts the opposite shift from what is observed experimentally is carbon 13, where the theoretical shift is +0.2 ppm while experimentally the shift from SSRD to SGD is -1.0 ppm. But this carbon, where the ester is attached to the anthracene, is particularly sensitive to ester rotation. We find that if other motions up to 30^o are taken into account, the carbon-13 shift for the 0^o structure shifts downfield by 1.0 ppm or more, which would lead to better agreement between theory and experiment. All these small changes can be summarized by calculating a reduced χ^2 values for the

comparison of the SSRD spectrum to the 0^o and 180^o calculated spectra. Using the values for the assigned carbons (except methyls) in Table 3.4, and assuming a variance of 2.0 ppm, we obtain a reduced χ^2 for the SSRD/0^o chemical shift comparison of 0.95 ppm, as opposed to a reduced χ^2 for the SSRD/180^o chemical shifts of 1.3 ppm. This lower reduced χ^2 value indicates that the 0^o calculation provides a better fit for the SSRD data. While these values are not different enough to conclusively say that the SSRD structure is closer to the PRD than to the SGD, taken with the methyl chemical shift differences and the likely averaging of the ester-adjacent sp^2 carbons, the SSNMR data provides circumstantial evidence that the PRD is closer to the SSRD structure than is the SGD.

Based on the powder XRD and SSNMR analysis, we tentatively assign the SSRD structure to be similar to the PRD structure in Figure 3.12.a. It is possible that further conversion of the monomer beyond 20% would generate lattice strain[50] and open up the crystal packing enough to allow the dynamic ester rotation we infer from the SSNMR spectrum and also cause slight changes in packing that can account for the differences between the calculated PRD powder XRD pattern and the experimental powder SSRD pattern. In order to illustrate the sequence of steps that occur after photoexcitation of **8** in the crystal, Figure 3.13 shows several views of the structures involved in the transformation, from the unreacted monomer pair (Figure 3.13.a), to the PRD (Figure 3.13.b), and finally to the fully converted equilibrium dimer structure of the SGD (Figure

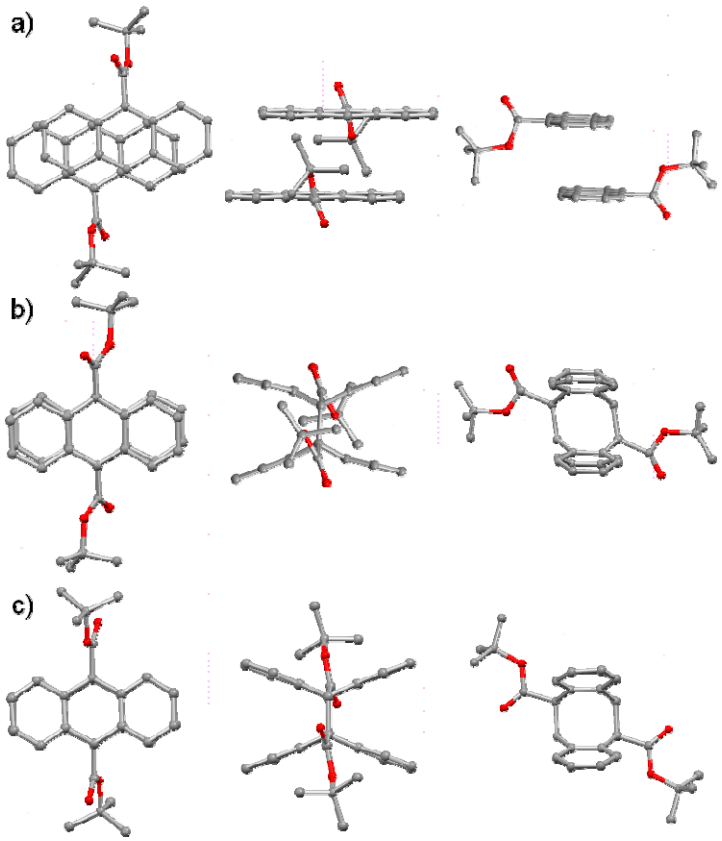

Figure 3.13 Three different views of the reactive molecular pairs obtained from the crystal structures of **a)** monomeric **8**; **b)** the PRD; **c)** the SGD.

3.13.c). Upon irradiation, the two molecules that compose the dimer pair in Figure 3.13.a must undergo two movements. First, the two anthracene rings must shift during the [4+4] dimerization reaction so that the new bonds can form. Second, the newly formed sp^3 carbons force the anthracene rings into a nonplanar "butterfly" conformation, as seen in Figure 3.1.3.b. We hypothesize that both of these processes are rapid (<< 1s) at room temperature and drive the formation of the SSRD, similar to the PRD structure, immediately after the photoreaction. After the formation of the cyclohexyl ring between

the anthracenes, the newly formed dimer molecules must execute two additional motions in order to eventually reach the low energy SGD conformation. First, the tert-butyl ester groups must rotate ~180^{o} from inward-facing with respect to the anthracene sandwich pair to an outward-facing position with the alkyl sidechains going diagonally up and away from the anthracene pair. *Ab initio* calculations have determined the barrier for this rotation is approximately 10 kcal/mole, suggesting that this motion would be slow at room temperature in the isolated molecule, and even slower in the dense crystal environment. Second, the dimer molecules must reassemble into the layered structure shown in Figure 3.9.a. We hypothesize that both processes are very slow compared to the formation of the photodimer, which leaves the solid trapped in the metastable SSRD structure for a period of months.

Now that we have an idea of the SSRD structure, we still need to explain the large (up to 15%) length expansion seen in nanorods composed of **8** (figure 3.5). For molecules like the diarylethenes, where the intramolecular photochemistry leaves the macroscopic crystals intact, it is possible to obtain the exact crystal structures of both the reactant and product molecules.[51] If this is the case, then it is possible to map the changes in molecular packing onto the macroscopic crystal deformations. [19,52] For **8**, where we cannot obtain an intact crystal of the SSRD, we must rely on coarser measurements of the molecular structure and infer how changes in structure and packing

affect the nanorod dimensions. Based on crystal data and structural refinement data, it would appear that the net volume change between monomer, PRD, and SGD is remarkably small. Thus it would appear that a simple explanation based on volume expansion of the crystal is insufficient to explain the observed expansion of the nanorods composed of **8**. But a detailed examination of the geometrical changes within a single reactive pair, as outlined in Figure 3.14, provides a plausible mechanism for both the increase in length and decrease in diameter of a nanorod observed in our previous paper.

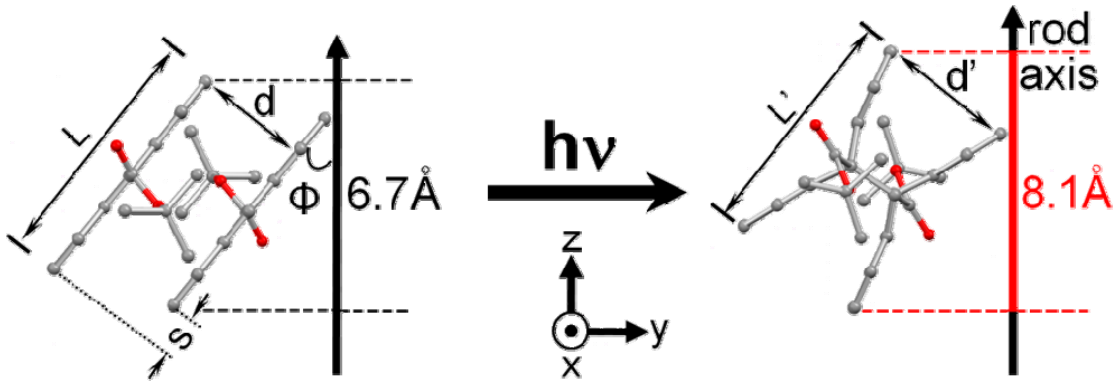

Figure 3.14 Schematic of the geometrical changes for a reactive pair in the monomeric and PRD crystal structures, with the angle ϕ with respect to the rod axis is assumed to be the same (40.1°) for both structures. The separation of the outermost atoms of the anthracene rings changes from d=3.48 Å to d'=4.24 Å, the length of the pair changes from L=7.27 Å to L'=7.00 Å, and the slip goes from s=1.44 Å in the monomer pair to s=0.0 Å in the photodimer. The photodimer expansion causes the projection of the pair onto the z-axis to increase from 6.7 Å to 8.1 Å.

From the crystal structure in Figure 3.6.a, we find that a given monomer pair is tilted at an angle ϕ=40.1° with respect to the rod axis. Furthermore, this monomer pair is separated by a distance d=3.48 Å and is also misaligned as seen in Figure 3.13.a. The

anthracene moieties are offset by 1.44 Å along their long axis and by 0.67 Å along their short axis (the short axis corresponds to the x-axis perpendicular to the plane of the figure). We only consider the longer "slip" s = 1.44 Å in order to simplify the analysis. The length of an anthracene ring is found to be L=7.27 Å. It is straightforward to calculate the projection of this monomer pair onto the z-axis, which corresponds to the long axis of the rod, and the y-axis, which corresponds to the rod diameter. We find that the z-projection is 6.7 Å and the y-projection is 8.3 Å. After irradiation, we assume that the PRD dimer structure is formed, and that the anthracene moieties make the same angle (40.1^{o}) with respect to the rod (z) axis. In this case the anthracene rings are aligned, so s=0.0, and we have new values for the length L' and the effective separation d'. L' is smaller since the anthracenes are now bent by the creation of the central sp^3 carbons. For this new butterfly structure, we find L'=7.00 Å. But this puckering of the anthracene rings also dramatically increases the separation of their outer atoms, with d'=4.24 Å. Taken together with $\phi=40.1^{o}$, these new values of L' and d' lead to a z-projection of 8.1 Å and a y-projection of 7.8 Å. If the change in the z-projection of the dimer is assumed to be directly proportional to the nanorod length change, we find that a 20% increase in length is predicted. Note that the increased z-projection results mainly from the increase in d' due to the distortion of the anthracene ring from planarity. For the diameter change, we first recognize that the herringbone pair packing motif means that half of the pairs

contract along the y-axis while the other half contract along the x-axis. This assumes that the pairs are exactly 90^{o} to each other, which is not exactly the case but is close. Thus we assume that only half the pairs undergo the 6.5% contraction implied by the monomer and the PRD y-projection values. This means that the average contraction along the rod diameter is only ~3.2%. Both of these predicted values (20% length expansion accompanied by a 3.2% diameter contraction) are in reasonable agreement with the experimental values (15% and 3.5%, respectively).

As mentioned above, the experimental values can vary from rod to rod, and our comparison to this theory concerns only rods where the maximum expansion was observed. This should be the most appropriate comparison, as the theoretical values do not take into account factors like defects, imperfect alignment, and incomplete reaction yields, all of which would reduce the observed expansion. Of course, final proof for this mechanism requires the exact structure of the SSRD. We are currently pursuing a multi-pronged effort to understand the structure of this intermediate crystal using computational methods subject to the constraints provided by SSNMR and XRD measurements. In the meantime, the geometry changes outlined in Figure 3.14 provide a plausible way for the nanorods to elongate in the absence of a large unit cell expansion. It is interesting that the key ingredient for nanorod expansion in this model is the tilt of the reactive pair combined with the expansion (from d to d') due to the butterfly motion of the anthracene

rings. If the anthracene rings had a different tilt angle ϕ with respect to the rod axis, we would predict a different value of the photomechanical expansion. If $\phi=90^{o}$, for example, we would predict a 22% expansion, while if $\phi=0^{o}$, we would predict a contraction of the rod. Thus the overall photomechanical behavior of the nanostructure is intimately tied to both the molecule-level motions induced by the photochemical reaction and to the orientation of the crystal within the nanostructure.

3.4 Spin Relaxation and its measurement:

3.4.1 Theory

Spin relaxation times depend on the local structural environment of molecules. Thus, having knowledge about the relaxation times in solids can give some information on the local dynamics of the nanorods. With this motivation in mind, we decided to make some T_1 measurements on the nanorod samples.

The radio frequency pulse perturbs the equilibrium state of nuclear spins. When the radio frequency pulse is not applied on the sample, the spins want to come back to their equilibrium position. In order to recover back to equilibrium, they have to dissipate all the excess energy they collected as a result of pulsing. This process is called relaxation. When the relaxation involves recovery of bulk magnetization along z-axis, it is called longitudinal relaxation. This process brings the nuclear system back to

equilibrium by losing heat energy into the surroundings. Due to this very reason, Longitudinal relaxation is also known as Spin-Lattice relaxation (more so in reference to ssNMR).

Using Bloch equations, the rate of recovery of bulk magnetization in the z-direction (M_z, the z-component of magnetization) for its return to equilibrium can be expressed as a 1st order rate

$$\frac{d(M_z)}{d\tau} = \frac{(M_0 - M_Z)}{T_1} \qquad \textbf{[3.1]}$$

This results in an exponential curve of the recovery of magnetization by stimulated emission of excess energy.

$$M_0 - M_Z(t) = [M_0 - M_Z(0)]\exp\left(-\frac{\tau}{T_1}\right) \qquad \textbf{[3.2]}$$

3.4.2 Measurement of T_1 using Inversion Recovery Sequence:

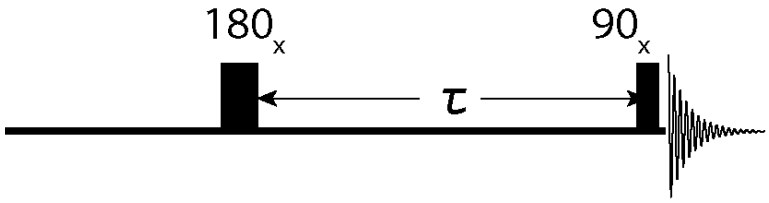

Figure 3.15 Basic Inversion Recovery pulse sequence

A basic pulse sequence for the measurement of Spin-lattice relaxation time is shown in figure 3.15[53]. This sequence is called the inversion recovery pulse sequence. It

is also used to selectively suppress the unwanted spin signals. This sequence perturbs the equilibrium and then detects the resulting magnetization as a function of variable delay τ. The first 180° radio frequency pulse rotates the equilibrium bulk magnetization vector +M0 to –M0. The width of this pulse is optimized to be equal to π i.e.

$$\gamma B_1 t_p = \pi \qquad \textbf{[3.3]}$$

This means the upper energy level is more populated than the lower level (inverse Boltzmann distribution). After a variable time interval (τ), the recovery of equilibrium magnetization shows an exponential behavior:

$$M_z(t) = M_0 \left[1 - 2 \exp\left(\frac{-\tau}{T_1}\right)\right] \qquad \textbf{[3.4]}$$

The (π/2) read pulse creates observable NMR signal in the form of M_y magnetization. It is clear from the previous equation that the NMR signal starts at the maximum negative intensity and exponentially convert to maximum positive intensity, going through zero. A not so accurate but easy way to estimate T_1 values can be employed by the use of null time, the cross-over time at which the intensity of NMR signal goes to zero.

$$T_1 = \frac{\tau_{null}}{\ln 2} \qquad \textbf{[3.5]}$$

Information regarding the structure and dynamics of molecules and the corresponding spin system is related to relaxation rates. Keeping this in mind, we made an elaborate effort to measure the T_1 times of all the peaks in the nanorod samples of varying dimer percentages. We used cross-polarization pulse sequence right after the inversion recovery sequence to transfer the magnetization of ^{1}H onto ^{13}C, which was then detected. Once the spectra were obtained, they were fit to Gaussian line functions, with some initial guess as shown below (Figure 3.16):

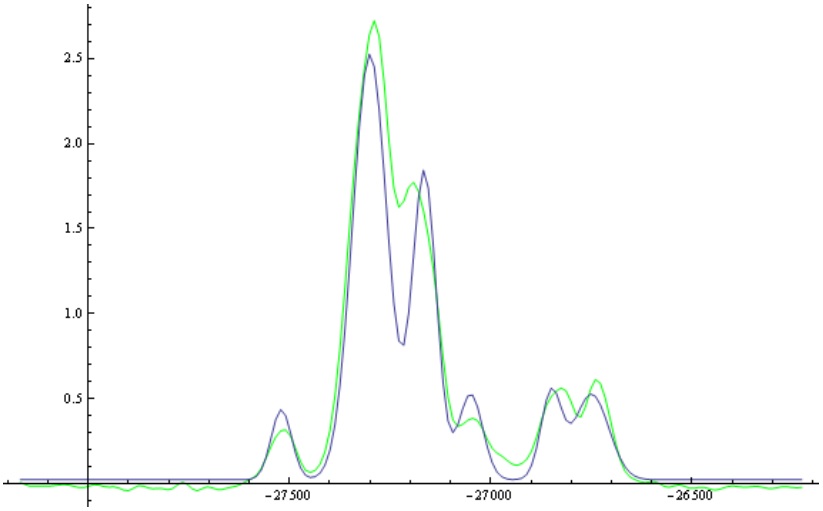

Figure 3.16 Spectral fit with initial guess

After going through an optimization on Mathematica, a more accurate fit is generated as shown below (figure 3.17).

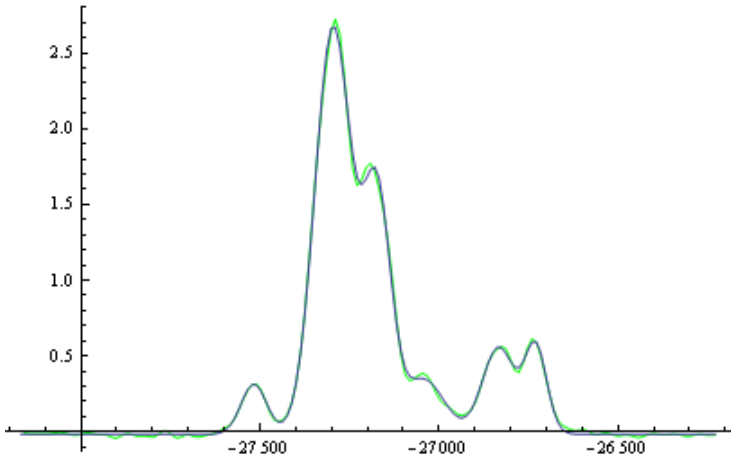

Figure 3.17 Actual fit

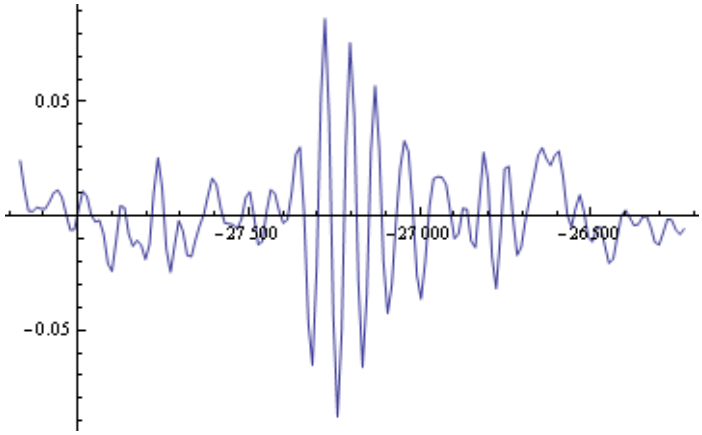

Figure 3.18 Residual of the fit

A residual of this fit to the original peaks is shown above (Figure 3.18).

The obtained intensities are then plotted as a function of variable delay, τ. Non-linear regression of this curve to fit equation [3.4] gives the value of T_1 for the corresponding peaks. A model plot is shown below for completeness:

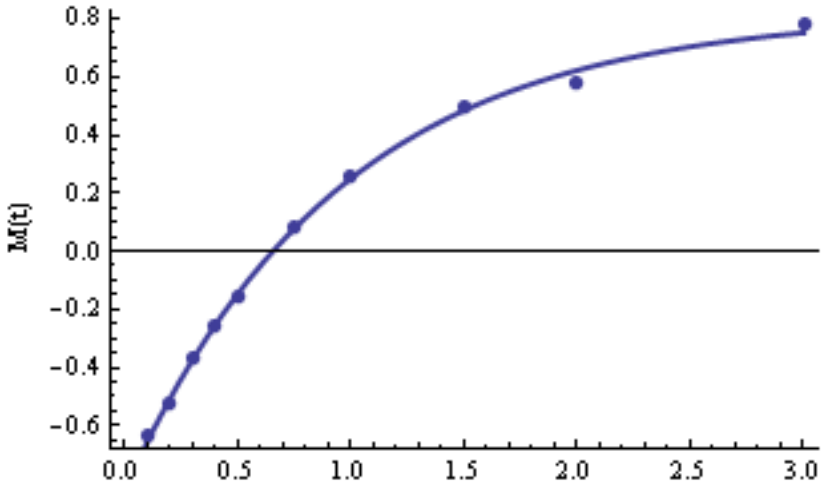

Figure 3.19 Exponential fit for T_1 measurement

Figures 3.20-3.24 reports the spin-lattice relaxation times of all the corresponding peaks (in seconds). Figure 3.25 shows a plot of relaxation times for the different peaks in various samples of the nanorods. It was plotted in this fashion to see how relaxation times correlate in these samples. However, the interpretation of T_1 with respect to structural properties is rather complex and not very well understood, unlike chemical shift and spin-spin coupling interactions. As a result we could not make any conclusive remarks on this part of the study.

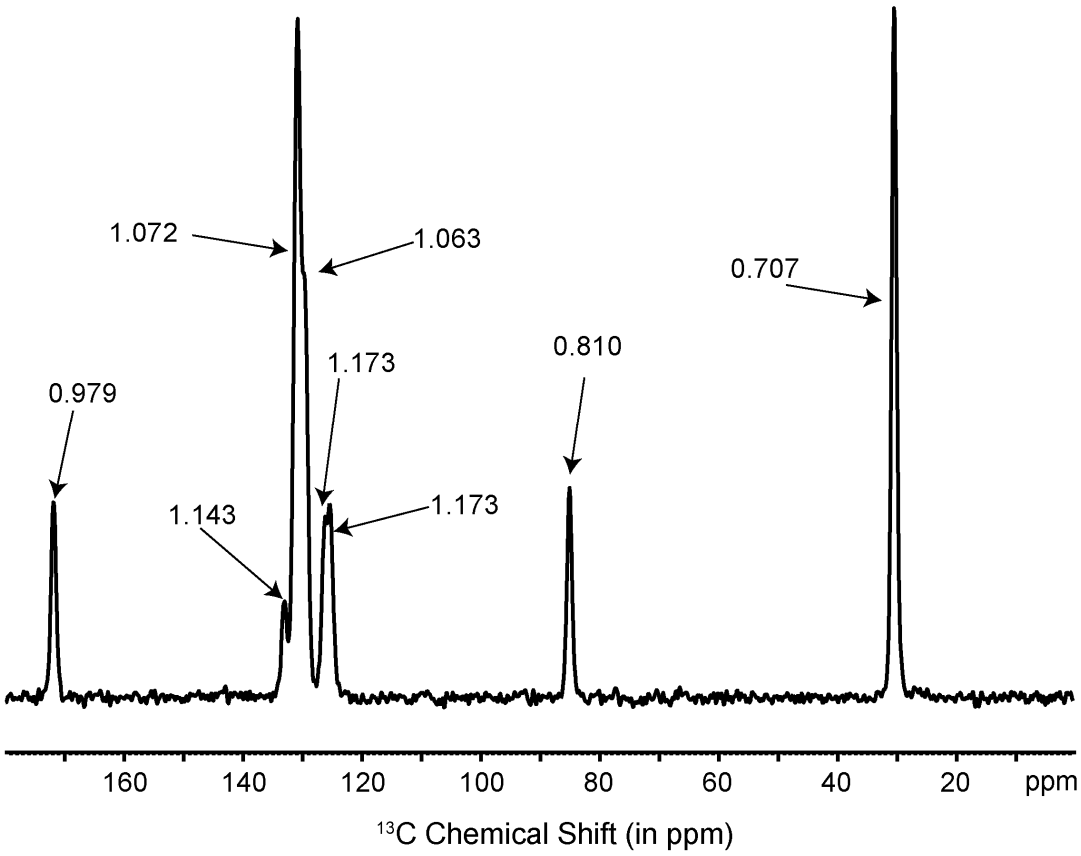

Figure 3.20 T_1 relaxation time (in sec.) for 0% dimer sample (i.e. all monomer)

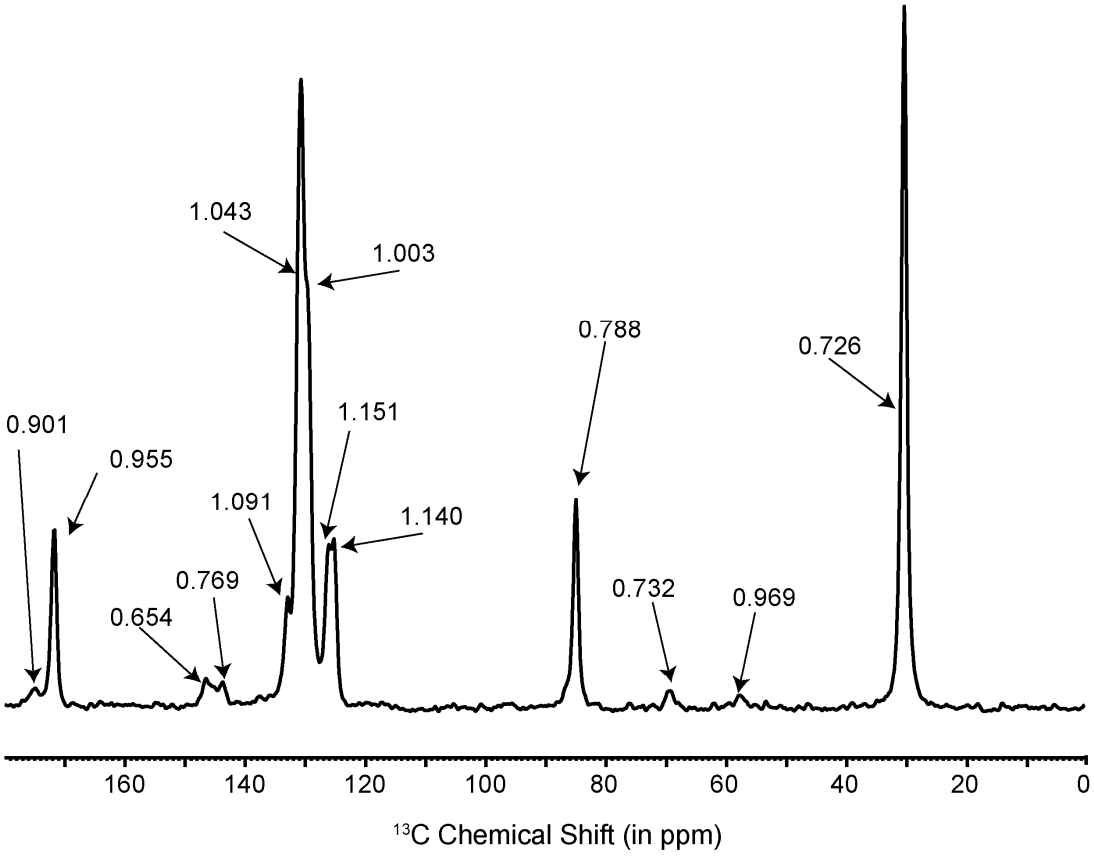

Figure 3.21 T_1 relaxation time (in sec.) for 5% dimer sample

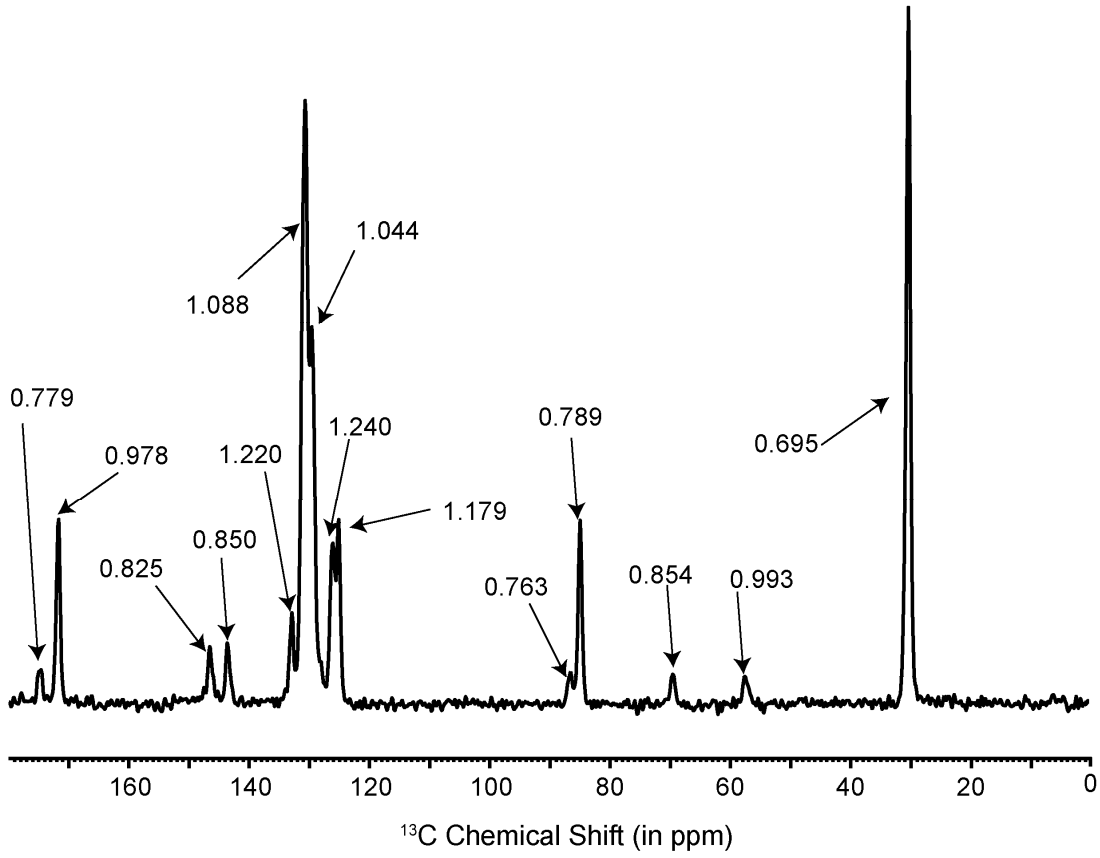

Figure 3.22 T_1 relaxation time (in sec) for 15% dimer sample

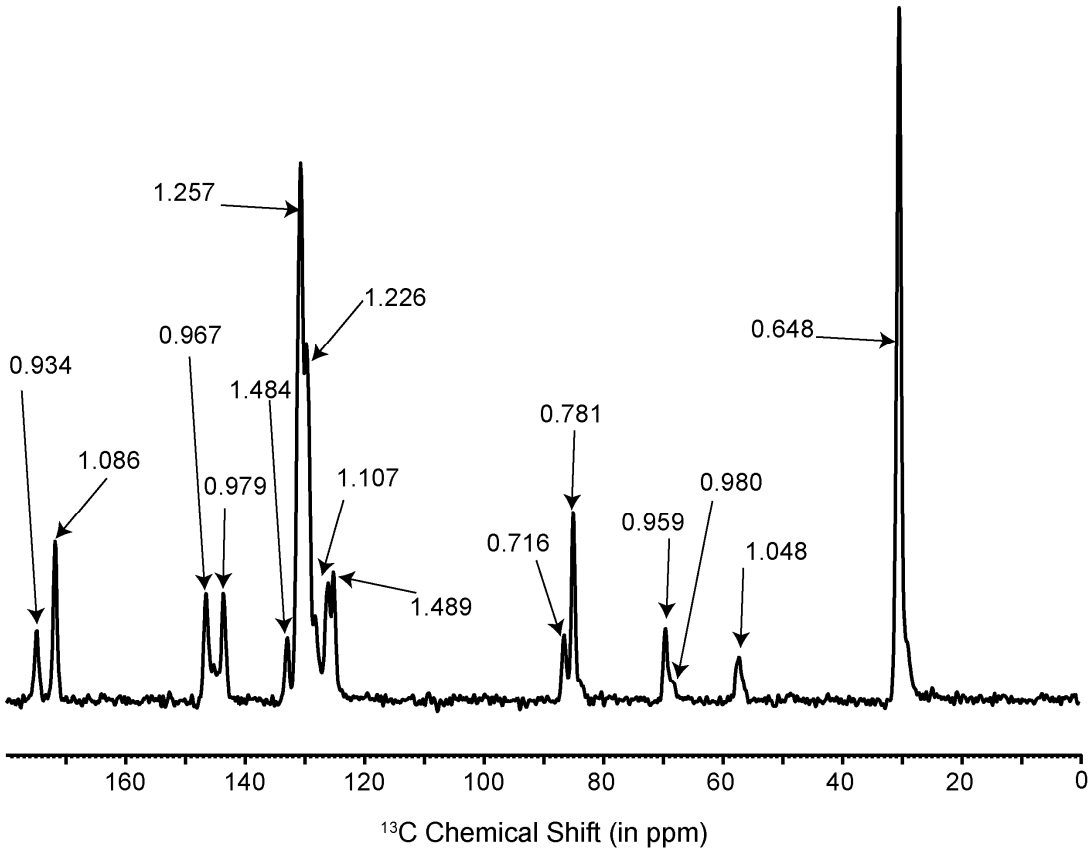

Figure 3.23 T_1 relaxation time (in sec) for 20% dimer sample

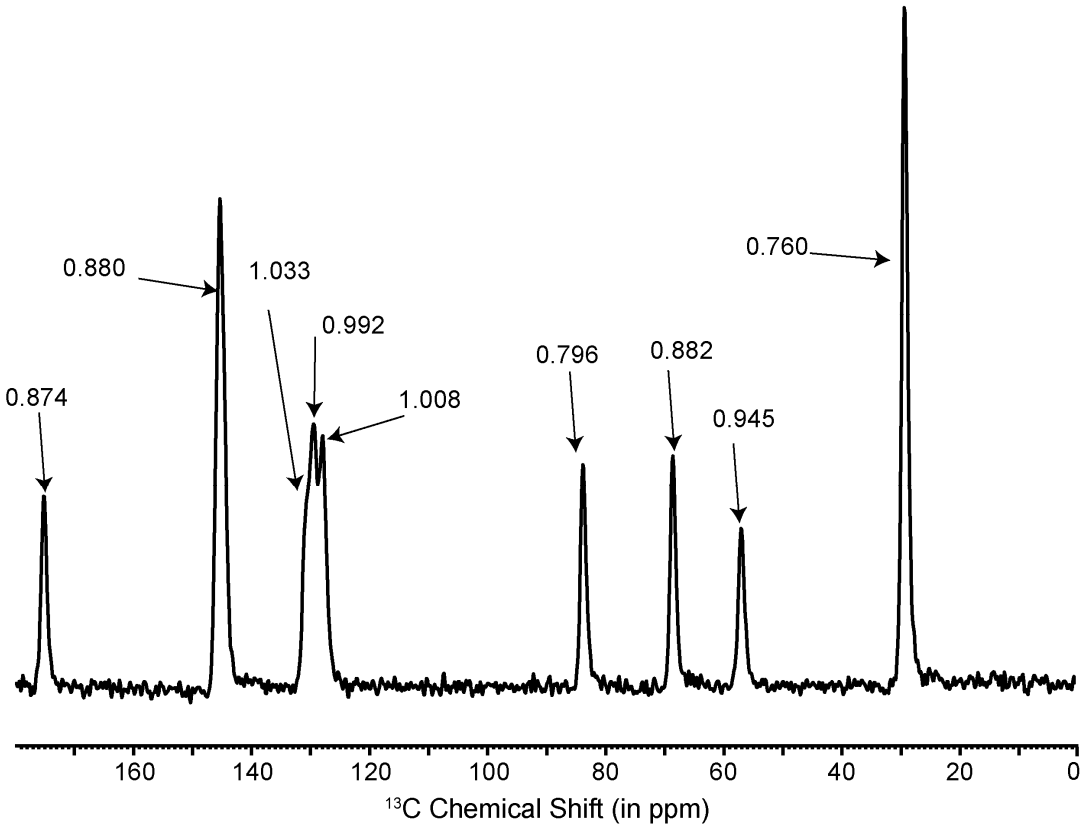

Figure 3.24 T_1 relaxation time (in sec) for 100% solid state dimer sample

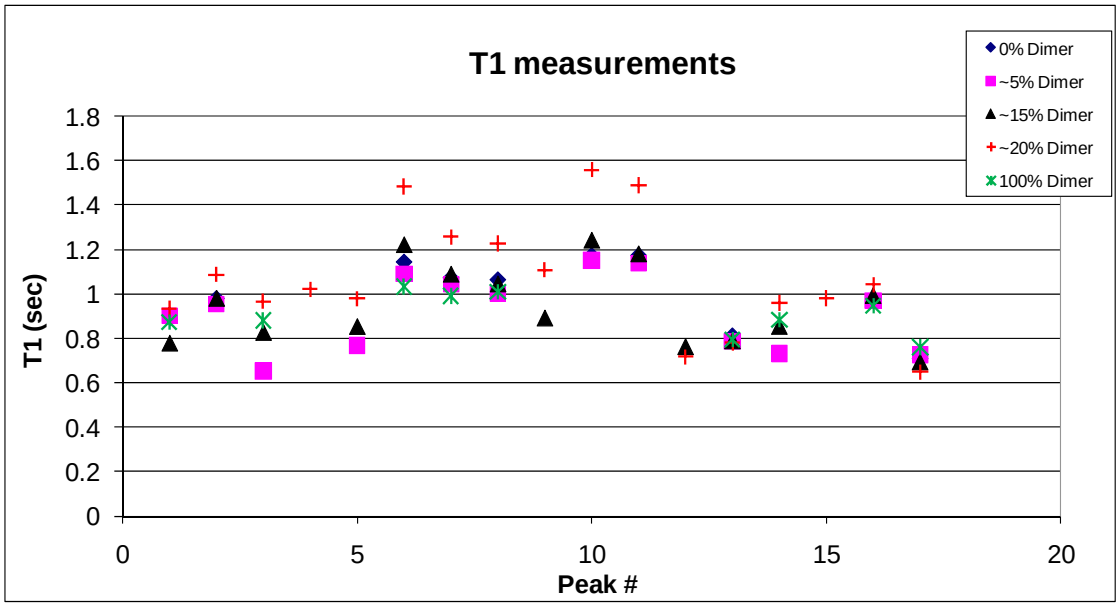

Figure 3.25 Graph of Relxation times (in seconds) of various peaks in nanorod samples

3.5 Conclusions

This study explains the photophysics of photomechanically responsive molecular crystal nanostructures based on anthracene esters.[34] These molecules form a versatile family of compounds that can be formed into photoresponsive nanorods despite variations in molecular structure and crystal packing motifs. A detailed study of 9TBAE **8** provides significant insight into the molecular-level dynamics that give rise to the micron-scale response of the nanorods. The photomechanical response of the nanorods is determined by a metastable crystalline intermediate (SSRD) that slowly converts into the low energy solution grown dimer (SGD) crystal structure over the course of weeks. We have used a variety of experimental measurements to establish the structural characteristics of the SSRD. Based on SSNMR data and powder XRD, coupled with *ab initio* calculations, we find that the SSRD is most likely the [4+4] photodimer that retains the orientation and packing of the monomer pair precursor, with a long lifetime before largescale ester rotations and repacking can take place. Calculations based on this structure can reproduce the experimental values for the maximum shape change associated with nanorods composed of **8**. We find that the large expansions seen in nanorods composed of molecule **8** arise from the tilt of the reactive pair relative to the rod axis combined with the puckering of the anthracene rings after the [4+4] photodimerization that increases their projection along the rod axis. While consistent

with our observations, conclusive proof for this mechanism must await detailed structural information on the SSRD intermediate. But we can already draw two important lessons from our work. First, the photomechanical response of the molecular crystal nanostructures arises from nonequilibrium crystal forms and cannot be predicted using only knowledge of the equilibrium reactant and product crystals. Second, it is possible to map the molecular-level motions associated with the photochemical reaction in the crystal onto the photomechanical motions induced by irradiation of a nanostructure composed of that crystal. This work provides insight into how solid-state photochemistry within nanostructured molecular crystals can give rise to novel photomechanical behavior on micron lengthscales. It is likely that similar phenomena will be observed in other photomechanical molecular crystal systems.

REFERENCES

(1) Cohen, M. D. *Angew. Chem. Int. Ed.* **1975**, *14*, 386-393.

(2) McBride, J. M.; Segmuller, B. E.; Hollingsworth, M. D.; Mills, D. E.; Weber, B. A. *Science* **1986**, *234*, 830-835.

(3) MacGillivray, L. R.; Papaefstathiou, G. S.; Friscic, T.; Hamilton, T. D.; Bucar, D. K.; Chu, Q.; Varshney, D. B.; Georgiev, I. G. *Acc. Chem. Res.* **2008**, *41*, 280-291.

(4) Keating, A. E.; Garcia-Garibay, M. A. In *Organic and Inorganic Photochemistry*; Ramamurthy, V., Schanze, K. S., Eds.; Marcel Dekker: New York, 1998.

(5) Kohler, W.; Novak, K.; Enkelmann, V. *J. Chem. Phys.* **1994**, *101*, 10474-10480.

(6) Enkelmann, V. *Mol. Cryst. Liq. Cryst.* **1998**, *313*, 15-23.

(7) Harada, J.; Nakajima, R.; Ogawa, K. *J. Am. Chem. Soc.* **2008**, *130*, 7085-7091.

(8) Garci-Garibay, M. A. *Ang. Chem. Int. Ed.* **2007**, *46*, 2-5.

(9) Finkelmann, H.; Nishikawa, E.; Pereira, G. G.; Warner, M. *Phys. Rev. Lett.* **2001**, *87*, 015501/1-015501/4.

(10) Yu, Y.; Nakano, M.; Ikeda, T. *Nature* **2003**, *425*, 145.

(11) Camacho-Lopez, M.; H. Finkelmann, H.; Shelley, P. P.-M. *Nat. Mater.* **2004**, *3*, 307-310.

(12) Ikeda, T.; Mamiya, J.; Yu, Y. *46* **2007**, 506-528.

(13) White, T. J.; Tabiryan, N. V.; Serak, S. V.; Hrozhyk, U. A.; Tondiglia, V. P.; Koerner, H.; Vaia, R. A.; Bunning, T. J. *Soft. Mater.* **2008**, *4*, 1796-1798.

(14) Oosten, C. L. v.; Bastiaansen, C. W. M.; Broer, D. J. *Nat. Mater.* **2009**, *8*, 677-682.

(15) Lange, C. W.; Foldeaki, M.; Nevodchikov, V. I.; Cherkasov, V. K.; Abakumov, G. A.; Pierpont, C. G. *Journal of the American Chemical Society* **1992**, *114*, 4220-4222.

(16) Flannigan, D. J.; Lobastov, V. A.; Zewail, A. H. *Ang. Chem. Int. Ed.* **2007**, *46*, 9206-9210.

(17) Flannigan, D. J.; Samartzis, P. C.; Yurtsever, A.; Zewail, A. H. *Nano Lett.* **2009**, *9*, 875-881.

(18) Irie, M. *Chem. Rev.* **2000**, *100*, 1685-1716.

(19) Irie, M.; Kobatake, S.; Horichi, M. *Science* **2001**, *291*, 1769-1772.

(20) Kobatake, S.; Takami, S.; Muto, H.; Ishikawa, T.; Irie, M. *Nature* **2007**, *446*, 778-781.

(21) Colombier, I.; Spagnoli, S.; Corval, A.; Baldeck, P. L.; Giraud, M.; Leaustic, A.; Yu, P.; Irie, M. *J. Chem. Phys.* **2007**, *126*, 011101/1-011101/3.

(22) Uchida, K.; Sukata, S.; Matsuzawa, Y.; Akazawa, M.; Jong, J. J. D. d.; Katsonis, N.; Kojima, Y.; Nakamura, S.; Areephong, J.; Meetsma, A.; Feringa, B. L. *Chem. Commun.* **2008**, 326-328.

(23) Koshima, H.; Ojima, N.; Uchimoto, H. *J. Am. Chem. Soc.* **2009**, *131*, 6890-6891.

(24) Naumov, P.; Kowalik, J.; Solntsev, K. M.; Baldridge, A.; Moon, J.-S.; Kranz, C.; Tolbert, L. M. *J. Am. Chem. Soc.* **2010**, *132*, 5845-5857.

(25) Becke, A. D. *Phys. Rev. A* **1988**, *38*, 3098-3100.

(26) Lee, C. T.; Yang, W. T.; Parr, R. G. *Phys. Rev. B* **1988**, *37*, 785-789.

(27) Becke, A. D. *J. Chem. Phys.* **1993**, *98*, 5648-5652.

(28) Frisch, M. J.; Trucks, G. W.; Schlegel, H. B.; Scuseria, G. E.; Robb, M. A.; Cheeseman, J. R.; Montgomery, J. J. A.; Vreven, T.; Kudin, K. N.;

Burant, J. C.; Millam, J. M.; Iyengar, S. S.; Tomasi, J.; Barone, V.; Mennucci, B.; Cossi, M.; Scalmani, G.; Hasegawa, J.; Ishida, M.; Nakajima, T.; Honda, Y.; Kitao, O.; Nakai, H.; Klene, M.; Li, X.; Knox, J. E.; Hratchian, H. P.; Cross, J. B.; Bakken, V.; Adamo, C.; Jaramillo, J.; Gomperts, R.; Stratmann, R. E.; Yazyev, O.; Austin, A. J.; Cammi, R.; Pomelli, C.; Ochterski, J. W.; Ayala, P. Y.; Morokuma, K.; Voth, G. A.; Salvador, P.; Dannenberg, J. J.; zakrzewski, V. G.; Dapprich, S.; Daniels, A. D.; Strain, M. C.; Farkas, O.; Malick, D. K.; Rabuck, A. D.; Raghavachari, K.; Foresman, J. B.; Ortiz, J. V.; Cui, Q.; Baboul, A. G.; Clifford, S.; Cioslowski, J.; Stefanov, B. B.; Liu, G.; Liashenko, A.; Piskorz, P.; Komaromi, I.; Martin, R. L.; Fox, D. J.; Keith, T.; Al-Laham, M. A.; Peng, C. Y.; Nanayakkara, A.; Challacombe, M.; Gill, P. M. W.; Johnson, B.; Chen, W.; Wong, M. W.; Gonzalez, C.; Pople, J. A.; Gaussian Inc.: Wallingford, CT, 2004.

(29) Sweeting, L. M.; Rheingold, A. L.; Gingerich, J. M.; A. W. Rutter; Spence, R. A.; Cox, C. D.; Kim, T. J. *Chem. Mater.* **1997**, *9*, 1103-1115.

(30) Ramamurthy, V.; Venkatesan, K. *Chem. Rev.* **1987**, *87*, 433-481.

(31) Good, J. T.; Burdett, J. J.; Bardeen, C. J. *Small* **2009**, *5*, 2902-2909.

(32) Al-Kaysi, R. O.; Bardeen, C. J. *Chem. Commun.* **2006**, 1224-1226.

(33) Al-Kaysi, R. O.; Dillon, R. J.; Zhu, L.; Bardeen, C. J. *J. Colloid. Interfac. Sci.* **2008**, *327*, 102-107.

(34) Al-Kaysi, R. O.; Muller, A. M.; Bardeen, C. J. *J. Am. Chem. Soc.* **2006**, *128*, 15938-15939.

(35) Enkelmann, V.; Wegner, G.; Novak, K.; Wagener, K. B. *J. Am. Chem. Soc.* **1993**, *115*, 10390-10391.

(36) Novak, K.; Enkelmann, V.; Wegner, G.; Wagener, K. B. *Ang. Chem. Int. Ed.* **1993**, *32*, 1614-1616.

(37) Fernandes, M. A.; Levendis, D. C. *Acta Cryst. B* **2004**, *60*, 315-324.

(38) Davaasambuu, J.; Busse, G.; Techert, S. *J. Phys. Chem. A* **2006**, *110*, 3261-3265.

(39) Khan, M.; Brunklaus, G.; Enkelmann, V.; Spiess, H.-W. *J. Am. Chem. Soc.* **2008**, *130*, 1741-1748.

(40) Honda, K.; Nakanishi, F.; Feeder, N. *J. Am. Chem. Soc.* **1999**, *121*, 8246-8250.

(41) Natarajan, A.; Tsai, C. K.; Khan, S. I.; McCarren, P.; Houk, K. N.; Garcia-Garibay, M. A. *J. Am. Chem. Soc.* **2007**, *129*, 9846-9847.

(42) Turowska-Tyrk, I.; Trzop, E. *Acta Crystal. B* **2003**, *59*, 779-786.

(43) Turowska-Tyrk, I. *J. Phys. Org. Chem.* **2004**, *17*, 837-847.

(44) Harris, K. D. M.; Thomas, J. M. *J. Solid. State. Chem.* **1991**, *93*, 197-205.

(45) Bertmer, M.; Nieuwendaal, R. C.; Barnes, A. B.; Hayes, S. E. *J. Phys. Chem. B* **2006**, *110*, 6270-6273.

(46) Fonseca, I.; Hayes, S. E.; Bertmer, M. *Phys. Chem. Chem. Phys.* **2009**, *11*, 10211-10218.

(47) Nieuwendaal, R. C.; Bertmer, M.; Hayes, S. E. *J. Phys. Chem. B* **2008**, *112*, 12920-12926.

(48) Takegoshi, K.; Nakamura, S.; Terao, T. *Solid State Nucl. Magn. Reson.* **1998**, *11*, 189-196.

(49) Fonseca, I.; Hayes, S. E.; Blumich, B.; Bertmer, M. *Phys. Chem. Chem. Phys.* **2008**, *10*, 5898-5907.

(50) Peachey, N. M.; Eckhardt, C. J. *J. Phys. Chem.* **1993**, *97*, 10849-10856.

(51) Abdelmoty, I.; Buchholz, V.; Di, L.; Guo, C.; Kowitz, K.; Englemann, V.; Wegner, G.; Foxman, B. M. *Cryst. Growth Design* **2005**, *5*, 2210-2217.

(52) Kuroki, L.; Takami, S.; Yoza, K.; Morimoto, M.; Irie, M. *Photochem. Photobiol. Sci.* **2010**, *9*, 221-225.

(53) Vold, R. L.; Waugh, J. S.; Klein, M. P.; Phelps, D. E. *Journal of Chemical Physics* **1968**, *48*, 3831-&.

CHAPTER IV

ANALYTICAL APPLICATIONS OF NUCLEAR MAGNETIC RESONANCE SPECTROSCOPY

4.1 Introduction

Nuclear Magnetic Resonance has become an essential technique for the characterization of organic and inorganic compounds. The use of solid-state NMR as a structure determination tool has become routine in cases where samples cannot be crystallized and studied by X-ray techniques. NMR active heteroatoms, such as ^{13}C, ^{31}P, ^{7}Li, ^{29}Si and ^{27}Al have been widely used over the past decade or so to probe deeper into the structure and properties of molecules. Solution-state NMR has become an indispensable technique in the field of analytical and organic chemistry. Since its start, by Schaefer and Stejskal in 1976[1], a combined use of magic-angle spinning (MAS), proton-to-carbon (or other non-sensitive nuclei) cross polarization, and high-power proton decoupling has been the key in solving complex NMR problems in solid state. In NMR, the line position in a spectrum gives information about the chemical environment of an atomic nucleus, which allows a fingerprint of the chemical groups present in a sample. Through-bond scalar couplings and through-space dipolar couplings between spins

provide information about the structure and stereochemistry of molecules. Two-dimensional NOE correlation spectroscopy (NOESY) and the Nuclear Overhauser Effect (NOE) difference experiment can be used to study the interaction of spins in space, which can be used to study associations between various components of complex mixtures, such as printing inks and media formulations in solution. Empirical evidences can be well supported by the use if *ab initio* calculations. Gaussain calculations can give information about the stable geometries and also predict the NMR spectra of the molecules under study. This chapter summarizes the use of NMR in solid and solution chemistry, on diverse samples, to solve analytically challenging problems.

4.2 pH- responsive nanogated ensemble based on gold-capped mesoporous silica through an acid-labile Acetal linker

4.2.1 Motivation

Mesoporous Silica (MS) in their early form were first synthesized by Yanagisawa et al.[2] in the 1990s and it quickly became a popular field of research. Kresge et al[3], were responsible for the synthesis of mesoporous molecular sieves (MMS) in1992, and ever since there has been a constant effort to synthesize new and useful mesoporous materials These porous materials have typical pore diameters of 2nm to 50 nm. Mesoporous materials comprise of inorganic xerogels, pillared clays, and the mobil composition of matter (MCM)[4]. Mesoporous silica have high surface area, uniform pore size, tunable

pore structure, and diverse surface functionality. These properties make them highly desirable for solid support to construct hybrid materials, for catalysis, enzyme mobilization, drug delivery and imaging[4-12]. Mesoporous silica materials have also been used as a controlled release system, which respond to distinct external stimuli. A series of supramolecular nanovalves using redox[13], pH[14], competitive binding[15], light[16], and enzymes[17] as actuators have been demonstrated. Nanoparticles have also been widely used as capping agents in MS release system. Recently, gold nanoparticles were used as blocking caps to control the transport of cargo from meosporous silica by controlling the pH[18].

Acid sensitive drug delivery vehicles are highly desired in the treatment of acidic targets, such as tumors and inflammatory tissues. Several acid degradable linkers have been used in the construction of prodrug conjugate, lipid, polymeric micelles and nanogels to deliver therapeutic contents in acidic pH environments.

4.2.2 Mechanism and characterization using NMR

In this section of the chapter we discuss the properties and characterization of a new pH-responsive nanogated ensemble. Gold nanoparticles were capped onto the mesoporous silica through an acid-labile acetal linker to make these pH-responsive nanogates[19].

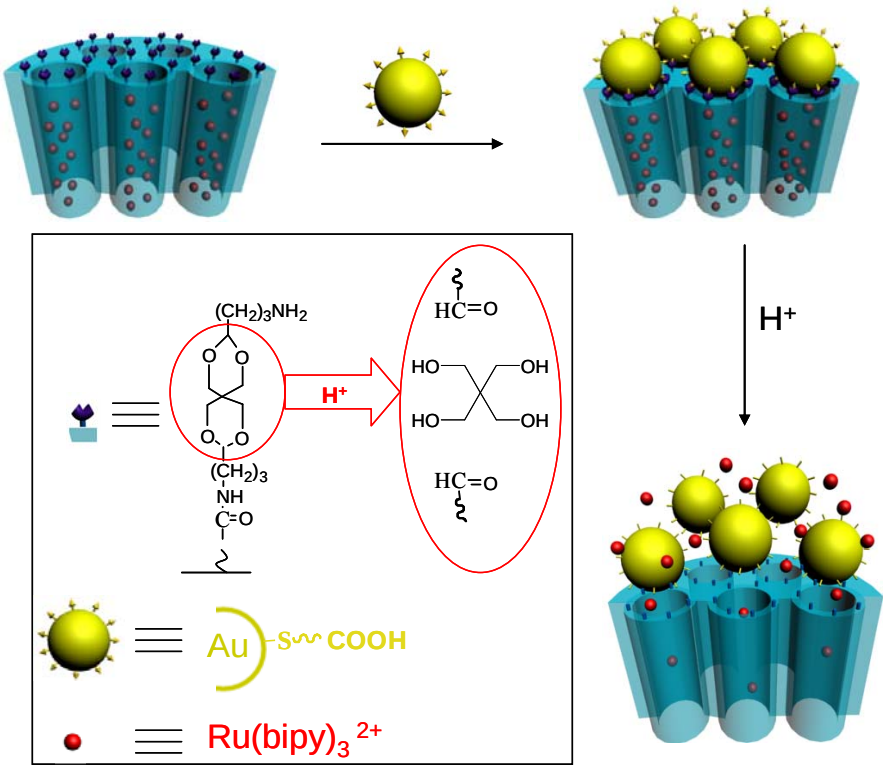

Figure 4.1 Scheme of pH-responsive nanogate ensemble ***(Published with permission from ref 19. Copyright 2010 American Chemical Society)***

As shown in Figure 4.1, at neutral pH, the linker remains intact and pores are blocked with gold nanoparticles hindering molecular diffusion from the pores. When the pH is lowered, to make the solution acidic, the acetal group (circled red in Figure 4.1) hydrolyses and the protective gold cap dislodges, allowing the escape of molecules from the MS chamber. This phenomenon can be controlled by regulating the pH. The nanogated assembly was made using the following synthesis scheme (Figure 4.2)

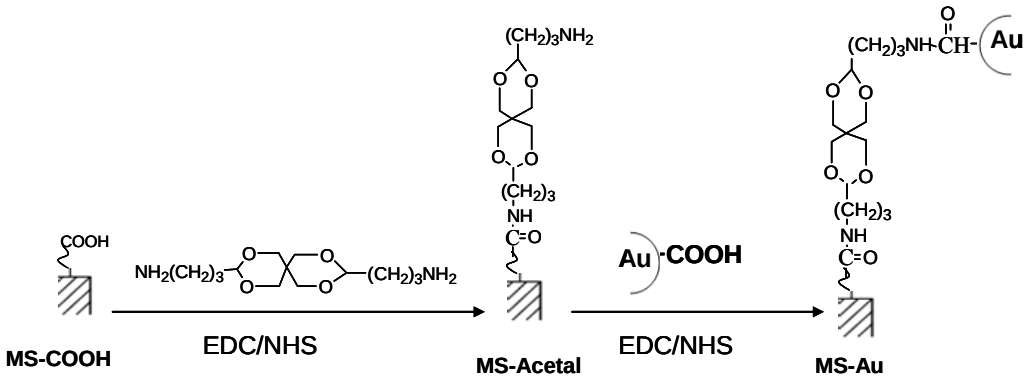

Figure 4.2 Schematic outline of synthesis of MS-Aetal and MS-Au ***(Published with permission from ref 19. Copyright 2010 American Chemical Society)***

One of the most essential requirements, for these nanogated ensembles to respond to change in pH is the presence of the gold cap, which creates a structural difference between MS-Acetal and MS-Au. In order to verify the formation of the gold-capped MS, several spectroscopic methods were used, including TEM, XRD, and ssNMR. BET nitrogen sorption isotherm and BJH pore size distribution techniques were used to establish the hexagonal channel shape of the MS.

13C solid-state NMR spectra of MS-Acetal and MS-Au were acquired at 9.4 T on a Bruker DSX spectrometer (^{1}H frequency 400.1 MHz) equipped with a double resonance 2.5 mm magic-angle-spinning probe spinning at 15 kHz. Cross-polarization from ^{1}H to ^{13}C was incorporated using a 4 ms 40 kHz spin lock on ^{13}C and a linearly ramped (50%-100%) matching field on ^{1}H. 1024 complex time points with a dwell of 20 μs (spectral width 50 kHz, total acquisition time 20.48 ms) were acquired with a recycle delay of 3 s and a total acquisition time of 24 hours.

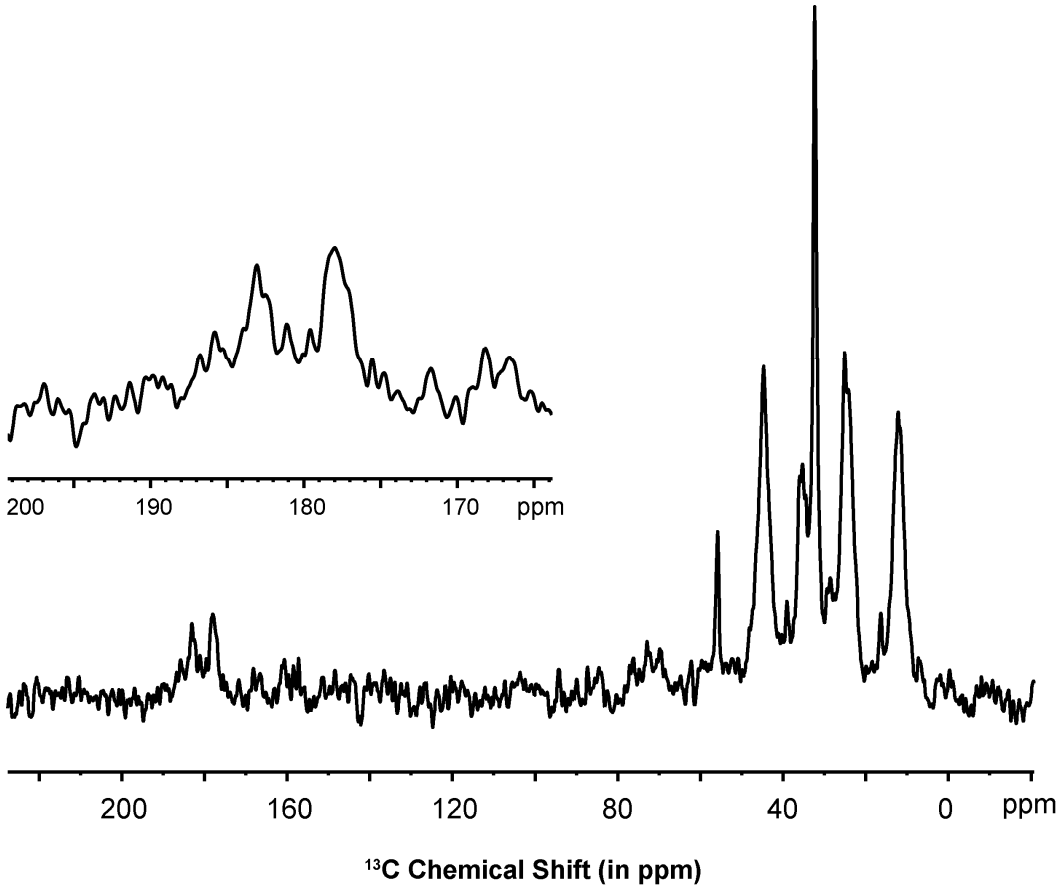

Figure 4.3 Solid state ^{13}C CP-MAS NMR spectrum of MS-Aetal

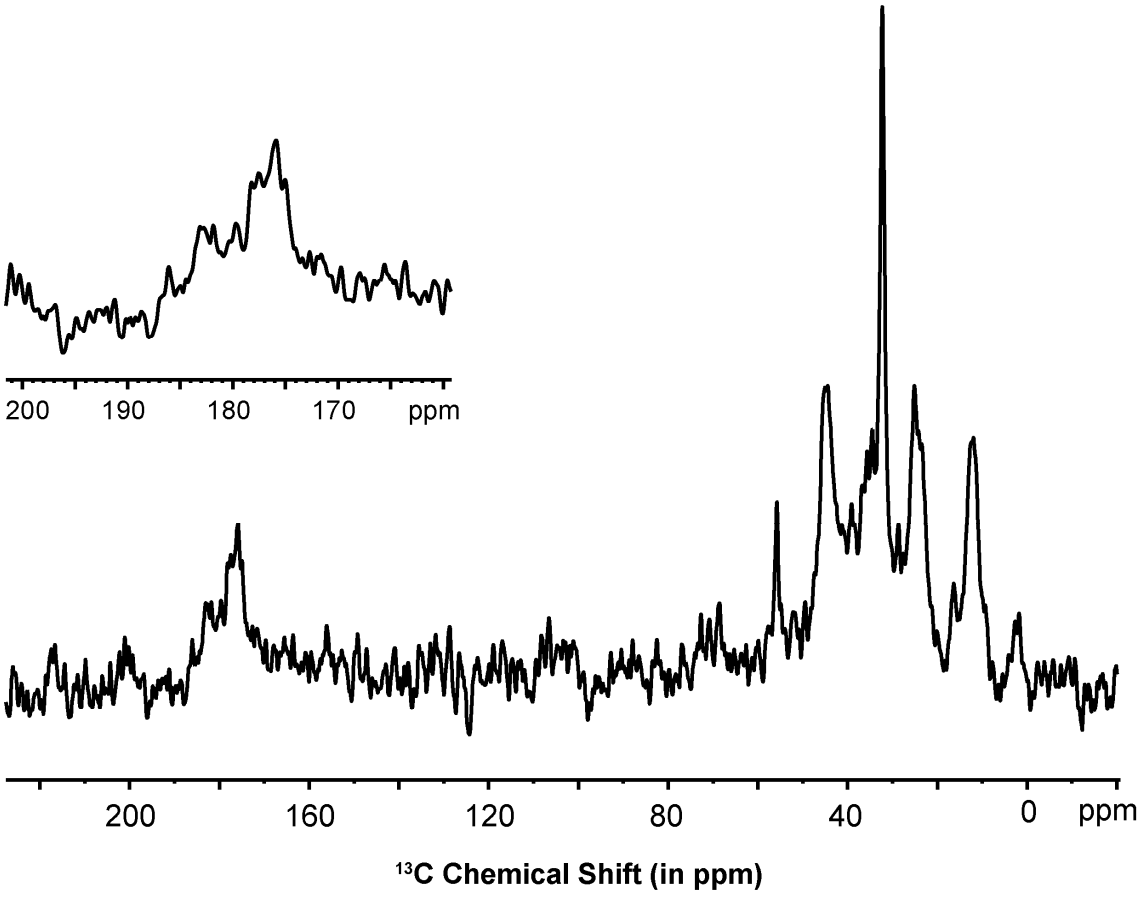

Figure 4.4 Solid state ^{13}C CP-MAS NMR spectrum of MS-Au

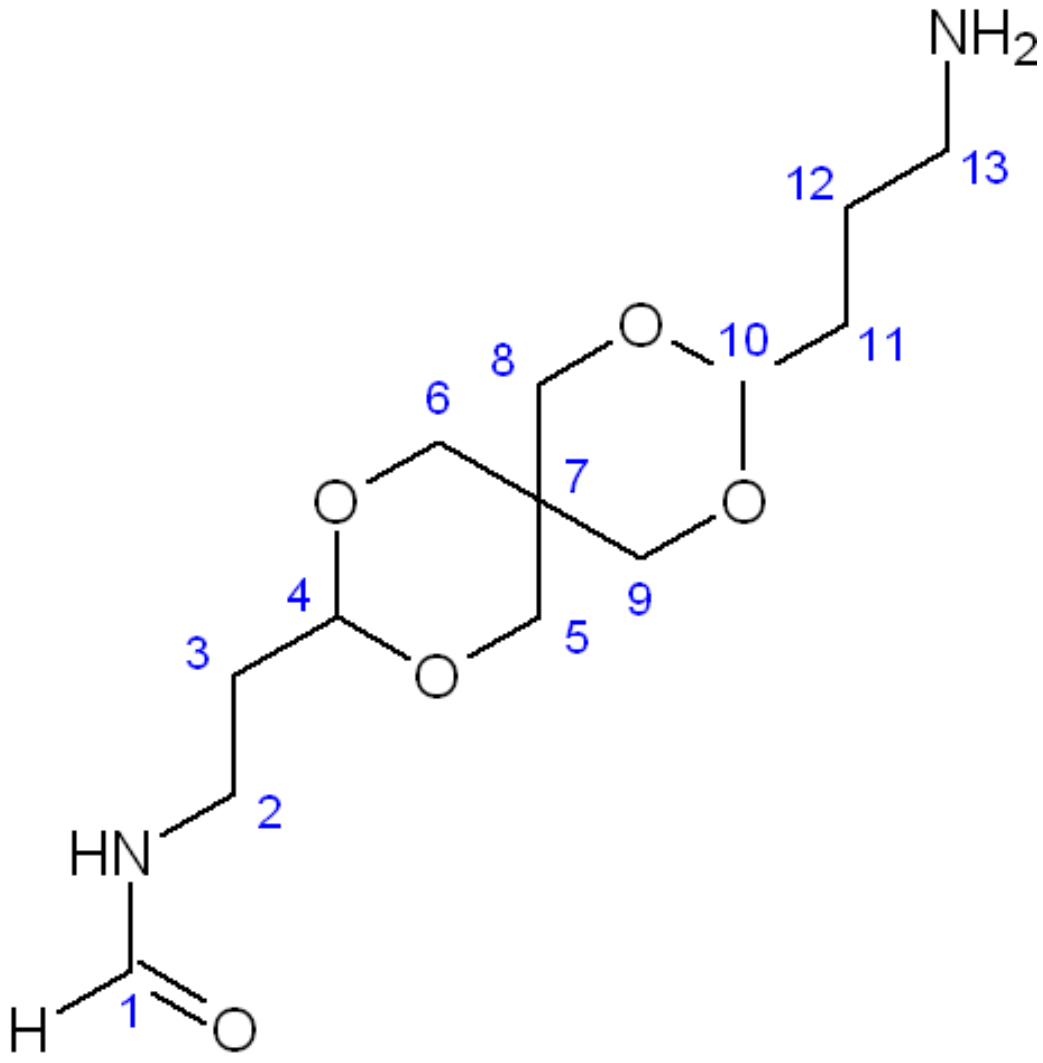

Figure 4.5 MS-Acetal basic structure with carbon numbers for assignment

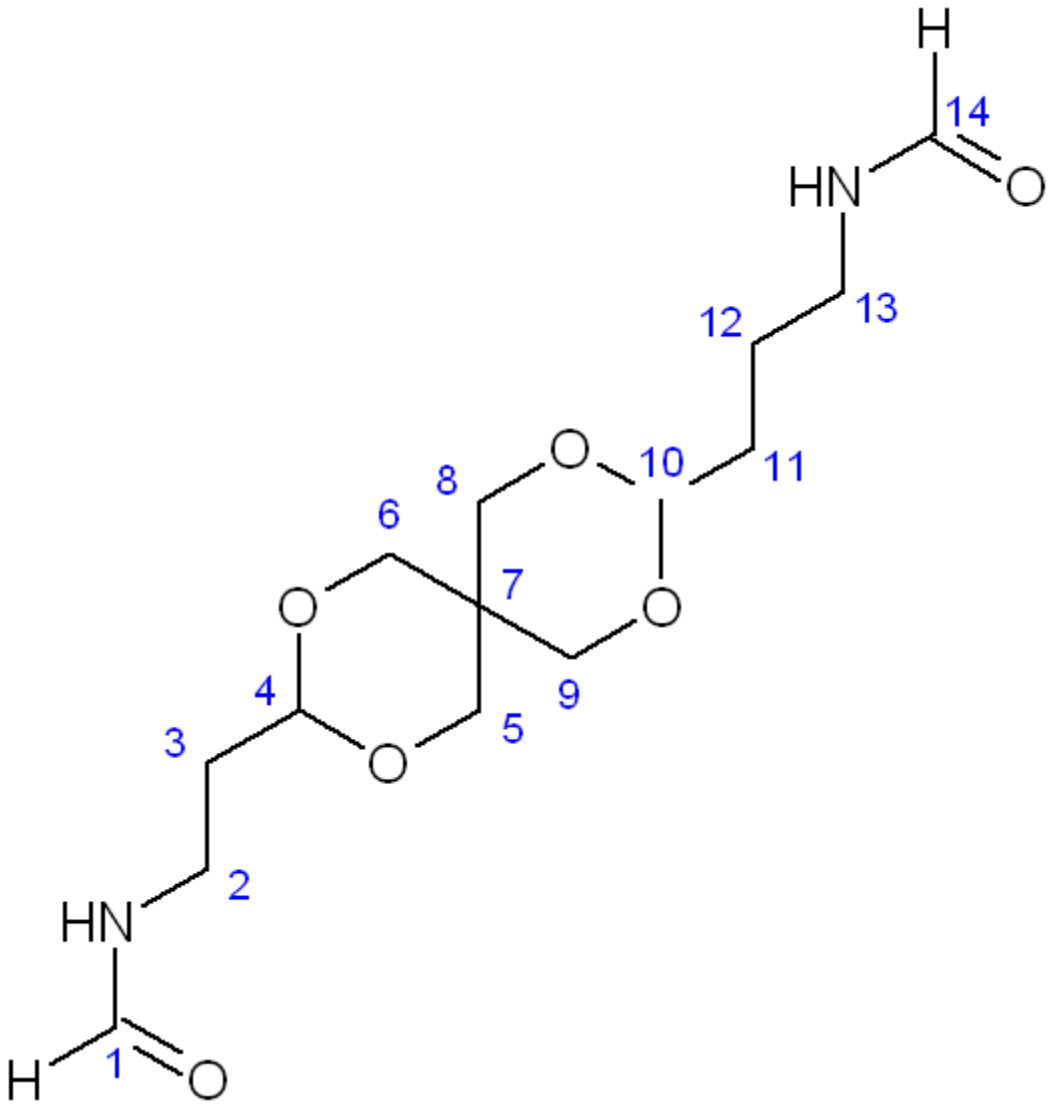

Figure 4.6 MS-Au basic structure with carbon numbers for assignment

The ssNMR spectra of MS-Acetal and MS-Au have subtle differences, which indicate that they have different chemical environment and functional groups. ssNMR spectra can be used to compare and conclude[20] that the gold nanoparticle is indeed attached to the C=O group, which in turn is attached to the NH- part of the acetal chain. Chemical shifts can be assigned to the thirteen carbon atoms present in the case of MS-Acetal (Figure 4.5) and fourteen carbon atoms (Figure 4.6) present in the case of MS-Au sample. Carbon number 12, 2, 11, 3, 7, and 13 appear between 0-45 ppm, as shown in Figure 4.3. Carbons 5, 6, 8 and 9, being equivalent, appear as a single resonance at 55 ppm. The carboxylic group carbon is shifted downfield and appears at ~170 ppm. Since carbon 4 and 10 have only one proton, its challenging to obtain a reasonable CP with our optimization conditions. As a result we do not see any line from these two carbons. Obviously, the ssNMR spectrum of MS-Au is similar to that of MS-Acetal, since it has very similar structure. A closer comparison shows that the peak at 175 ppm has grown in intensity. This suggests formation of a new carboxylic group in the molecule. This establishes that the MS-Au has the gold cap, which is formed by the loss of a water molecule.

4.2.3 Section Conclusion

ssNMR can be useful to distinguish subtle structural changes in mesoporous silica materials, which are otherwise challenging to characterize. Since ssNMR is a non-invasive technique, measurements can be made on important materials, without altering their structural or functional properties. Acid labile acetal group linked gold nanoparticles can be used as pH-dependent capping agents for the mesoporous silica molecules. The

guest molecules were blocked from the MS-Au at neutral pH and released at low pH. These materials can find potential use in the delivery of therapeutic agents to low pH tissues, such as tumors and inflammatory sites and other pH dependent applications.

4.3 Protein refolding assisted by Periodic Mesoporous Organosilicas

4.3.1 Motivation

Since its discovery in 1992,[3] ordered mesoporous structures (OMSs) have been known to exhibit unique structural features, such as regular pore geometry, high surface area, and large pore volume[21]. The surface properties of OMS can be altered easily[22] to transform them into highly useful materials. Periodic mesoporous organosilicas (PMOs) are one such class of hybrid materials, which are formed by assembly from organic group bridged silsesquioxanes, $(RO)_3Si\text{-}R\text{-}Si(OR)_3$[23-25]. PMOs have homogenously distributed organic groups within their framework walls. These features make PMOs highly useful in medical and biological fields, such as protein immobilization [26], bioactive glasses[27], and drug release[28].

One of the current research interests in the bioenginnering industry is exploring large-scale, efficient and rapid refolding of recombinant proteins from inclusion bodies, which are formed by overexpression of cloned or synthetic genes of *Escherichai coli*[29]. Although, over the past 10 years or so, many methods have been developed to carry on this process efficiently[30-32], formation of inactive protein aggregates, which competes with true folding, still remains the main roadblock in efficient protein recovery[33,34]. Batch dilution, the most prominent and popular technique used today suffers from the need of

extremely low protein concentrations (<0.1 mg/mL). Pulse-renaturation[35] or fed-batch operation[36] has been devised to increase the concentration of renatured proteins. They require stepwise or continuous addition of unfolded proteins to the refolding solution, in presence of the denaturant. However, this changes the optimal refolding conditions and destabilizes refolded proteins at high denaturant concentrations.

4.3.2 Experimental Section

A new method of protein refolding without perturbing the optimal refolding conditions can be achieved by the use of ordered mesoporous materials [37]. The unique structural and surface properties of PMOs can be used to effectively entrap denatured proteins. The entrapped proteins can be released into the refolding buffer in a controlled fashion by a stimuli response. The mesoporous channels are uniform in size distribution, and they can be tailored to uniquely fit the individual denatured proteins. This process minimizes the risk of protein aggregation. Cumulative folding can be achieved due to the continuous release of denatured proteins (Figure 4.5).

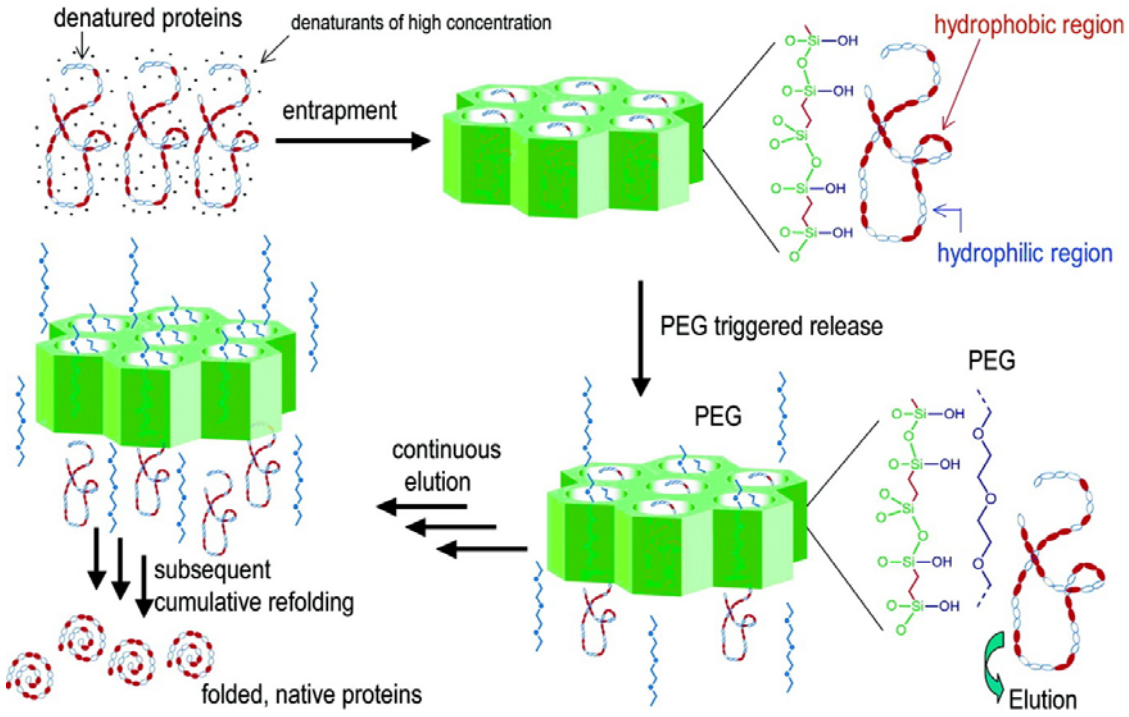

Figure 4.7 Protein refolding assisted by PMO ***(Published with permission from ref 37. Copyright 2007 American Chemical Society)***

Ethylene bridged periodic mesoporous organosilicas with two different pore size were prepared under acidic conditions using BTESE as the organosilicas precursor and Brij 76 and Brij 56[38,39] as the template by our collaborator, Prof. Pingyun Feng's group at UC Riverside. The obtained periodic mesoporous organosilicas were denoted as E-PMO-A (Brij 76) and E-PMO-B (Brij 56). For comparisons, pure siliceous SBA-15 was also prepared.

Table 4.1 Structural properties of PMOs and their adsorption capacities for d-Lys

Materials	**Template**	**Pore size (nm)**	**BET surface area (m^2/g)**	**Pore volume (cm^3/g)**	**Maximum adsorption capacity (mg/g)**
E-PMO-A	Brij 76	4.8	891	0.83	168
E-PMO-B	Brij 56	4.1	1025	0.80	138
SBA-15	Brij 76	5.3	990	0.96	280

The XRD patterns of E-PMO-A and SAB-15 show the characteristics of an ordered two dimensional hexagonal mesoporous structure (Figure 4.8)

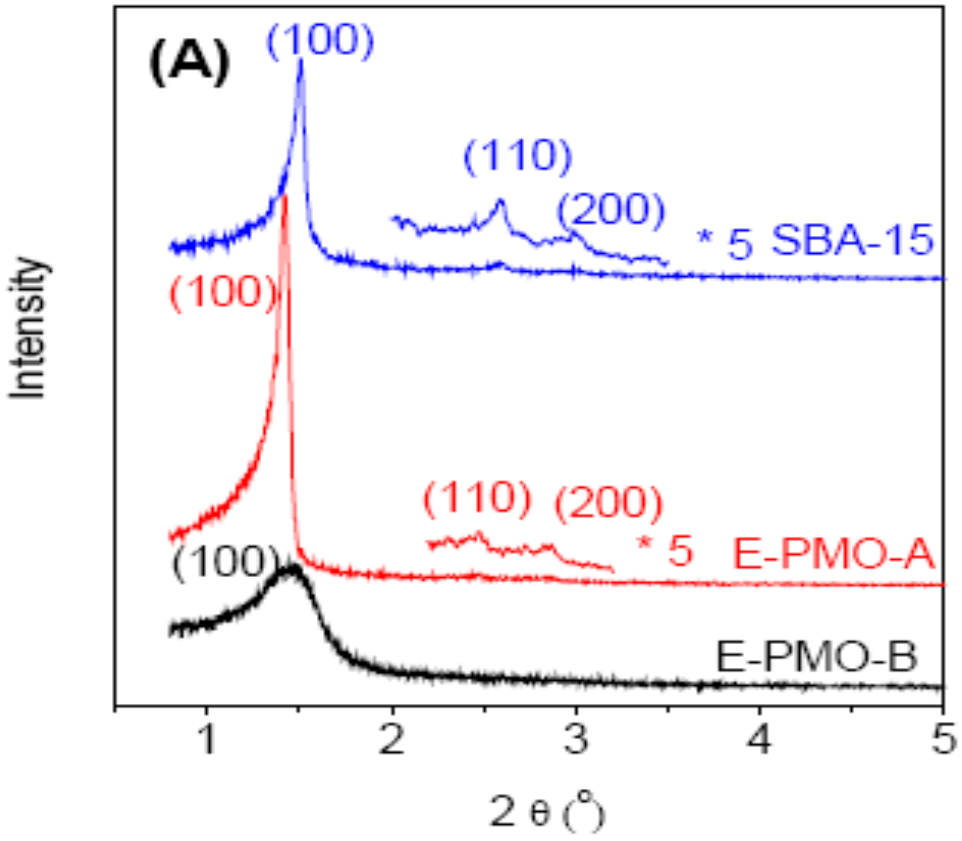

Figure 4.8 XRD patterns of E-PMO-A (red), E-PMO-B (black) and SBA-15 (blue)
(Published with permission from ref 37.Copyright 2007 American Chemical Society)

4.3.3 Characterization of PMOs using NMR

In order for the protein folding to work, a simultaneous existence of hydrophilic and hydrophobic surface in the silica framework is required. Therefore it was essential to verify if E-PMO exhibits both hydrophobic and hydrophilic feature in the form of ethylene and silanol groups. NMR is a sensitive and non-invasive technique for nuclei with non-zero spins, like ^{13}C and ^{29}Si. ^{29}Si is a spin ½ nuclei with a natural abundance of 4.7%. Its relative sensitivity is 7.84 x 10^{-3} compared to ^{1}H, which is 1. ^{29}Si studies around the world, in various different ssNMR research groups over the years have provided highly insightful knowledge about the structure and chemistry of silicon containing materials[40]. Pioneering work in the field of zeolites using 29Si NMR shifts was achieved by Lippmaa et al between 1978 and 1980[41,42]. Typical ^{29}Si lines are over 100 ppm wide. In order to differentiate resonances arising from different ^{29}Si environments, cross polarization magic angle spinning experiments should be used. Due to the small chemical shift anisotropy of ^{29}Si nucleus, minimal spinning sideband problems are seen in MAS studies of silicates[43]. This is not true with ^{13}C nuclei, especially at higher spinning speed and larger field strengths.

Magic-angle-spinning (MAS) solid-state NMR spectra of E-PMO-A were acquired on a Bruker DSX 400 Spectrometer (400.42 MHz ^{1}H; 100.70 MHz ^{13}C; 79.55 MHz ^{29}Si) using a double resonance 4 mm MAS probe (sample volume ~ 80 mL). The MAS rate for both ^{13}C and ^{29}Si samples were 8 kHz. ^{13}C spectra were acquired using tangent ramped cross-polarization from ^{1}H followed by high power proton decoupling (83 kHz TPPM). 2048 complex time points were sampled with a spectral width of 50 kHz

and averaged over 2048 scans with a relaxation delay of 5 s. ^{29}Si spectra were acquired using a 90-degree Si pulse (50 kHz) followed by high power proton decoupling (83 kHz TPPM). 2048 complex time points were sampled with a spectral width of 50 kHz and averaged over 16384 scans with a relaxation delay of 4 s. The spin-lattice relaxation times of ^{29}Si in solids are very small in comparison with ^{13}C nuclei, which allow the use of relatively short pulse delay time in the experiments. Figure 4.9 shows the obtained spectra. The ^{13}C spectrum shows a sharp single peak at 8 ppm which corresponds to the Si-C-C-Si backbone structure of the E-PMO material. There is another small peak at 60 ppm which corresponds to the carbons from ethylene glycol molecules, used for elution of the proteins. This result suggests that the ethylene glycol (and not the D-lys) is associated with the periodic mesoporous material. The ^{29}Si NMR results, shown in Figure 4.9 B clearly establish that there are three different types of Si center in the PMO. T_1, is the Silicon center with one –OSi group attached to it, and can be seen at about -50 ppm, T_2, is the Silicon center with two –OSi groups attached to it, and appears at -60 ppm, and T_3, is the Silicon center with three –OSi groups attached to it, and can be seen at about -70 ppm. These results indicate the successful removal of the template and the hybrid structure that the E-PMO-A forms with poly(ethylene glycol).

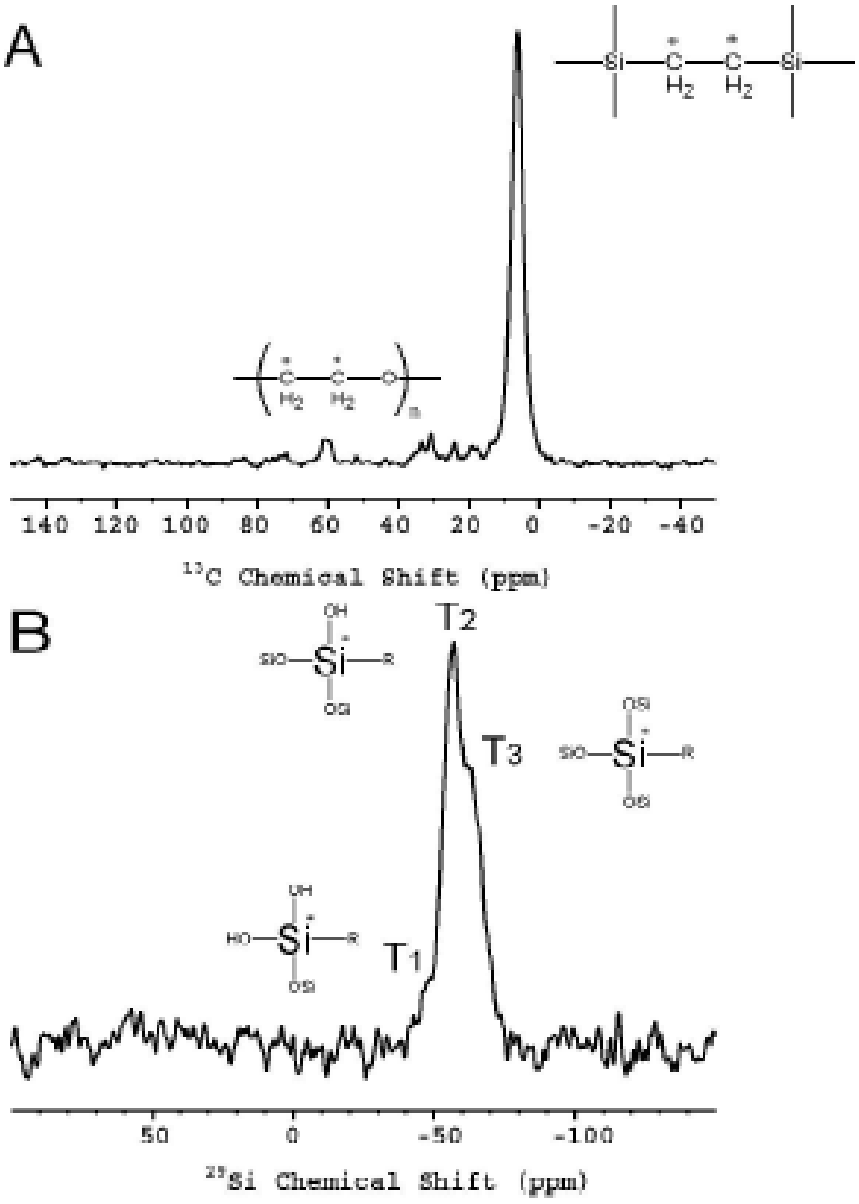

Figure 4.9 ^{13}C CP/MAS (A) and ^{29}Si MAS (B) spectra of E-PMO-A. The signals were assigned to specific C/Si atoms with different environments, as marked with asterisks. The results indicate the successful removal of the template and a hybrid structure of E-PMO-A.

Hen egg white lysozyme (D-lys) was used a model protein to study the efficiency of PMO-assisted refolding. At basic pH the lysozyme is positively charged but the silica surface is negatively charged. Interactions between mesoporous silicas and lysozyme include electrostatic interactions between charged silanol groups on the silica surface and the exposed charge of amino acid reside of lysozyme and hydrophobic interactions between ethylene groups of E-PMO and exposed hydrophobic parts of protein. Poly (ethylene glycol) was used as a trigger to release encapsulated protein from the mesopores because it can form stronger hydrogen bonds with the silanol groups of the silica surface than the D-lys. There are several advantages of this method, like reusability of the matrix, easy separation of protein from denaturants, and a controlled folding protocol.

4.3.4 Section Conclusion

Use of ssNMR was essential to understand the structure of E-PMOs, which seems to be a promising material to enhance lysozyme oxidative refolding by active entrapment of denatured proteins in PMO and by subsequent PEG-triggered release into the refolding buffer. The rich synthetic chemistry of ordered mesoporous materials, together with various pore geometries and sizes and controllable surface functionalities, as established by the use of magic angle ssNMR measurements on ^{13}C and ^{29}Si nuclei, makes it possible to develop suitable materials for the adsorption and controlled release of proteins.

4.4 Binder-Dispersant Interactions in Ink-jet printing media

4.4.1 Background and Analysis Goal

We tested for a chemical interaction between the dispersant (DIC RW-0058 styrene-acrylic random co-polymer) and binder (DIC RW-4601 anionic polyurethane) in solution. We gathered evidence identifying the groups on the polymers responsible for the interaction. The structures of these molecules are shows in Figure 4.12 and Figure 4.13.

4.4.2 NMR investigation

In ^{1}H nuclear magnetic resonance (NMR), the line position reflects the immediate chemical environment of an atomic nucleus, allowing a fingerprint of the chemical groups present in a molecule or mixtures of molecules. Through-space dipolar couplings between spins provide a mechanism for the intra- and intermolecular transfer of magnetization between sites that are close in space. Because of this, the dipolar coupling provides a mechanism to assess the interaction between molecules in a mixture. If the molecules do not interact, there will be no dipolar coupling between them in solution. On the other hand, if the molecules bind, either specifically or non-specifically, protons on the different molecules will establish dipolar contact. The Nuclear Overhauser Effect (NOE) difference experiment is a standard method for measuring dipolar interactions in solution-state NMR. In this experiment, one line in the NMR spectrum of a molecule is saturated, which causes a change in intensity of other lines in the spectrum that are dipolar coupled to the corresponding proton.

Figure 4.10 illustrates the NOE difference experiment separately for binder and dispersant solutions, along with their mixture. The dispersant alone shows two broad peaks in the aromatic (7 ppm) and aliphatic regions (1-2 ppm) ranges (Figure 4.10.A). When the aromatic peaks are saturated (indicated by the arrow), there is a corresponding decrease in the aliphatic region, indicating through space proximity. Similarly, when the downfield binder group is irradiated, there is a decrease in intensity at the aliphatic binder sites (Figure 4.10.B). Note, however, the control experiment (Figure 4.10.D) in which the binder solution is saturated at the frequency of the dispersant aromatic protons. In this case, no decrease in intensity is observed. Finally, for the mixture of dispersant and binder (Figure 4.10.C), a clear decrease in signal intensity for the binder occurs upon irradiation of the dispersant peaks, indicating that the two components are interacting (i.e., in close spatial contact) in solution.

A second experiment, 2D NOE correlation spectroscopy (NOESY) provides another way to observe dipolar coupled spins using magnetic resonance. In this case, the dipolar coupling affects magnetization transfer that results in cross-peaks in a 2D correlation experiment. Figure 4.11 shows the 2D NOESY spectrum of the mixture of dispersant and binder in D_2O solution. The large peak in the center is water. The cross-peaks between the binder and dispersant peaks are easily identified, once again indicating an association of binder with dispersant in solution.

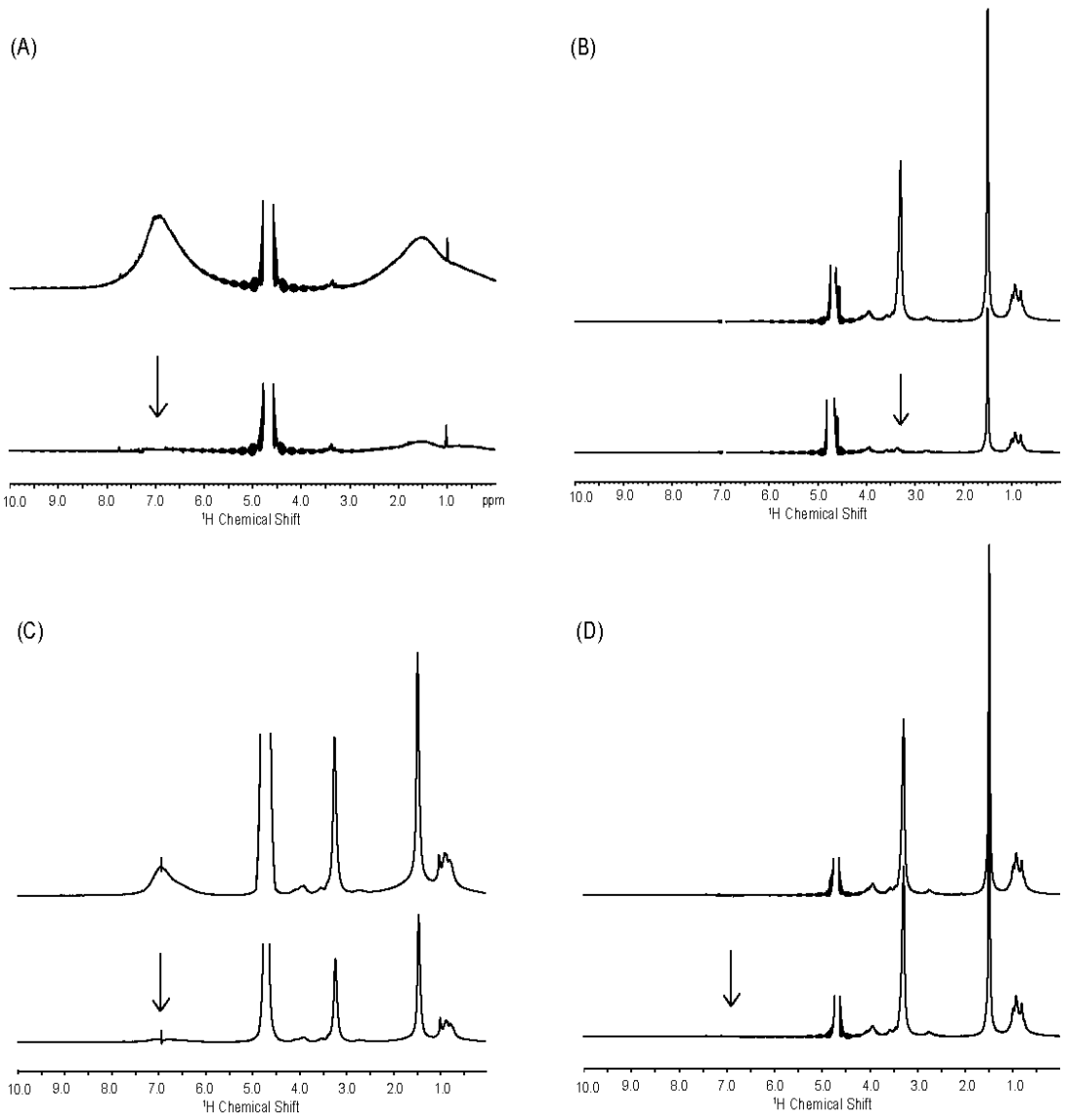

Figure 4.10 ^{1}H NOE difference NMR spectra for (A) solution of dispersant in D_2O, (B) solution of binder in D_2O, (C) mixture of dispersant and binder in D_2O, and (D) solution of binder with control irradiation. The arrows indicate the frequency of the on-resonance saturation pulse in (A), (B), and (C), while (D) shows binder with control saturation at the frequency of the dispersant aromatic peaks. Data were acquired on a 14.1 T (600 MHz, ^{1}H) Bruker AVANCE II spectrometer with a recycle delay of 5 s

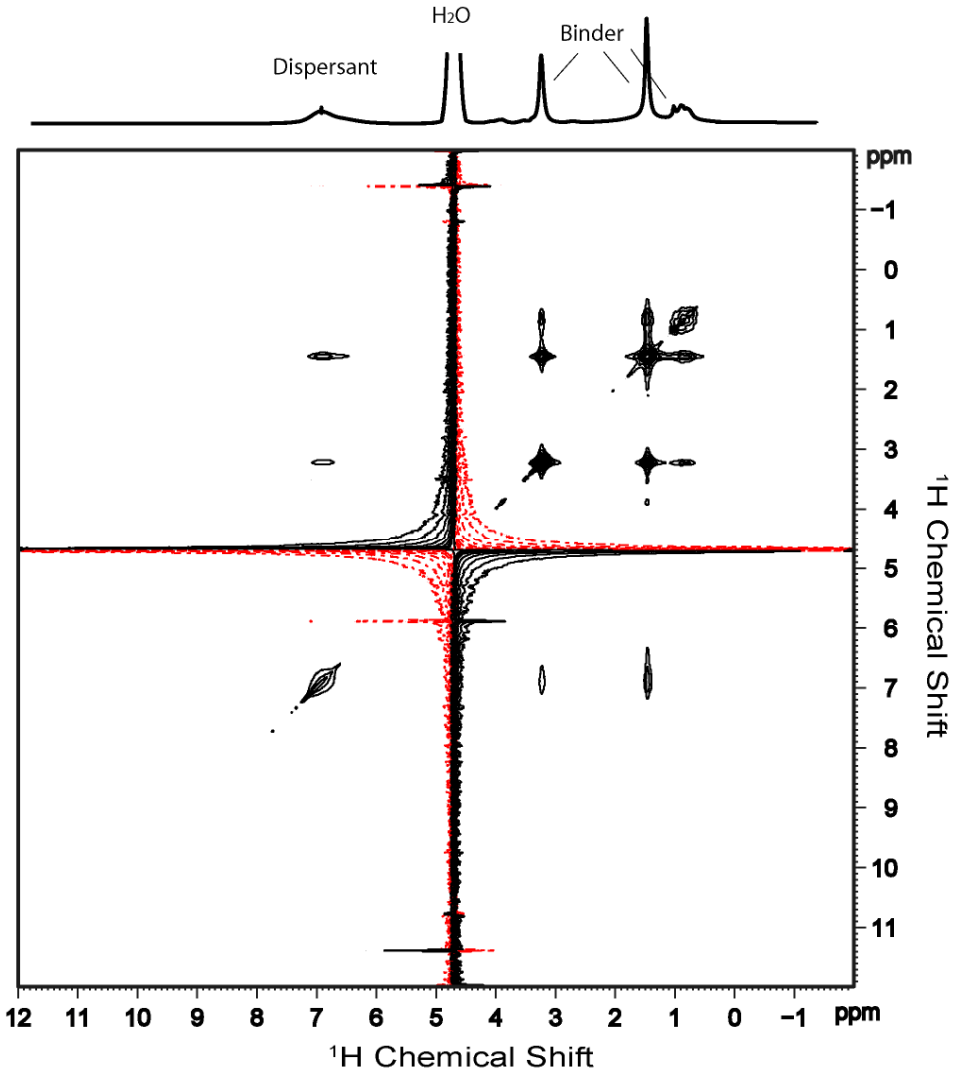

Figure 4.11 ^{1}H NOESY 2D correlations spectrum of the mixture of dispersant and binder in D_2O. Spectrum acquired on a 14.1 T (600 MHz, ^{1}H) Bruker AVANCE II spectrometer using a NOESY mixing time of 100 ms and a recycle delay of 3 s

The NMR shifts for the dispersant were modeled using ChemDraw to compare with the obtained results. The dispersant is a styrene acrylic copolymer composed of styrene, acrylic acid, methacrylic acid, and butyl acrylate. Typically the acrylics are present at a few mole percent. The structure in Figure 4.12 estimates RW0058 as 70% styrene, 10% acrylic acid, 10% methacrylic acid, and 10% butyl acrylate. The ten monomer structure in Figure 4.12 has a molecular weight about 1/10 of the actual structure so resolution will be higher in the computed spectrum. The chain terminations are assumed cumene. The computed spectrum in Figure 4.12 suggests that we should see two peaks for the polymer: one in the aromatic region and the other in the methyl region of the spectrum. This is seen in the measured spectrum in Figure 4.10. The very low resolution displayed in Figure 4.10 is likely due to hindered chain mobility in an aqueous environment.

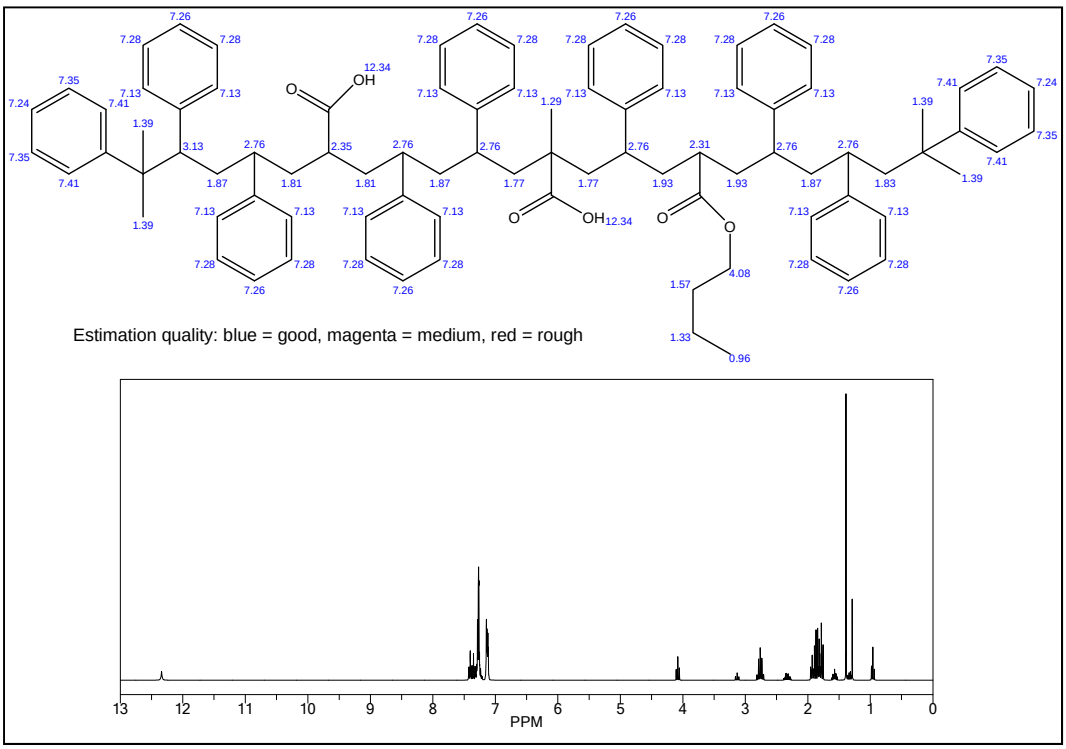

Figure 4.12 RW0058 Dispersant Structure and Predicted proton NMR

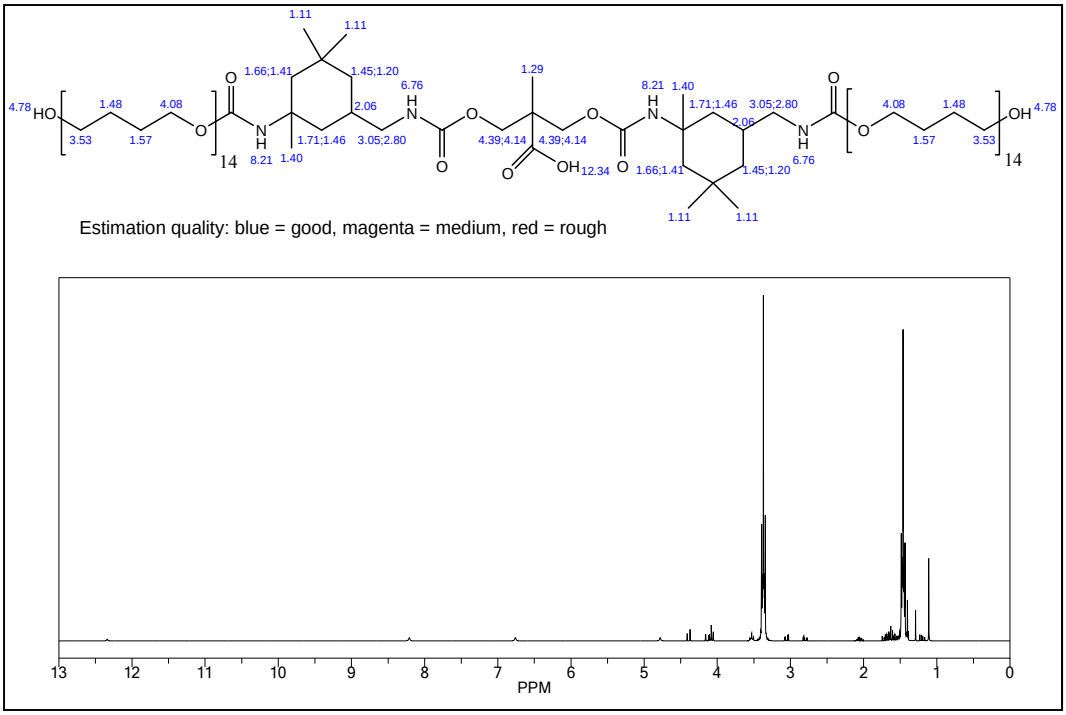

Figure 4.13 RW4601 Binder Structure and Predicted proton NMR

A similar computation was done for the polyurethane binder. This prediction is shown in Figure 4.13. The binder is composed of 3-hydroxy-2-hydroxymethyl-2-methyl-proprionic acid (DMPA), isophorone di-isocyanate (IPDI), and poly(tetramethylene oxide) glycol (PTMG). The polyether side chains are long and dominate the spectrum. Only two units were needed to produce the simulation below. This simulation suggests the two sharp binder peaks in Figure 4.10.B are from the polyether protons. These peaks are shown in proximity to (< 0.5 nm) the phenyl groups in the Figure 4.11 NOESY spectrum[44].

4.4.3 Section Summary

Our results suggest an interaction between the phenyl rings of the styrene acrylic dispersant and the polyether chains of the urethane binder.

4.5 Determining the Latex Particle to Soluble Organic Ratios in Mojito Cyan AR1 and AR2 Latexes

4.5.1 Background and Analysis Goal

The Mojito project is having issues with the scale up of the cyan ink. The first alignment run printed reliably with no kogation or decel issues. The second and many subsequent runs printed poorly. The root cause is not known. However, the issue seems to correlate with free polymer in the latex.

4.5.2 Results and Discussion

In ^{1}H nuclear magnetic resonance (NMR), the line position reflects the chemical environment while the line width is influenced by molecular tumbling rates. Small organic molecules that tumble quickly in solution have line widths of several Hz, while large latex particles (which are tumbling quite slowly and are essentially organic "solids") have line widths on the order of 30 kHz. Figure 4.14 A, B shows how this can be used to easily identify spectral intensity due to these components, with the broad component in 4.12 B corresponding to the latex particles and the narrow lines (expanded in 4.12 A) being due to the small organics.

The extreme difference in line widths provides a mechanism to compare the relative ratios of latex to soluble organics. Figure 4.14 A, B is for AR1 and C, D is the corresponding plots for AR2, scales so that the soluble organics are the same intensity. It is clear from the figure that the amount of latex in AR2 is significantly less than AR1. A simple scaling of the peaks shows this ratio to be 35% +/- 2%.

4.5.3 Summary

We have developed a fast method of quantifying the change in the ratio of latex particles to soluble organics in latex emulsions. We have applied this method to the alignment run one (AR1) and alignment run two (AR2) latexes used in Mojito cyan. We have observed that AR2 has only 35% of the latex compared to AR1.

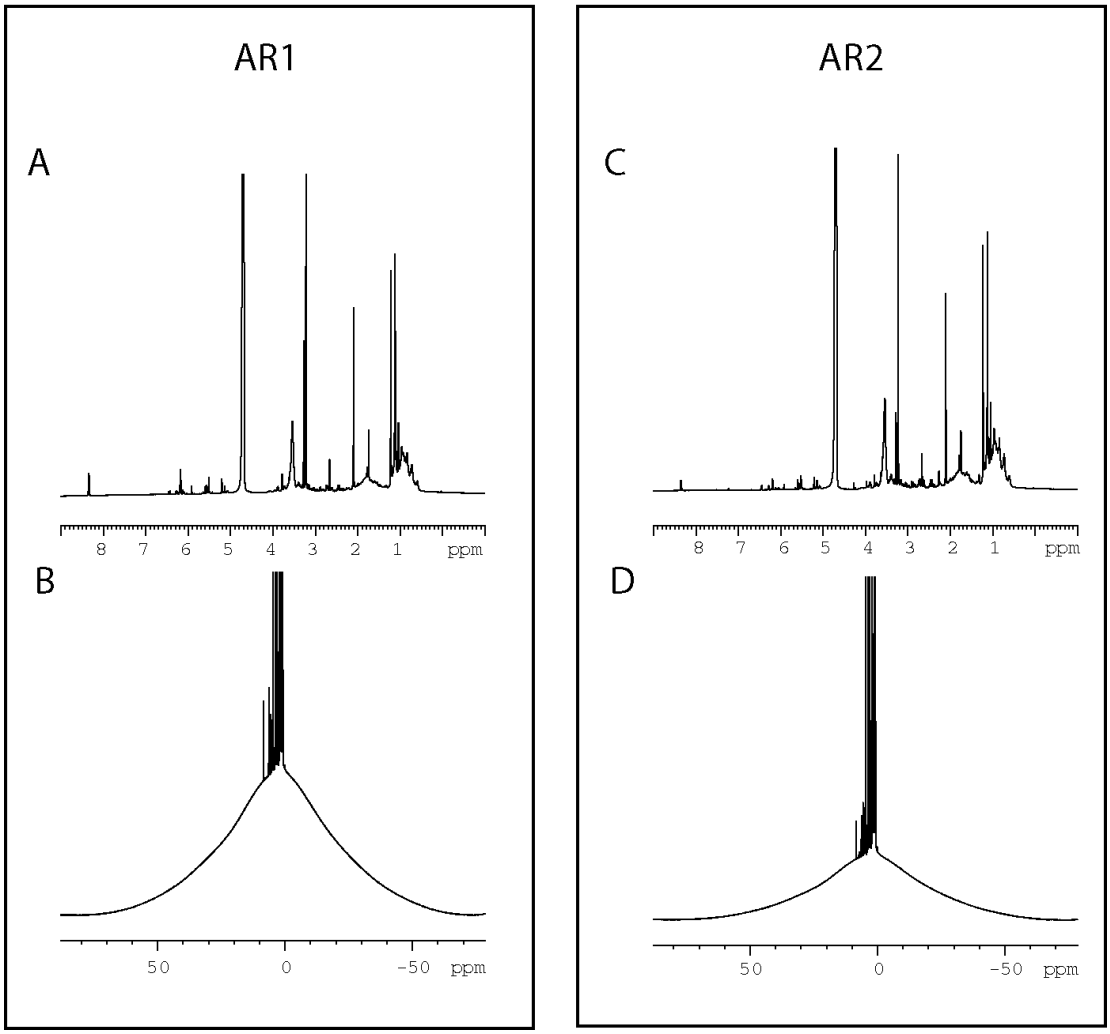

Figure 4.14 ^{1}H NMR spectra for AR1 (A, B) and AR2 (C, D). The upper plots are expanded in the central region to show the soluble organics, while the bottom plots show the full spectral region and the large, broad latex peak. Data were acquired on a 14.1 T (600 MHz, ^{1}H) Bruker AVANCE II spectrometer with a recycle delay of 20 s. 32 transients were averaged for a total acquisition time of 12 minutes.

4.6 Effect of protonation on the conformation of Cinchonidine

4.6.1 Introduction

Cinchona alkaloids are natural products, found in the bark of *Cinchona ledgeriana* trees. These natural products are extremely useful in a variety of industrial applications. They are used in pharmaceuticals for the treatment of malaria[45] and cardiac arrhythmias[46], as additives for soft drinks[47], starting materials for organic synthesis[48], as chiral resolving agents in fractional crystallization[49] and chromatographic techniques[50], and as agents for promoting enantioselective transformations in both homogeneous[51] and heterogeneous[52] catalysis. Cinchona has such wide applications due to their unique structural property, characterized by an aromatic quinoline ring connected to a quinuclidine tertiary amine through a chiral alcoholic carbon. Figure 4.15 shows a typical

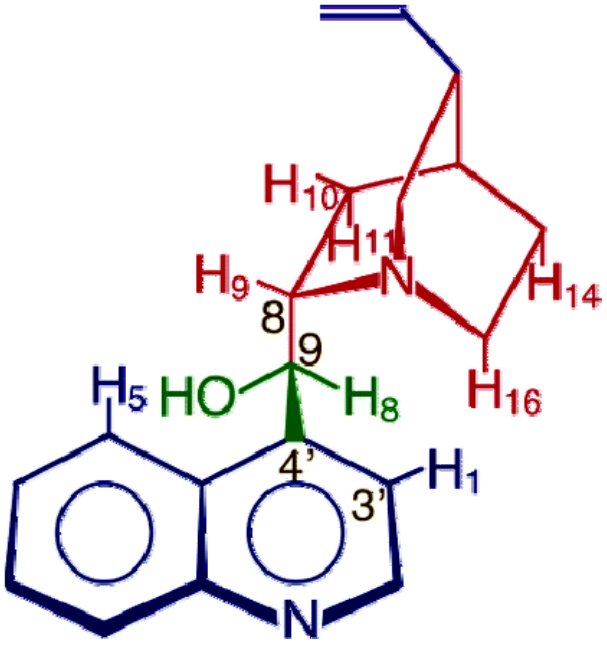

Figure 4.15 Cinchonidine molecule ***(Published with permission from ref 53. Copyright 2006 American Chemical Society)***

cinchonidine molecule[53].

The useful properties of cinchona has been attributed to the environment around the chiral linker and have shown to involve the participation of the nitrogen in the aliphatic amine [54,55]. Addition of a proton to the aliphatic amine changes the chemistry of cinchona, as shown by Karle and Ferri[56,57], presumably by inducing a change in molecular confirmation[58-60]. We use a combined approach of using Nuclear Magnetic Resonance spectroscopy and ab initio computational methods to investigate the effect of protonation on the conformational preference of cinchona in this section of the chapter.

4.6.2 Results and Discussion

The signals of normal ^{1}H NMR spectrum are correlated with each other in a 2D COSY (Correlation Spectroscopy) spectrum. Cross peaks exist in the 2-D COSY spectrum where there is spin-spin coupling between protons (or other nuclei such as ^{19}F and ^{31}P). Since this coupling usually exists over a length of two or three chemical bonds, the connectivity and structure can be obtained from the COSY spectrum. COSY spectra were obtained for the free base and HCl-protnated cinchonidine molecule in deuterated methanol. Assignments were made using Spakry software to obtain the position of various protons on the molecule (Figure 4.16 and 4.17).

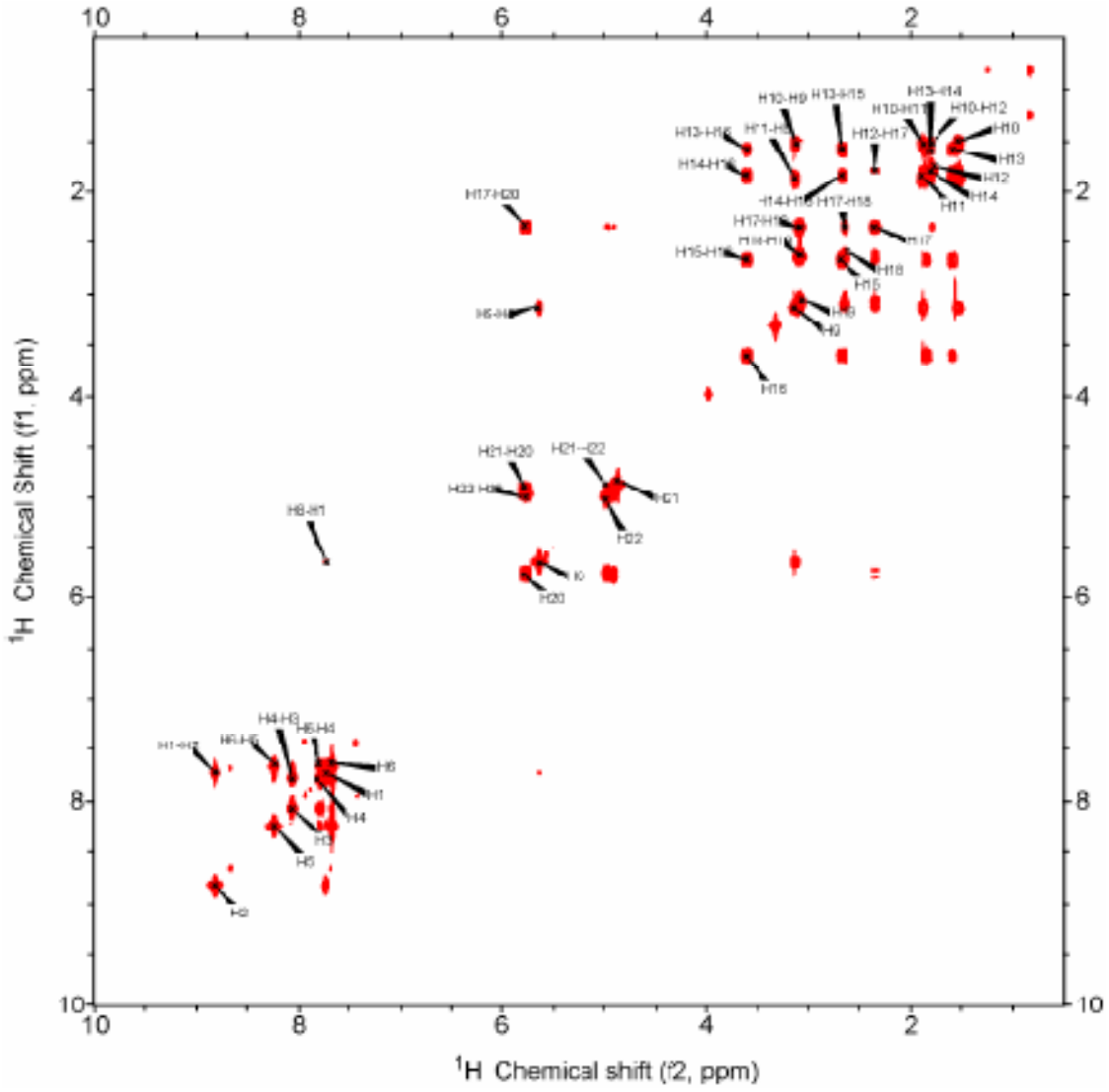

Figure 4.16 2D COSY correlation spectrum of Cinchonidine in deuterated methanol. Data were acquired on a 11.7 T Varian Inova spectrometer (1H frequency 500.14 MHz) equipped with a triple-resonance triple-axis gradient probe. 256 real-valued t1 points and 2048 complex t2 points were acquired with a spectral width of 6.5 kHz in each dimension. 4 scans per t1 increment were co-added with a relaxation delay of 1 s. Spectrum was linear predicted once in the indirect dimension, and a sine-bell apodization applied to both dimensions before zero filling once and Fourier

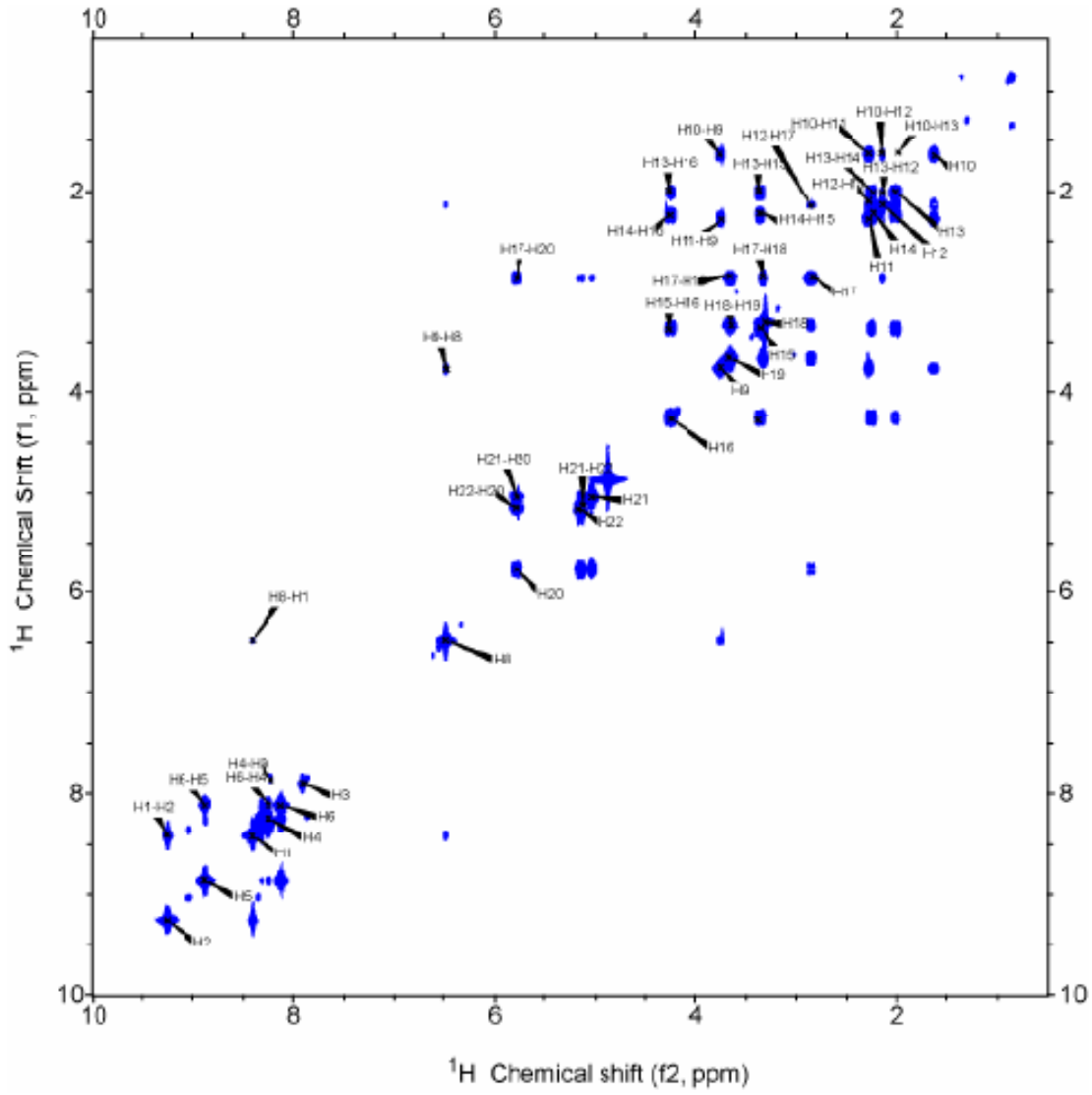

Figure 4.17 2D COSY correlation spectrum of protonated Cinchonidine in deuterated methanol. Data were acquired on a 14.1 T Bruker Avance Spectrometer (^{1}H frequency 600.14 MHz) equipped with a double-resonance single-axis gradient proton-fluorine probe. 2048 complex -valued t1 points and 4096 complex t2 points were acquired with a spectral width of 10.8 kHz in each dimension. 4 scans per t1 increment were co-added with a relaxation delay of 1 s. Spectrum was linear predicted once in the indirect dimension, and a sine-bell apodization applied to both dimensions before zero filling

Nuclear Overhauser Enhancement Spectroscopy (NOESY) experiment gives rise to correlation signals due to dipole cross-relaxation between nuclei in space[61]. The intensity of the peaks gives information on distance between the two given nuclei, since it is related to the sixth power of special distance. NOESY experiments were performed on pure cinchonidine and protonated cinchonidine in solution. Figure 4.18 shows complete NOESY spectrum of pure cinchonidine and Figure 4.19 shows expanded regions of the NOESY spectra for free cinchonidine in deuterated methanol solutions. Cross-peaks are seen in the spectrum for the free cinchonidine, indicating close contacts between the H_1 and H_5 atoms of the quinoline aromatic ring and the H_8 and H_9 atoms of the linker chiral centers as well as the H_{11}, H_{14}, and H_{16} axial atoms of the quinuclidine ring. This indicates nearly free molecular rotation around both $C_{4'}-C_9$ and C_9-C_8 bonds or, as previously reported in other solvents, fast interconversion among a number of stable conformations[62-64]. However, the absence of signal for the interaction between H_5 and H_{11} points to some limitations to this free rotation.

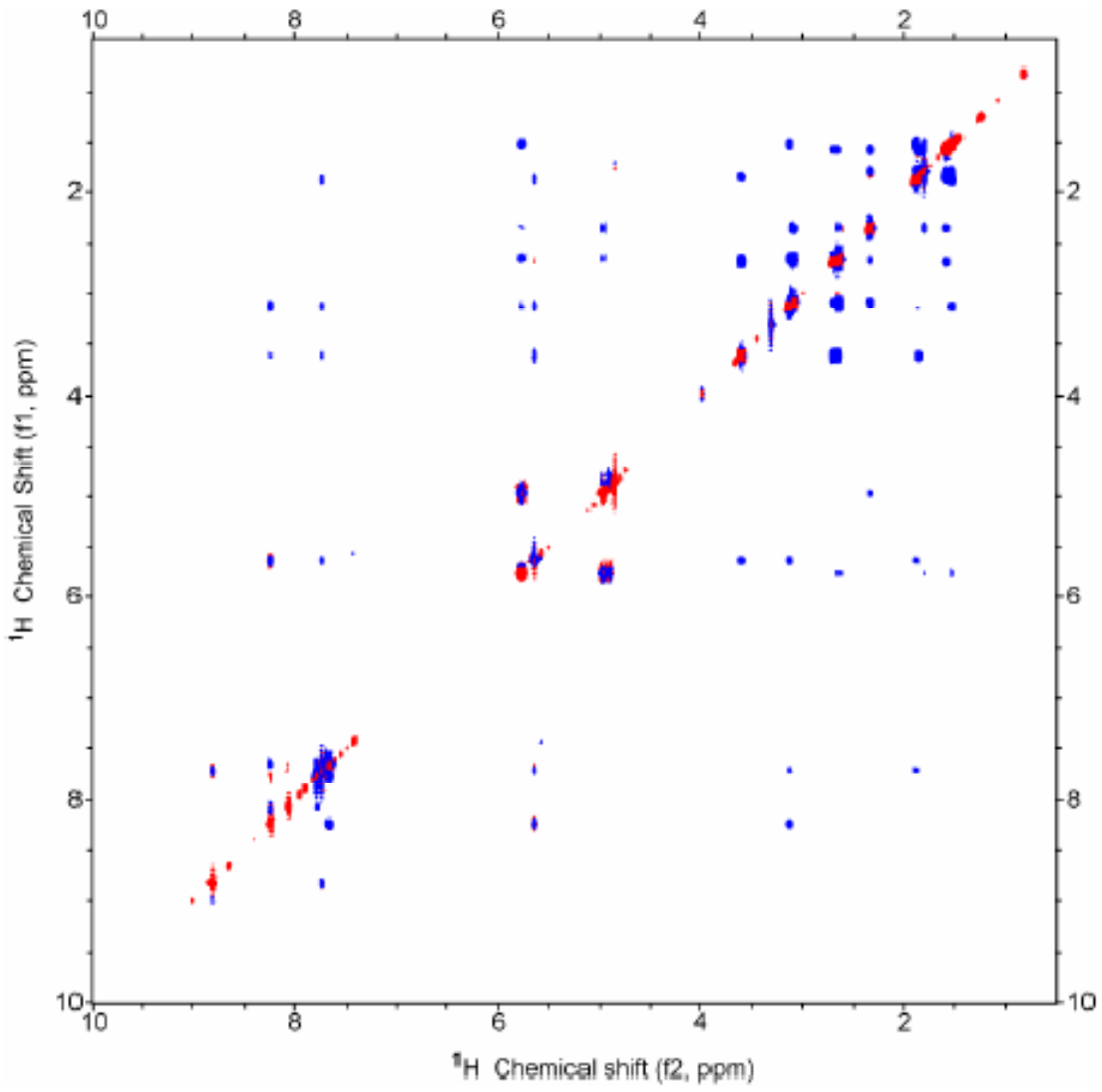

Figure 4.18 2D NOESY correlation spectrum of Cinchonidine in deuterated methanol. Data were acquired on a 11.7 T Varian Inova spectrometer (1H frequency 500.14 MHz) equipped with a triple-resonance triple-axis gradient probe. 128 complex-valued t1 points and 1024 complex t2 points were acquired with a spectral width of 6.5 kHz in each dimension. 4 scans per t1increment were co-added with a relaxation delay of 1.5 s and a mixing time of 500 ms. Spectrum was linear predicted once in the indirect dimension, and a 90-shifted sine-bell apodization applied to both dimensions before zero filling once and Fourier transformation.

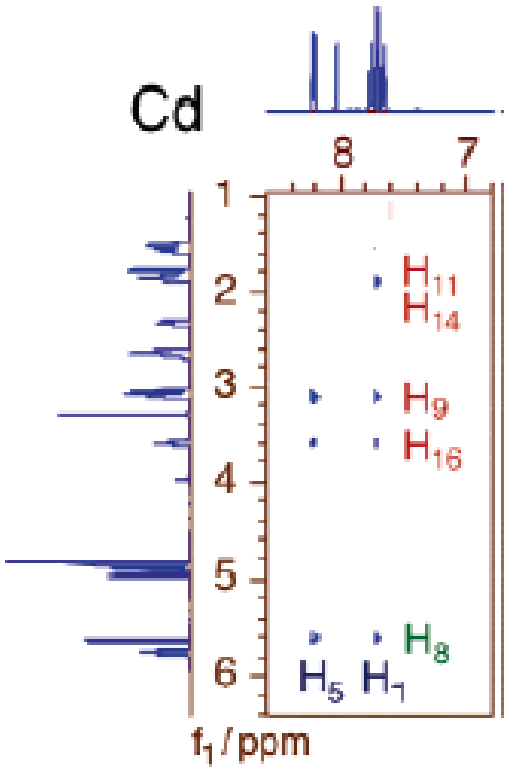

Figure 4.19 Details of ^{1}H NOESY 2D NMR spectra from 10 mM solutions of free base (Cd, Aldrich 96% purity) cinchonidine, showing the cross peak region

The complete NOESY spectrum of the protonated cinchonidine is shown in Figure 4.20 and Figure 4.21 shows its expanded regions in deuterated methanol solutions. They display a significantly lower number of cross-peaks, indicating close interactions only between the H_5−H_8, H_5−H_9, and H_1−H_{14} pairs of atoms. These data can be easily interpreted as corresponding to conformations where the C_9−C_8 bond is approximately at a right angle from the quinoline ring, the OH group pointing toward the H_1 side of that ring, and the $C_{4'}$−C_9 and C_8−N bonds roughly aligned. Such a structure is analogous to the so-called Open(3) arrangement identified in similar systems by X-ray crystallography[13] and quantum mechanical calculations[60,63]

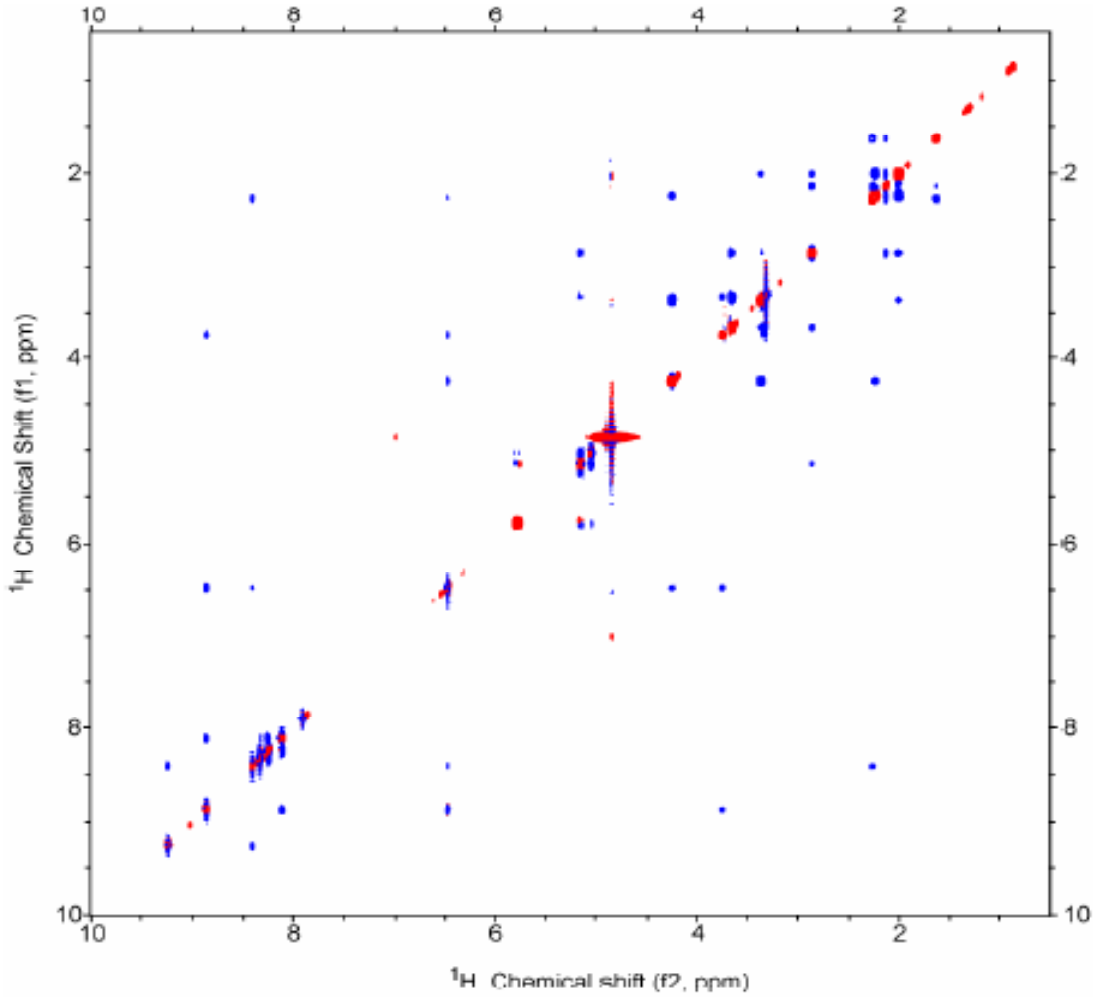

Figure 4.20 2D NOESY correlation spectrum of protonated Cinchonidine in deuterated methanol. Data were acquired on a 14.1 T Bruker Avance Spectrometer (^{1}H frequency 600.14 MHz) equipped with a double-resonance single-axis gradient proton-fluorine probe. 1024 complex-valued t1 points and 2048 complex t_2 points were acquired with a spectral width of 10.8 kHz in each dimension. 4 scans per t_1 increment were co-added with a relaxation delay of 1.5 s and a mixing time of 500 ms. Spectrum was linear predicted once in the indirect dimension, and a 90-shifted sine-bell

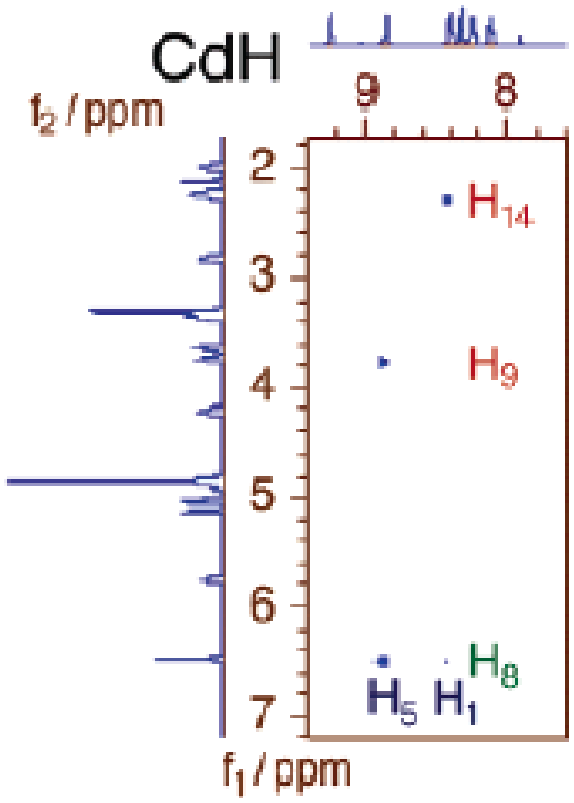

Figure 4.21 Details of ^{1}H NOESY 2D NMR spectra from 10 mM solutions of HCl-protonated (CdH, prepared by titration with HCl) cinchonidine in deuterated methanol showing the cross peak region

The protonation of cinchonidine appears to hinder rotation around the $C_{4'}$–C_9 and C_9–C_8 bonds and to favor only a narrow range of the conformational space of the molecule. Previous studies on the behavior of cinchonidine in the presence of acetic[65], mandelic[66], and tiglic[67] acids indicating similar rotational restrictions were explained by the formation of Coulombic complexes between CdH and the carboxylate group of the corresponding conjugate base via a hydrogen-bonded bridge from the protonated quinuclidine nitrogen to the acidic hydroxo group. However, in those cases, the argument was made that the driving force for such an interaction is the particular fit of the carboxylate ions in the bridging position of the Open(3) conformation of cinchonidine, perhaps because of its bidentate coordination[65]. With other acids and with different cinchona isomers, direct hydrogen bonding between the amine and hydroxyl groups, without the intervention of the counterion, has been invoked to justify similar restrictions in molecular rotations[68] Competition between direct inter- and intramolecular hydrogen bonding has also been used to justify the varying biological activity of different cinchona[56,59,60].

To investigate the role of the counterion in stabilizing the protonated cinchonidine structure, ^1H–^{19}F NMR experiments were performed on the HF-protonated cinchonidine salt ($CdH^+ \cdot F^-$) in both methanol and the aprotic solvent acetonitrile. Limited rotation was again observed in both cases, and close proximity between the fluorine anion and H_5, H_8, and the hydroxyl proton (in the acetonitrile solution) was identified by heteronuclear $^1H[^{19}F]$ NOE difference experiments (Figure 4.22)[69]

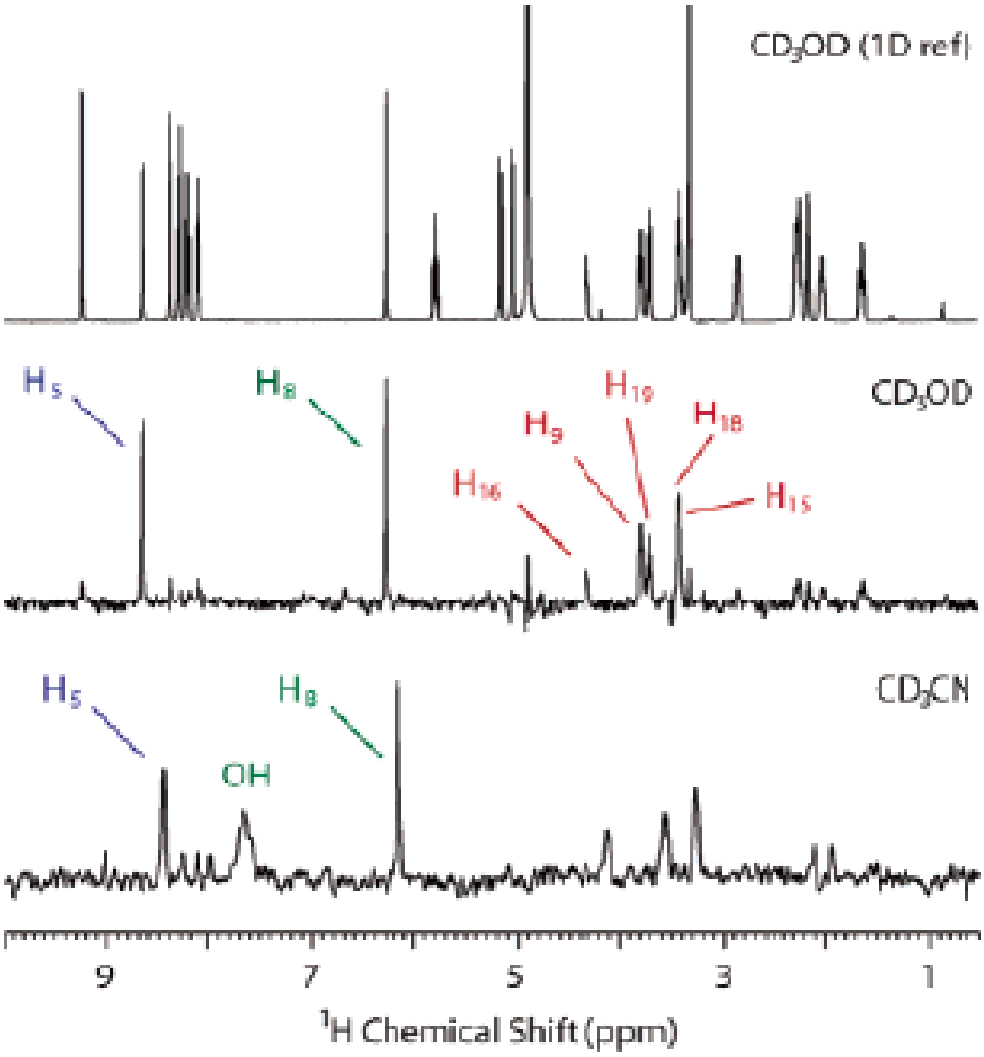

Figure 4.22 $^{1}H[^{19}F]$ NOE difference spectrum (τ_{mix} = 0.25 s) of the HF-protonated cinchonidine salt $CdH^{+}.F^{-}$ in acetonitrile (bottom) and methanol (middle). The F^{-} anion remains tightly associated with the N-H^{+} moiety, giving rise to heteronuclear NOEs to the hydroxyl proton as well as H_5, H_8, and several protons on the quinuclidine ring. (Top) A 1D ^{1}H spectrum of CdH^{+}.F- in methanol is also shown for reference.

This strongly suggests the participation of the counterion in stabilizing the conformations that result from protonation. The $^{1}H-^{19}F$ NMR are consistent with the conformation suggested by Figure 4.23 but also add the need for the formation of a bridge between the nitrogen atom in the quinuclidine ring and other hydrogens via the insertion of an HF (or an HCl) molecule.

Consistent with the NMR data, ab initio quantum mechanical calculations of the HF- and HCl-protonated cinchonidine yielded two similar minimum energy structures for each case, with approximately the same $C_{3'}-C_{4'}-C_9-C_8$ dihedral angle ($\sim$90°) and only a $\sim$30° difference in the second $C_{4'}-C_9-C_8-N$ angle (Figure 4.23).

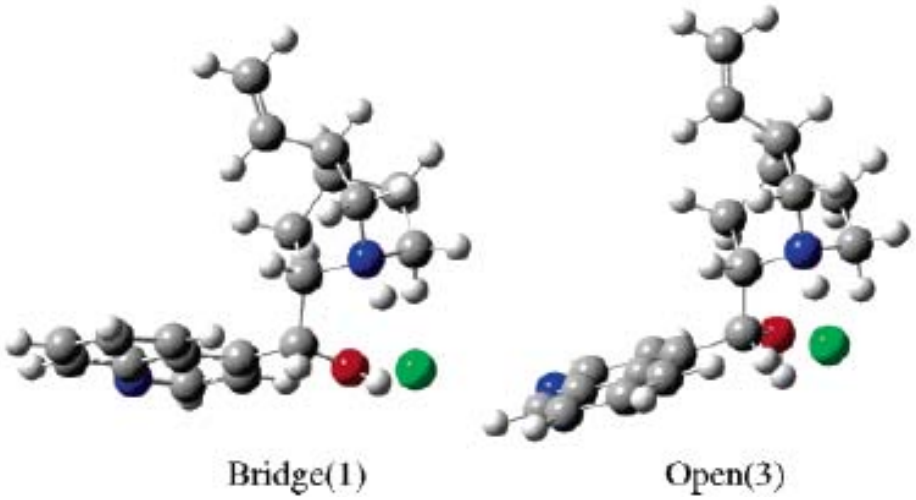

Figure 4.23 Minimum energy structures for protonated cinchonidine, calculated using Gaussian03 (DFT-B3LYP; 6-31G(d,p)). In the presence of either chlorine (shown) or fluorine (not shown) counterions, the two lowest-energy conformations have torsional constraints analogous to the acetate structure, with the anion participating in either a hydrogen-bonding bridge (Bridge(1), left) or an ion pair conformation involving other non-acidic hydrogen atoms in the cinchona (Open(3), right) ***(Published with permission from ref 53. Copyright 2006 American Chemical Society)***

In fact, the main difference between those two structures, shown in Figure 4.23, is in the position of the counterion: in one, the F^-/Cl^- is nested between the amino and hydroxo groups, while in the other, the interaction is with the non-acidic H_5 atom of the quinoline ring. The former is an additional low-energy minimum not present in the unprotonated Cd, while the latter structure corresponds most closely to the lowest energy Open(3) conformation of Cd, but with the conjugate base anion interacting with the electrostatically positive plane of the aromatic system. As the two conformations determined by our calculations have energies that differ by less than 1 kcal/mol, they are likely to be in fast exchange in solution; the structure implied by the NOESY data in Figure 4.19 and 4.21 is therefore taken to represent their average. Several other stable minima were found at higher energies (tabulated in the Supporting Information), but notably, those corresponding to the favorable Closed(1) and Closed(2) conformations in Cd ($C_{4'}-C_9-C_8-N$ angles of ~60−70°) were found to be extremely unfavorable in the salts, with energies greater than 9 kcal/mol above their respective ground states.

4.6.3 Section Conclusion

A direct evidence of a connection between the protonation of the amine and a change in conformational preference in the cinchona is provided through a combination of NMR and ab initio calculation methods. The free rotations around the central C-C bonds are severely impaired by protonation, and that the conjugate base anion plays an active role in stabilizing the resulting structures. Addition of the acid shifts the equilibrium to favor a small conformational subspace. The generality of this binding motif and the concomitant rotational restriction that it causes has important implications

for understanding the reactivity of cinchona. In particular, it must now be realized that the conformational restriction in cinchona caused by simple diatomic acids may be more complicated than the simple N−H−O hydrogen-bonding mechanism previously proposed.

4.7 Chapter Conclusion

A wealth of information can be gathered from NMR active nuclei which are common in most biological systems (^{1}H, ^{13}C, ^{31}P, ^{15}N, ^{17}O) and materials (^{13}C, ^{29}Si, ^{77}Se, ^{27}Al). ^{29}Si can have broad lines in the NMR spectrum, and therefore demand the use of CPMAS along with longer acquisitions. Printing inks and various other formulations used in printing industry comprise mainly of large ($\geq$10 kDa) organic molecules. As a result of their large size and high viscosity, they behave almost like solids in the NMR timescale. A bifocal approach of using solid as well as liquid state NMR spectroscopy to unravel some of the compositional and functional aspects of their chemistry has a promising future.

REFERENCES

(1) Schaefer, J.; Stejskal, E. O. *Journal of the American Chemical Society* **1976**, *98*, 1031-1032.

(2) Wang, L. Z.; Shi, J. L.; Yu, J.; Yan, D. S. *J. Inorg. Mater.* **1999**, *14*, 333-342.

(3) Kresge, C. T.; Leonowicz, M. E.; Roth, W. J.; Vartuli, J. C.; Beck, J. S. *Nature* **1992**, *359*, 710-712.

(4) Lei, C.; Shin, Y.; Liu, J.; Ackerman, E. J. *J. Am. Chem. Soc.* **2002**, *124*, 11242.

(5) Kesanli, B.; Lin, W. *Chem. Commun.* **2004**, 2284.

(6) Mihalcik, D. J.; Lin, W. *Angew Chem., Int. Ed.* **2008**, *47*, 6229.

(7) Zhu, H.; Liang, C.; Yan, W.; Overbury, S. H.; Dai, S. *J. Phys. Chem. B* **2006**, *110*, 10842.

(8) Lei, C.; Shin, Y.; Liu, J.; Ackerman, E. J. *Nano Lett.* **2007**, *7*, 1050.

(9) Trewyn, B. G.; Slowing, I. I.; Giri, S.; Chen, H.; Lin, V. S. Y. *Acc. Chem. Res.* **2007**, *40*, 846.

(10) Trewyn, B. G.; Giri, S.; Slowing, I. I.; Lin, V. S. Y. *Chem. Commun.* **2007**, 3236.

(11) Slowing, I. I.; Trewyn, B. G.; Giri, S.; Lin, V. S. Y. *Adv. Func. Mater.* **2007**, *17*, 1225.

(12) Taylor, K. M. L.; Kim, J. S.; Rieter, W. J.; An, H.; Lin, W. *J. Am. Chem. Soc.* **2008**, *130*, 2154.

(13) Hernandez, R.; Tseng, H. R.; Wong, J. W.; Stoddart, J. F.; Zink, J. I. *J. Am. Chem. Soc.* **2004**, *126*, 3370.

(14) Nguyen, T. D.; Leung, K. C. F.; Liong, M.; Pentecost, C. D.; Stoddart, J. F.; Zink, J. I. *Org. Lett.* **2006**, *8*, 3363.

(15) Leung, K. C. F.; Nguyen, T. D.; Stoddart, J. F.; Zink, J. I. *Chem. Mater.* **2006**, *18*, 5919.

(16) Nguyen, T. D. K.; Leung, C. F.; Liong, M.; Liu, Y.; Stoddart, J. F.; Zink, J. I. *Adv. Funct. Mater.* **2007**, *17*, 2101.

(17) Patel, K.; Angelos, S.; Dichtel, W. R.; Coskun, A.; Yang, Y. W.; Zink, J. I.; Stoddart, J. F. *J. Am. Chem. Soc.* **2008**, *130*, 2382.

(18) Aznar, E.; Marcos, M. D.; Martinez-Manez, R.; Sancenon, F.; Soto, J.; Amoro, P.; Guillem, P. *J. Am. Chem. Soc.* **2009**, *131*, 6833.

(19) Liu, R.; Zhang, Y.; Zhao, X.; Agarwal, A.; Mueller, L. J.; Feng, P. Y. *Journal of the American Chemical Society* **2010**, *132*, 1500-1502.

(20) Lai, C. Y.; Trewyn, B. G.; Jeftinija, D. M.; Jeftinija, K.; Xu, S.; Jeftinija, S.; Lin, V. S. Y. *J. Am. Chem. Soc.* **2003**, *125*, 4451.

(21) Ying, J. Y.; Mehnert, C. P.; Wong, M. S. *Angew. Chem., Int. Ed.* **1999**, *38*, 56.

(22) Hoffmann, F.; Cornelius, M.; Morell, J.; FrÃ¶ba, M. *Angew. Chem., Int. Ed.* **2006**, *45*, 3216.

(23) Asefa, T.; MacLachlan, M. J.; Coombs, N.; Ozin, G. A. *Nature* **1999**, *402*, 867.

(24) Inagaki, S.; Guan, S.; Fukushima, Y.; Ohsuna, T.; Terasaki, O. *J. Am. Chem. Soc.* **1999**, *121*, 9611.

(25) Melde, B. J.; Holland, B. T.; Blanford, C. F.; Stein, A. *Chem. Mater.* **1999**, *11*, 3302.

(26) Han, Y. J.; Stucky, G. D.; Butler, A. *J. Am. Chem. Soc.* **1999**, *121*, 9897.

(27) Yan, X.; Yu, C.; Zhou, X.; Tang, J.; Zhao, D. *Angew. Chem., Int. Ed.* **2004**, *43*, 5980.

(28) Vallet-RegÃ-, M.; RÃ¡mila, A.; del Real, R. P.; PÃ©rez-Pariente, J. *Chem. Mater.* **2001**, *13*, 308.

(29) Misawa, S.; Kumagai, I. *Biopolymers* **1999**, *51*, 297.

(30) Rozema, D.; Gellman, S. H. *J. Am. Chem. Soc.* **1995**, *117*, 2373.

(31) Hevehan, D. L.; De Bernardez Clark, E. *Biotechnol. Bioeng.* **1997**, *54*, 221.

(32) Lu, D. N.; Liu, Z.; Wu, J. Z. *Biophys. J.* **2006**, *90*, 3224.

(33) Goldberg, M. E.; Rudolph, R.; Jaenicke, R. *Biochemistry* **1991**, *30*, 2790.

(34) Buswell, A. M.; Middleberg, A. P. *J. Biotechnol. Bioeng.* **2003**, *83*, 567.

(35) Fischer, B.; Perry, B.; Summer, I.; Goodenough, P. *Protein Eng.* **1992**, *5*, 593.

(36) Katoh, S.; Terashima, M.; Kishida, H.; Yagi, H. *J. Chem. Eng. Jpn.* **1997**, *30*, 964-965

(37) Wang, X. Q.; Lu, D. N.; Austin, R.; Agarwal, A.; Mueller, L. J.; Liu, Z.; Wu, J. Z.; Feng, P. Y. *Langmuir* **2007**, *23*, 5735-5739.

(38) Sayari, A.; Yang, Y. *Chem. Commun.* **2002**, 2582-2583.

(39) Wang, W.; Xie, S.; Zhou, W.; Sayari, A. *Chem. Mater.* **2004**, *16*, 1756.

(40) Klinowski, J. *Prog. Nucl. Magn. Reson. Spectrosc.* **1984**, *16*, 237-309.

(41) Lippmaa, E. T.; Alla, M. A.; Pehk, T. J. *Journal of the American Chemical Society* **1978**, *100*, 1929-1931.

(42) Lippmaa, E.; Magi, M.; Samoson, A.; Engelhardt, G.; Grimmer, A. R. *Journal of the American Chemical Society* **1980**, *102*, 4889-4893.

(43) Gibby, M. G.; Pines, A.; Waugh, J. S. *Journal of the American Chemical Society* **1972**, *94*, 6231-&.

(44) Errede, L. A.; Tiers, G. V. D. *Journal of Physical Chemistry B* **1997**, *101*, 7794-7807.

(45) Wilairatana, P.; Krudsood, S.; Treeprasertsuk, S.; Chalermrut, K.; Looareesuwan, S. *Arch. Med. Res.* **2002**, *33*, 416.

(46) Aviado, D. M.; Salem, H. *J. Clin. Pharmacol.* **1975**, *15*, 477.

(47) Dewick, P. M. *Medicinal natural products : a biosynthetic approach*; 2nd ed.; Wiley: Chichester, West Sussex, England, 2004.

(48) Hoffmann, H. M. R.; Frackenpohl, J. *Eur. J. Org. Chem.* **2004**, *null*, 4293.

(49) McCague, R.; Smith, A. *Innovations Pharm. Technol.* **1999**, *99*, 100.

(50) Francotte, E. R. *J. Chromatogr., A* **2001**, *906*, 379.

(51) Bolm, C.; Gladysz, J. A. *Chem. Rev.* **2003**, *103*, 2761.

(52) Baiker, A. *J. Mol. Catal. A* **1997**, *115*, 473.

(53) Olsen, R. A.; Borchardt, D.; Mink, L.; Agarwal, A.; Mueller, L. J.; Zaera, F. *Journal of the American Chemical Society* **2006**, *128*, 15594-15595.

(54) Schwalm, O.; Weber, J.; Minder, B.; Baiker, A. *Int. J. Quantum Chem.* **1994**, *52*, 191.

(55) Yoon, T. P.; Jacobsen, E. N. *Science* **2003**, *299*, 1691.

(56) Karle, J. M.; Bhattacharjee, A. K. *Bioorg. Med. Chem.* **1999**, *7*, 1769.

(57) Ferri, D.; BÃ¼rgi, T.; Borszeky, K.; Mallat, T.; Baiker, A. *J. Catal.* **2000**, *193*, 139.

(58) Dijkstra, G. D. H.; Kellogg, R. M.; Wynberg, H.; Svendsen, J. S.; Marko, I.; Sharpless, K. B. *J. Am. Chem. Soc.* **1989**, *111*, 8069.

(59) Warhurst, D. C.; Craig, J. C.; Adagu, I. S.; Meyer, D. J.; Lee, S. Y. *Malaria J.* **2003**, *2*, 1.

(60) Caner, H.; Biedermann, P. U.; Agranat, I. *Chirality* **2003**, *15*, 637.

(61) Jeener, J.; Meier, B. H.; Bachmann, P.; Ernst, R. R. *Journal of Chemical Physics* **1979**, *71*, 4546-4553.

(62) Dijkstra, G. D. H.; Kellogg, R. M.; Wynberg, H. *J. Org. Chem.* **1990**, *55*, 6121.

(63) BÃ¼rgi, T.; Baiker, A. *J. Am. Chem. Soc.* **1998**, *120*, 12920.

(64) Maier, N. M.; Schefzick, S.; Lombardo, G. M.; Feliz, M.; Lindner, K. R.; Lipkowitz, K. B. *J. Am. Chem. Soc.* **2002**, *124*, 8611.

(65) Ferri, D.; BÃ¼rgi, T.; Baiker, A. *J. Chem. Soc., Perkin Trans. 2* **1999**, *null*, 1305.

(66) Larsen, S.; Lopez de Diego, H.; Kozma, D. *Acta Crystallogr., Sect. B: Struct. Sci.* **1993**, *49*, 310.

(67) Ferri, D.; BÃ¼rgi, T.; Baiker, A. *J. Chem. Soc., Perkin Trans. 2* **2002**, *null*, 437.

(68) Karle, J. M.; Karle, I. L.; Gerena, L.; Milhous, W. K. *Antimicrob. Agents Chemother.* **1992**, *36*, 1538.

(69) Martinez, D.; Gerig, J. T. *J. Magn. Reson.* **2001**, *152*, 269.

CHAPTER V

CONCLUSION

The application of NMR methodology to solve problems in the field of analytical chemistry and material science is presented in this thesis work. Synthesis and characterization of new materials with a wide variety of applications is being developed at an ever accelerating rate. Solid-state NMR proves to be a robust molecular level probe for use often in conjuncture with X-ray crystallography and *ab initio* structural refinement, for solid state structure determination.

The presence of unpaired electrons in neutral molecular radical conductors makes them a promising material in the fields of optoelectronics, magnetooptics and spintronics. However, the presence of the single electron gives paramagnetic characteristic to these materials, which makes NMR spectra shift, broaden and loose signal due to the reduction in the relaxation rates. The application of solid-state paramagnetic NMR to study the electronic structure and phase change of these conductors establishes a hypothesis of fast exchange between the phenalenyl rings, as discussed in Chapter 2 of this thesis. Further work is underway in this direction to quantitatively test the model and provide insight into the spin densities on carbon centers in the molecule.

The molecular-level motions leading to the photomechanical response of molecular crystal nanostructures based on anthracene esters can be studied using a combination of solid-state NMR and X-ray crystallography, as reported in Chapter 3 of

this thesis. Since NMR can probe the structural changes in these nanorods without perturbing the system, it is highly applicable to gain insight into the molecular-level dynamics that give rise to the micron-scale response of photomechanical molecular crystal systems.

NMR active nuclei which are common in most biological systems (^{1}H, ^{13}C, ^{31}P, ^{15}N, ^{17}O) and materials (^{13}C, ^{29}Si, ^{77}Se, ^{27}Al) are routinely being used to characterize industrially applicable systems. ^{29}Si, which is a common element for the framework construction in several modern day materials, can be studied using ssNMR using CP-MAS techniques. Printing inks and similar polymeric formulations, behave almost like solids in the NMR timescale. Simultaneous use of solid as well as solution state NMR spectroscopy can answer questions regarding the chemistry of their composition and functions.

Cross-polarization to enrich the sensitivity of rare nuclei, faster spinning rates of samples at magic angle, use of more efficient decoupling sequences, and using pulse sequence specifically tailored for the problem at hand can all be used together to investigate the structure, properties and functions of inorganic materials. Application of these ideas is the central theme of this thesis. A solid platform which has been founded, as show in this thesis, will help solve materials problems of the future.